DISSERTATION

# CHARGE CARRIER DYNAMICS OF 2-DIMENSIONAL PHOTOELECTRODES PROBED VIA ULTRAFAST SPECTROELECTROCHEMISTRY

Submitted by

Rachelle Austin

Department of Chemistry

In partial fulfillment of the requirements

For the Degree of Doctor of Philosophy

Colorado State University

Fort Collins, Colorado

Summer 2024

Doctoral Committee:

Advisor: Justin Sambur
Co-Advisor: Amber Krummel

Anthony Rappe
Amy Prieto
Andrew McNally
Samuel Brewer

ABSTRACT

CHARGE CARRIER DYNAMICS OF 2-DIMENSIONAL PHOTOELECTRODES PROBED VIA ULTRAFAST SPECTROELECTROCHEMISTRY

The integration of hot charge carrier-based energy conversion systems with two-dimensional (2D) semiconductors holds immense promise for enhancing the efficiency of solar energy technologies and enabling novel photochemical reactions. Current approaches, however, often rely on costly multijunction architectures. In this dissertation, I present research that combines spectroelectrochemical and *in-operando* transient absorption spectroscopy measurements to unveil ultrafast (<50 fs) hot exciton and free charge carrier extraction in a proof-of-concept photoelectrochemical solar cell constructed from earth-abundant monolayer (ML) $MoS_2$. Theoretical analyses of exciton states reveal enhanced electronic coupling between hot exciton states and neighboring contacts, facilitating rapid charge transfer. Additionally, I discuss insights into the physical interpretation of transient absorption (TA) spectroscopy data in 2D semiconductors, comparing historical perspectives from physical chemistry and solid-state physics literature. My perspective encompasses various physical explanations for spectral features and experimental trends, particularly focusing on the contribution of trions to TA spectra. Furthermore, I examine how different physical interpretations and data analysis procedures can yield distinct timescales and mechanisms from the same experimental results, providing a comprehensive framework for understanding charge carrier dynamics in 2D semiconductor-based optoelectronic devices.

# ACKNOWLEDGEMENTS

I extend my sincerest appreciation to my advisors, Amber Krummel and Justin Sambur, for their invaluable mentorship, guidance, and unwavering support throughout my academic and research endeavors. Their expertise, encouragement, and belief in my potential have been instrumental in shaping my academic and professional growth, equipping me with the knowledge and problem-solving skills to overcome challenges, collaborate across disciplines, and realize success.

I also send my deepest gratitude to my peer mentors Dr. Yusef Farah and Dr. R. Colby Evans. Their fantastic leadership set my standards for quality scientific research and communication, and their example continues to motivate me to learn and grow. I could not have done this work without them, and I feel incredibly grateful to have had them as mentors.

I am indebted to my physics professor, Dr. William Schoenfeld, whose profound knowledge, mentorship, and guidance have influenced my academic trajectory. His dedication to fostering intellectual curiosity has inspired me to delve deeper into the realms of scientific inquiry. Furthermore, I am grateful to my high school teacher, Frank Hanson, whose passion for chemistry and dedication to his students ignited my fascination with the subject. His encouragement to pursue AP chemistry laid the foundation and set me on the path to where I am today.

I extend my heartfelt gratitude to my parents, whose unwavering support and encouragement have underpinned my academic journey. Their sacrifices, guidance, and belief in my abilities have propelled me forward, instilling in me the determination to pursue my goals with unwavering dedication.

To my dear friends, thank you for standing by my side, offering solace during the difficult

moments, and celebrating the victories with unwavering enthusiasm. Your camaraderie and encouragement have lightened my burdens and enriched my experiences, reminding me of the importance of connection amidst academic pursuit.

Lastly, I am profoundly grateful for my partner Zachary and his steadfast support and boundless compassion throughout the rigors of graduate school. His unwavering presence, understanding, and encouragement have been a constant source of strength, enabling me to navigate the challenges and triumphs of this journey with greater resilience.

To all who have played a role in my academic journey, I am deeply grateful for your support and belief in my potential. Your influence has left an indelible mark on my life, and I am thankful for the privilege of learning and growing alongside such incredible individuals. This chapter in my life has irrevocably changed my life, both personally and professionally, and I look forward to what the next chapter brings.

# DEDICATION

I dedicate this dissertation to Doodle.

TABLE OF CONTENTS

# Chapter 1 : INTRODUCTION

## 1.1 Motivation for hot carrier solar energy devices

As efforts to combat climate change and shift towards sustainable energy systems intensify, research and development of renewable energy technology has never been more crucial. Within clean energy sources, solar energy conversion emerges as a particularly promising technology. Solar energy was first commercialized in the 1980s, but after 40 years of development and $382 billion of investment in 2022 alone (*1*), solar energy currently only comprises 4.5% of total global electricity generation (*2*). The problem that currently limits widespread use of solar energy conversion devices is efficiency (*3*).

One method to improve the efficiency of solar energy conversion devices that use semiconductors is to utilize the energy above the band gap, which is traditionally lost as heat (*4*–*6*). In semiconductors, electronic energy states form bands; the band containing the highest occupied states is denoted the valence band, and the band containing the lowest unoccupied states is termed the conduction band. The band gap is the difference in energy between the top of the valence band and bottom of the conduction band. Illuminating a semiconductor with light of energy above the semiconductor bandgap generates free charge carriers into higher-energy conduction band states that are above the conduction band minimum energy (Figure 1-1). These highly excited free charge carriers are termed "hot carriers" in accordance with their excess energy. After excitation, hot carriers will rapidly cool to the bandgap edges (conduction band minimum and valence band maximum) by transferring their excess energy to the crystal lattice via phonons (lattice vibrations). This thermalization loss of the energy above the bandgap accounts for a 33% energy loss of incident sunlight and is the largest limiting factor to solar energy conversion (*7*).

Notably, nanostructures such as quantum wells, quantum dots, perovskites, and 2-dimensional materials have demonstrated slower carrier cooling rates as compared to bulk materials. As a result, they hold significant potential for hot carrier devices ((*8*). Hot carrier extraction could improve the efficiency of commercialized solar photovoltaics as well as solar-fuel-producing photoelectrochemical cells, potentially doubling the maximum theoretical efficiency from of 33% (*9*) to 66% (*10*).

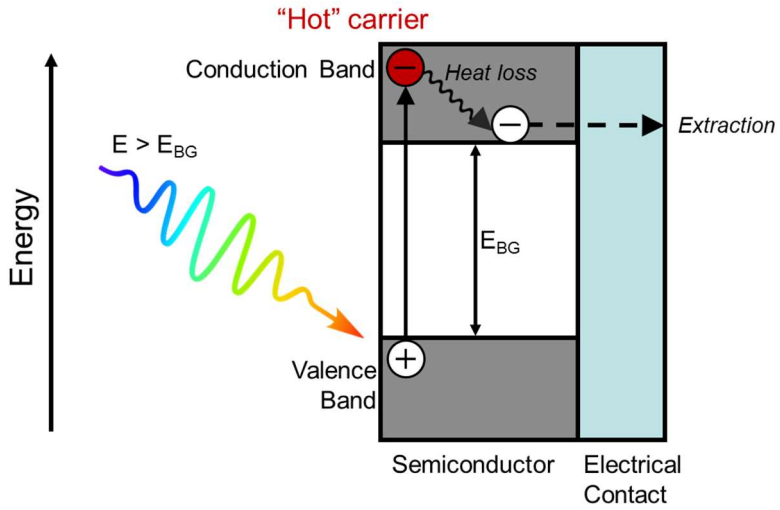


Figure 1-1. Simplified diagram of hot carrier cooling in a semiconductor. Light with energy greater than the bandgap of the semiconductor ($E_{BG}$) excites electrons from the valence band into the conduction band. The highly excited hot carriers cool (lose energy through heat) to the band edge before they are extracted for use in the device.

Notably, hot carrier extraction enhances efficiency in different ways for photovoltaic devices and photoelectrochemical cells. Photovoltaic devices convert sunlight directly into electricity. Photoelectrochemical cells convert sunlight to storable chemical fuels by using solar energy to do reactions. In a photovoltaic device architecture, hot carrier extraction can improve power output through increasing the voltage of the solar cell (*11*). In solar photoelectrochemical cells, hot carrier extraction can improve efficiency by driving high-energy, photo-induced charge

transfer reactions that are not possible under ordinary conditions (*12*). An additional benefit of photoelectrochemical cells is that the storable fuels they generate eliminate the need for battery storage. Photoelectrochemical cells also offer an ideal device design for the study of hot carriers due to the perpendicular geometry of carrier extraction.

**1.2 Hot carrier photoelectrochemical cells**

The basic geometry of a photoelectrochemical cell is provided in Figure 1-2. This design facilitates hot carrier extraction because generated carriers need only to travel the thickness of the material to reach extraction sites (electrolyte interface and electrical contact) and do not need to diffuse laterally for extraction. Additionally, charge carrier extraction can be tuned in photoelectrochemical cells through the applied voltage and redox potential of the electrolyte, which can be altered to maximize the amount and energy of extracted charge carriers.

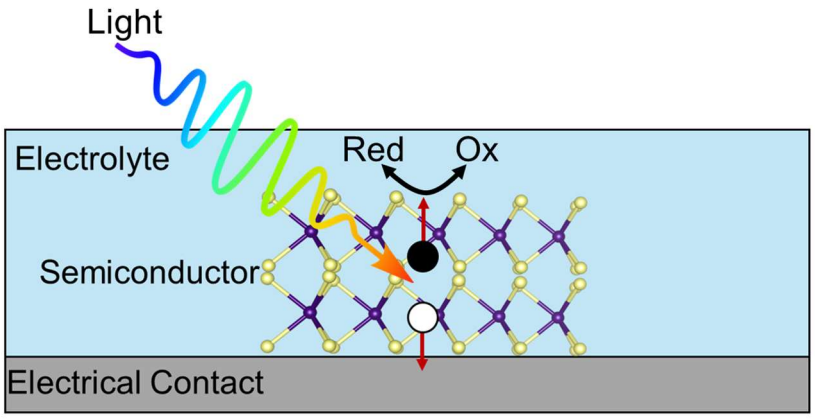


Figure 1-2. Basic geometry of a photoelectrochemical device. The semiconductor on an electrical contact forms the photoelectrode. Light hits the semiconductor photoelectrode to generate electrons and holes (shown as black and white circles, respectively), which then react with redox species or transfer to the electrical contact for extraction.

The main methods of charge carrier extraction in solar energy conversion cells are reactions with redox molecules at the semiconductor-electrolyte interface or extraction at an electrical

contact. Previous work has shown that hot carriers can be extracted via redox reactions in GaP and InP (*13*, *14*) and extracted at electrical contacts in halide perovskites (*15*), quantum dots (*16*), and two-dimensional transition metal dichalcogenides (2D TMDs) (*17*). However, a main issue with hot carrier extraction is that cooling happens as carriers travel through the material, so a material and device design that minimizes charge carrier travel is required to make hot carrier extraction possible. One material and device combo that fulfills this requirement is 2-dimensional transition metal dichalcogenides (2D TMDs) in photoelectrochemical cells.

**1.3 2D TMDs for hot carrier extraction**

2D TMDs are a class of low-cost (*18*), atomically thin semiconductors of the form $MX_2$ (M = Mo or W, X = S, Se, Te). The 2D TMDs are composed of a layer of transition metal atoms sandwiched between two layers of chalcogen atoms as shown in Figure 1-3. Bulk crystals of these materials are formed with many layers bound together by weak van der Waals interactions. The layers of these materials can be easily thinned down to a single layer, or "monolayer," that is only three atoms thick, as shown in Figure 1-3. The most well-studied 2D TMD to date is molybdenum disulfide ($MoS_2$). Monolayer $MoS_2$ is an ideal candidate for hot carrier extraction applications because it has a direct bandgap of 1.88 eV that is suitable for solar energy absorption (*19*) and can absorb 10% of incident visible light, even with a material thickness of < 1 nm (*20*). It also has optimal material geometry for hot carrier extraction. The three-atom thickness of monolayer $MoS_2$ reduces the distance that hot charge carriers need to travel for extraction at electrolyte or electrical contacts in a photoelectrochemical cell design, as shown in Figure 1-3. In multilayer bulk samples, generated charge carriers must travel through the crystal lattice to reach extraction sites. This extended travel results in hot carriers cooling before extraction. The thinness of monolayer $MoS_2$

significantly reduces this distance, optimizing the hot carrier extraction efficiency and extracted hot carrier energy.

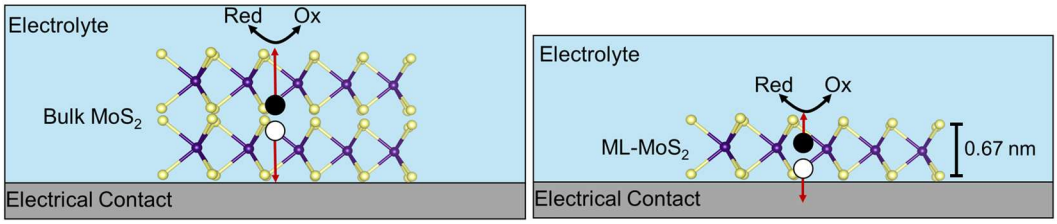


Figure 1-3. Schematic comparing the extraction of charge carriers at electrical contact and electrolyte for a bulk sample (left) and monolayer sample (right). Electrons are depicted as black circles, while holes are depicted as white circles.

The ways in which hot carriers cool and decay in monolayer $MoS_2$ have been studied in air, but not within photoelectrochemical devices. The dynamics of hot carriers under device operating conditions are not well understood and the energy and yield of hot carrier extraction has not yet been quantified. This complexity arises from the multitude of complex physical and chemical mechanisms behind charge carrier generation and cooling in monolayer $MoS_2$ (more detail of these mechanisms can be found in Chapter 2).

### 1.4 Spectroscopy as a tool to probe electron dynamics

Our aim is to investigate the behavior of charge carriers and their dynamics within 2D TMDs while they function inside of a device. How can we measure this information without disassembling the device? Utilizing light that can pass through the device enables non-invasive, non-destructive measurements of the 2D material during device operation. We leverage the way light interacts with matter to learn information we cannot directly see, such as chemical and molecular structure and dynamics. Spectroscopy (*spectre*, "ghost" and *scopy*,"to examine") is, by definition, the study of the interaction of light and matter. The essence of my research centers on

this fundamental interplay between light and matter at both linear and nonlinear levels of interaction.

Linear spectroscopy encompasses a suite of powerful techniques used to investigate the interactions between light and matter in a linear manner. At its core, linear spectroscopy is the absorption, emission, or scattering of light by a sample across a range of wavelengths or energies. By measuring the intensity and wavelength dependence of these interactions, linear spectroscopy enables researchers to identify molecular constituents, determine electronic and vibrational energy levels, and elucidate structural characteristics with remarkable precision (*21*). Common examples of linear spectroscopic techniques include UV-Visible spectroscopy, infrared spectroscopy, and Raman spectroscopy, each offering unique capabilities for probing different aspects of molecular and electronic structure. In each of these techniques, light from a light source is sent to the system of interest and the light that comes out is measured – a photon in, and a photon out. The incident light is weak and therefore a small perturbation to the system. A weak interaction of light and matter is a linear interaction.

Nonlinear spectroscopy explores optical processes that arise from the nonlinear interaction of materials to intense light fields (*21*, *22*). The sample can interact with light multiple times, and these multiple interactions of light can exchange energy, interfere, and couple with each other within the chemical system. Nonlinear spectroscopy techniques utilize high-intensity, pulsed laser sources to leverage the nonlinear interactions between photons and matter. The goal is to unveil rich structural and dynamic information that is often inaccessible through linear methods. Using extremely short pulses of laser light can measure how the chemical system responds to a light source and how the excited sample evolves over time (excited state dynamics). This is the basis for the nonlinear spectroscopy technique of pump-probe spectroscopy. As discussed in more detail

in Chapter 2, pump-probe spectroscopy uses two laser pulses (one as a "pump" and one as "probe") to probe ultrafast processes and unravel dynamic behaviors in chemical systems.

### 1.5 Outline of Dissertation

In this dissertation, I use 2D TMD photoelectrochemical cells as a model system for the study of hot carrier extraction. I unite the techniques of linear and nonlinear visible light spectroscopy with electrochemistry to probe the steady-state and excited-state electronic and charge extraction dynamics of 2D TMD photoelectrodes. I begin with background information on the mechanism of charge carrier generation in 2D TMD semiconductors, the techniques of spectroelectrochemistry and transient absorption, and motivation for the design of our experiments in Chapter 2. Chapter 3 details the experimental methods used to collect and analyze all data for this study. Chapter 4 is our published study of hot carrier extraction from 2D TMD photoelectrodes. Finally, Chapter 5 is an invited perspective that discusses the unique photophysics of multi-charge species in 2D TMDs and their implications for charge carrier dynamics interpretations.

**References**


1. International Energy Agency, IEA Report World Energy Investment 2023, *IEA* (2023).
2. International Energy Agency, Renewables 2023, *IEA* (2024).
3. Y. H. Chiu, T. H. Lai, M. Y. Kuo, P. Y. Hsieh, Y. J. Hsu, Photoelectrochemical cells for solar hydrogen production: Challenges and opportunities. *APL Mater* **7** (2019).
4. C. V. Shank, R. L. Fork, R. F. Leheny, J. Shah, Dynamics of photoexcited GaAs band-edge absorption with subpicosecond resolution. *Phys Rev Lett* **42**, 112–115 (1979).
5. W. J. Danaher, L. E. Lyons, Irreversibilities in the mechanism of photoelectrolysis. *Nature* **271**, 137 (1978).
6. B. D. S., W. F., N. A. J., Hot carrier injection at semiconductor- electrolyte junctions. *J Appl Phys* **51**, 2158–2163 (1980).
7. M. Wolf, A new look at silicon solar cell performance. *Energy Conversion* **11**, 63–73 (1971).
8. D. T. Nguyen, L. Lombez, F. Gibelli, S. Boyer-Richard, A. Le Corre, O. Durand, J. F. Guillemoles, Quantitative experimental assessment of hot carrier-enhanced solar cells at room temperature. *Nat Energy* **3**, 236–242 (2018).
9. R. T. Ross, A. J. Nozik, Efficiency of hot-carrier solar energy converters. *J Appl Phys* **53**, 3813–3818 (1982).
10. W. Shockley, H. J. Queisser, Detailed balance limit of efficiency of p-n junction solar cells. *J Appl Phys* **32**, 510–519 (1961).
11. I. Konovalov, V. Emelianov, Hot carrier solar cell as thermoelectric device. *Energy Sci Eng* **5**, 113–122 (2017).
12. A. J. Nozik, Utilizing hot electrons. Nature Publishing Group [Preprint] (2018). https://doi.org/10.1038/s41560-018-0112-5.

13. J. A. Turner, A. J. Nozik, J. A. Turner, A. J. Nozik, Evidence for hot - electron injection across p - GaP / electrolyte junctions Evidence for hot-electron injection across p-GaP lelectrolyte junctions. **101**, 1–4 (1996).

14. G. Cooper, J. A. Turner, B. A. Parkinson, A. J. Nozik, Hot carrier injection of photogenerated electrons at indium phosphide-electrolyte interfaces. *J Appl Phys* **54**, 6463–6473 (1983).

15. M. Li, S. Bhaumik, T. W. Goh, M. S. Kumar, N. Yantara, M. Grätzel, S. Mhaisalkar, N. Mathews, T. C. Sum, Slow cooling and highly efficient extraction of hot carriers in colloidal perovskite nanocrystals. *Nat Commun* **8**, 3–12 (2017).

16. P. Singhal, H. N. Ghosh, Hot Charge Carriers in Quantum Dots: Generation, Relaxation, Extraction, and Applications. *ChemNanoMat* **5**, 985–999 (2019).

17. L. Wang, Z. Wang, H. Y. Wang, G. Grinblat, Y. L. Huang, D. Wang, X. H. Ye, X. Bin Li, Q. Bao, A. S. Wee, S. A. Maier, Q. D. Chen, M. L. Zhong, C. W. Qiu, H. B. Sun, Slow cooling and efficient extraction of C-exciton hot carriers in MoS2 monolayer. *Nat Commun* **8** (2017).

18. Y. H. Lee, X. Q. Zhang, W. Zhang, M. T. Chang, C. Te Lin, K. Di Chang, Y. C. Yu, J. T. W. Wang, C. S. Chang, L. J. Li, T. W. Lin, Synthesis of large-area MoS 2 atomic layers with chemical vapor deposition. *Advanced Materials* **24**, 2320–2325 (2012).

19. J. Gusakova, X. Wang, L. L. Shiau, A. Krivosheeva, V. Shaposhnikov, V. Borisenko, V. Gusakov, B. K. Tay, Electronic Properties of Bulk and Monolayer TMDs: Theoretical Study Within DFT Framework (GVJ-2e Method). *Physica Status Solidi (A) Applications and Materials Science* **214**, 1–7 (2017).

20. M. Bernardi, M. Palummo, J. C. Grossman, Extraordinary sunlight absorption and one nanometer thick photovoltaics using two-dimensional monolayer materials. *Nano Lett* **13**, 3664–3670 (2013).

21. S. Mukamel, *Principles of Nonlinear Optical Spectroscopy* (Oxford University Press, New York, 1995).

22. P. E. H. J. W. Powers, *Fundamentals of Nonlinear Optics* (CRC Press, 2nd Edition., 2017).

# Chapter 2 : BACKGROUND & MOTIVATION

This chapter provides a comprehensive overview of key concepts essential for understanding the subsequent research. This chapter explains the use of spectroelectrochemistry as a method to study the behavior of charge carriers within devices using light to probe electronic systems. Finally, this chapter discusses the utility of transient absorption spectroscopy as a tool for probing ultrafast charge carrier dynamics on femtosecond timescales.

## 2.1 Mechanisms of carrier generation in 2D TMD semiconductors

As briefly mentioned in Chapter 1, electronic energy states in semiconductors form bands; the band containing the highest occupied states is the named the valence band (the energy levels the valence electrons occupy) and the band containing the lowest unoccupied states is called the conduction band (the energy levels at which electrons are delocalized and able to contribute to electrical conductivity). The band gap is the difference in energy between the top of the valence band and bottom of the conduction band. Electrons in the valence band can absorb light equal to or greater than the energy of the bandgap to be excited into the conduction band, thereby allowing the flow of charge through the semiconductor. Left in the valence band is a “hole,” or localized region of positively-charged electron absence that also acts as a charge carrier in the semiconductor.

In bulk semiconductors at room temperature, photoexcited electrons and holes exist as “free carriers” that can travel independently through the material. Electrons and holes that are bound together via coulombic interaction are called excitons, and these bound electron-hole pairs act as a quasiparticle that travels with a constant radius through the crystal lattice. In bulk semiconductors, excitons are weakly bound and will freely dissociate at room temperature. Unlike bulk semiconductors, excitons in 2-dimensional semiconductors such as 2D transition metal

dichalcogenides (TMDs) are quantum confined and are strongly bound even at room temperature due to reduced dielectric screening (*1*). Excitons can also bind to an excess electron or hole to create three-particle "trions" that can exist at room temperature in 2D TMDs at sufficiently high carrier densities (*2*).

The 2D TMD studied in this body of work is molybdenum disulfide ($MoS_2$). Monolayer $MoS_2$ has three types of excitons (*3*) as shown in the band energy diagram in Figure 2-1. The band-edge A- and B-excitons have energies of 1.88 eV and 2.01 eV respectively and are split due to spin-orbit coupling in the valence band (*4*). The higher energy C-exciton is a unique exciton with energy of 2.98 eV that arises due to band nesting of the valence and conduction bands (*5*). Notably, band nesting results in a strongly enhanced optical response, resulting in the C-exciton dominating the UV-Vis absorbance spectrum of $MoS_2$ (*6*).

The electronic properties of semiconducting TMDs are determined by the bonding behavior between the metal and chalcogen atoms, which have been studied extensively since the 1950's and can be simplified with a ligand field model (*7*). $MoS_2$ has trigonal prismatic coordination (D3h symmetry), resulting in splitting of the Mo *d*-orbitals into $d_{z^2}$, $d_{xy}$ and $d_{x^2-y^2}$ states. The valence band maximum and conduction band minimum at the K-point are nearly exclusively $d_{xy}$ and $d_{x^2-y^2}$ states for Mo. This makes the excitation of A-excitons and B-excitons *d-d* transitions, which are known to be weakly absorbing in accordance with the Laporte selection rule. Conversely, the uppermost states at the Γ-point of the valence band originate mainly from $d_{z^2}$ orbitals on Mo atoms and the conduction band states are comprised of $p_z$ orbitals on S atoms. Thus, the excitation of C-excitons is a metal to ligand charge transfer, a transition that results in intense light absorption.

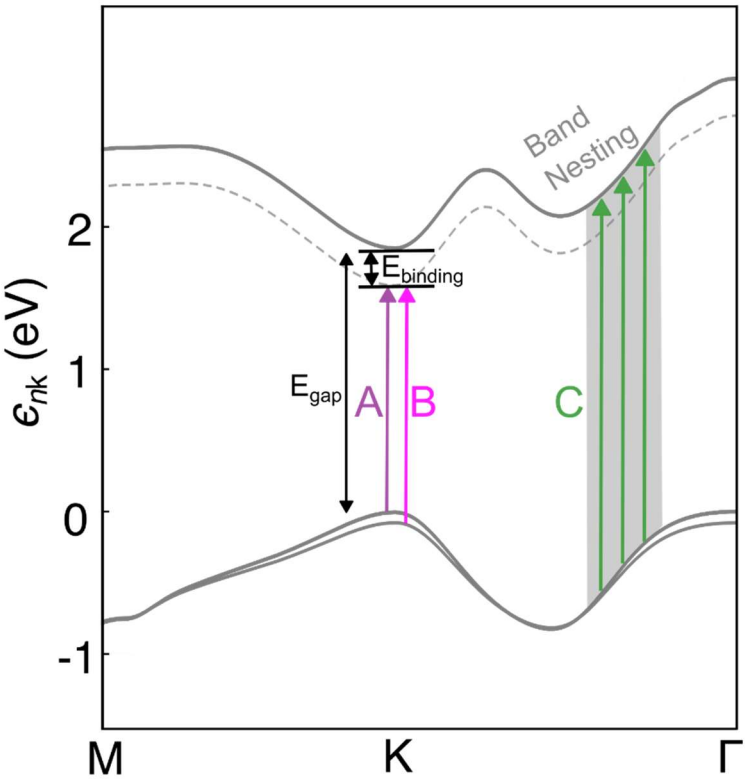


Figure 2-1. Band energy diagram of monolayer $MoS_2$. Adapted from (*7*).

Figure 2-1 compares the electronic bandgap energy ($E_{gap}$) to the exciton transitions and binding energy. The A- and B-exciton transition resonances are smaller than the electronic bandgap due to the large binding energy of the excitons ($E_{binding}$) (*1*, *8*, *9*) and it is $E_{exciton}$ that is observed as visible light absorption peaks in UV-Vis spectroscopy (see Chapter 3 for absorption data and analysis).

We detail here the generation and decay mechanisms of charge carriers and excitons in 2D TMDs. Upon photoexcitation with light above the bandgap energy, hot carriers and high-energy hot C-excitons are formed (process 1 in Figure 2-2). Hot carriers cool to the band edge via carrier-phonon scattering (typically in < 1ps), where they can become bound into A-excitons (*10*) (process 2). A- and B-excitons can diffuse through the material and may encounter trap states from defect sites in the crystal lattice that assist in electron-hole recombination (*11*) (process 3). Further exciton

decay pathways are radiative recombination (process 4), where an exciton decays by emitting a photon, and non-radiative recombination (process 5), where an exciton decays through emission of a phonon. The timescales over which these first-order decay mechanisms occur in 2D TMDs range from tens of femtoseconds to nanoseconds (*3*). After excitation, cooling processes (2 & 3) typically occur over a few picoseconds while recombination processes (4-5) occur over hundreds of picoseconds to nanoseconds. The dominant exciton decay pathway in as-synthesized monolayer $MoS_2$ is non-radiative recombination as evidenced by the low photoluminescence quantum yield (*12*). When the TMD is in contact with a substrate/superstrate, an additional pathway of charge transfer is possible, labelled as extraction (process 6) in Figure 2-2.

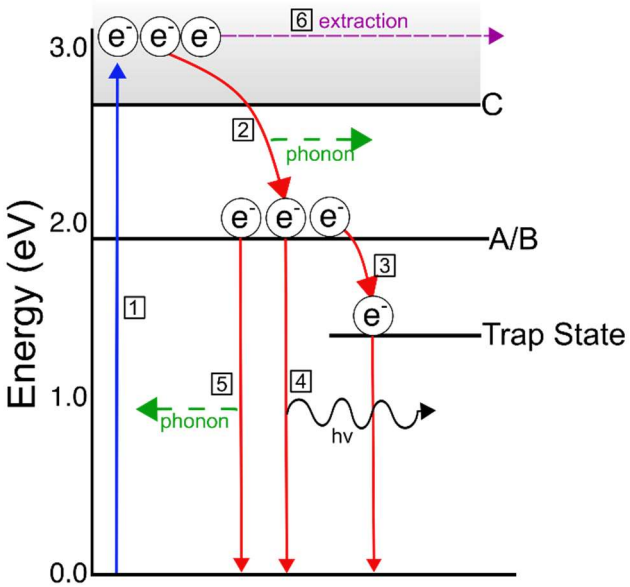


Figure 2-2. The pathways of charge carrier generation and decay. The A- and B-exciton states are represented as a singular band-edge state for simplicity. The C-exciton is represented as a shaded distribution of energy states that overlaps with free carrier energy states in the conduction band. Holes are omitted from the diagram for clarity.

## 2.2 Tuning charge extraction via applied potential

Charge extraction in electrochemical flow cells occurs via redox reactions with electrolyte species. In the studied $MoS_2$ cells with iodide as the redox species, the major reaction to generate photocurrent is oxidation of iodide to iodine via holes (*13*).

$$2I^- + 2h^+ \rightarrow I_2 \quad (6)$$

The photogenerated holes react with iodide at the electrode/electrolyte interface while the corresponding electrons travel through the conductive substrate at the working electrode and contribute to measured current. The potential applied to the sample via the potentiostat changes the number of electrons/holes extracted via redox reactions by causing a difference in electrochemical potential between the sample (the working electrode) and the counter electrode. Anodic potential applies a higher electrostatic potential at the $MoS_2$ and a lower electrostatic potential at the counter electrode. This potential difference causes electrons to flow out of the $MoS_2$ into the conductive substrate and causes holes to react with the iodide at the electrolyte interface. The reverse occurs at cathodic potential, where a lower electrostatic potential is applied to the working electrode and electrons flow into the $MoS_2$, thus resulting in a small amount of the reverse reaction (iodine reduction). The flow of charges due to the applied potential changes the charge carrier density within the $MoS_2$ (Figure 2-3). The influence of the potential-induced charge carrier density on the exciton energies and optical spectra of $MoS_2$ are discussed in detail in Chapter 5.

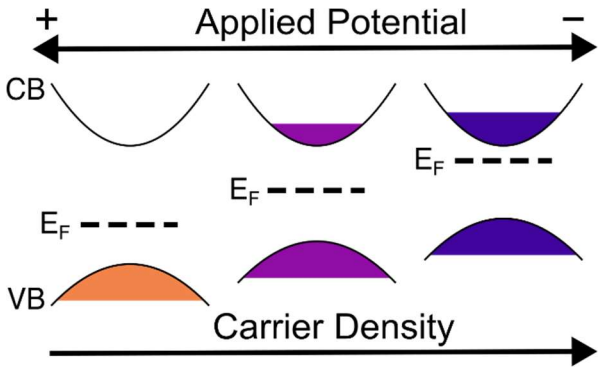


Figure 2-3. The effect of applied potential on electron density at the band edge of monolayer $MoS_2$.

**2.3 The driving force for charge transfer**

As mentioned in Chapter 1, hot carrier extraction in photoelectrochemical devices involves the injection of photoexcited charge carriers from the semiconductor electrode into a liquid electrolyte to drive high energy chemical redox reactions before the photoexcited carriers relax (i.e., thermalize) in the semiconductor.

A quantity necessary for understanding extraction of charge carriers in semiconductor electrochemical cells is the thermodynamic driving force for charge transfer (ΔG0'). ΔG0' is calculated as

$$\Delta G^{0'} = E_{CB} - qE^{0'}\left(\frac{A}{A^-}\right) \qquad Eq. 2-1$$

where $E_{CB}$ is the energy of the conduction band, $q$ is the charge of an electron ($1.6022 \times 10^{-19}$ C), and $E^{0'}(A/A^-)$ is the nonstandard redox potential of the redox couple ($A/A^-$) (*14*). The relationship between $\Delta G^{0'}$ and conduction band energy is qualitatively shown in Figure 2-4. The quantity $\Delta G^{0'}$ dictates the spontaneity and energy of the charge transfer (*15–17*). Extraction of charge carriers with excess energy above the conduction band edge therefore provides additional driving force to do reactions with large redox potentials, such as $CO_2$ reduction (*18*).

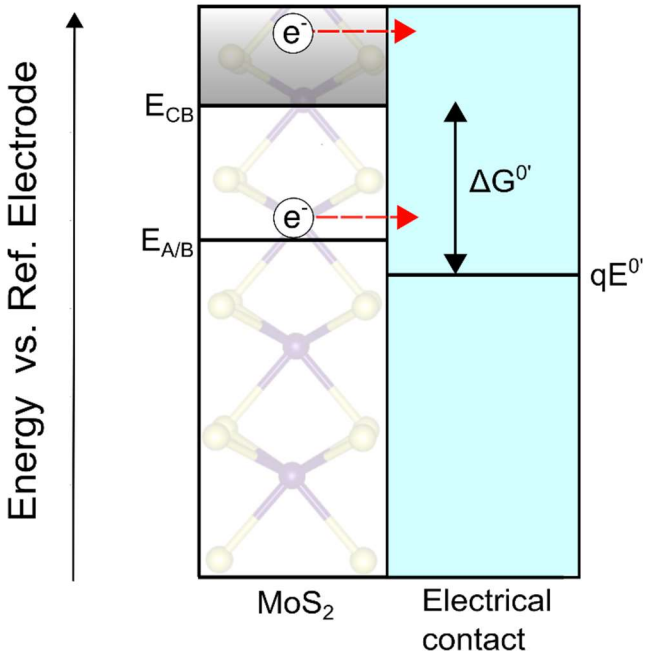


Figure 2-4. Simplified qualitative relationship between $\Delta G^{0'}$, electrolyte redox potential, and conduction band energy ($E_{CB}$) of monolayer $MoS_2$ with flatband potentials. Charge transfer is depicted with red arrows. The relative position of the A/B-exciton energy level ($E_{A/B}$ ) is also shown.

### 2.4 Spectroelectrochemistry as a technique to study charge carrier extraction in devices

Spectroelectrochemistry is the combination of spectroscopy and electrochemistry into a single experiment (*19*). This collection of *in-operando* simultaneous spectroscopic and electrochemical information gives insight to electron transfer processes happening at electrodes; electrochemistry measures charge extraction occurring at the electrode, while spectroscopy (in our UV-Vis spectroscopy) informs on the electronic energy levels of the electrode. In this research, we combine UV-Vis absorption spectroscopy with electrochemical techniques to study 1) the dependence of charge extraction on photon energy, and 2) the effect of applied voltage on light absorption. From these measurements (detailed in Chapters 3 and 4), we can learn which excitonic transitions contribute to current flow in the ML-$MoS_2$ photoelectrode. We also combine

electrochemistry with ultrafast transient absorption to probe the dynamics of excitons within the ML-$MoS_2$ electrode and study the rate and energy of charge transfer at the electrode.

**2.5 Transient Absorption as a technique for probing ultrafast charge carrier dynamics**

Transient absorption (TA) is a pump-probe spectroscopic technique used to study excited state dynamics of molecules and materials. Pump and probe beams within the UV/visible range are typically used in TA experiments as light absorption in this energy range provides information on electronic state dynamics (*20*). The femtosecond pump and probe pulses allow the measurement of excited state dynamics that occur on the order of femtoseconds to nanoseconds. A schematic of the typical transmission TA experiment is shown in Figure 2-5.

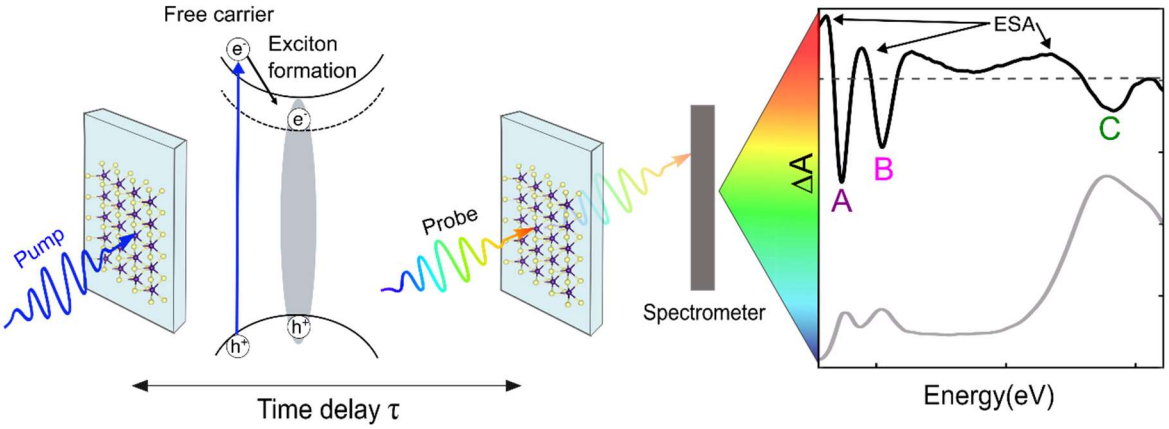


Figure 2-5. Scheme of the transient absorption technique. The pump laser pulse is shown exciting a sample of monolayer $MoS_2$ on a transparent substrate. The pump laser excites electrons from the valence band of the $MoS_2$ into the conduction band, generating free electrons and holes and subsequently excitons. The probe laser pulse is sent through the sample after a time delay τ and the probe laser pulse is measured by the spectrometer as a change in the absorbance versus probe energy (wavelength). An example TA spectrum of monolayer $MoS_2$ on ITO is plotted in black. The steady state absorbance of the same monolayer sample is given in grey for comparison of the exciton peak energies.

The absorbance of the excited sample is measured by first pumping the sample with a monochromatic laser pulse that is resonant with an electronic transition in the sample. This pump pulse induces a transition to an excited electronic state. The broadband probe pulse will pass

through the sample after the pump pulse with a specified time delay τ. The absorbance of the excited-state sample is calculated as

$$A^*(\lambda,\tau) = -log\left(\frac{I^*(\lambda,\tau)}{I_0(\lambda)}\right) \qquad Eq.2-2$$

where $I^*(\lambda,\tau)$ is the light transmitted through the excited sample at time τ. A change in absorbance between the ground state and excited state is given as

$$\Delta A(\lambda,\tau) = A^*(\lambda,\tau) - A^0(\lambda) = log\left(\frac{I(\lambda)}{I^*(\lambda,\tau)}\right) \qquad Eq.2-3$$

The signals $I_0(\lambda)$ and $I^*(\lambda,\tau)$ are typically spectrally resolved and recorded as a difference spectrum ($\Delta A(\lambda,\tau)$) for each time delay. This change in absorbance as a function of wavelength and time is denoted as the transient absorption signal, and it reports on the excited state of the sample and how that excited state evolves over time. There are two major electronic contributions to the transient absorption signal of $MoS_2$: ground-state bleach and excited-state absorption. Ground-state bleach is a negative ΔA signal that occurs when the absorbance of the ground state is higher than the absorbance of the excited state for a particular wavelength. This is because electrons have been promoted to a higher energy level and are no longer available to absorb probe photons. Excited state absorption is a positive ΔA signal because the absorbance of the excited sample is higher than the absorbance of the ground-state sample. This process occurs when excited electrons absorb more light for promotion into even higher electronic states, which can occur only when the sample has been pumped to the excited state. It is important to note that stimulated emission can contribute to transient absorption signal as negative ΔA signal (*20*), however it has not been reported in TA experiments of 2D TMDs. This may be due to the low photoluminescence (PL) signal of monolayer TMDs. In our samples, we measure low PL signal of monolayer $MoS_2$ on glass and

this signal is further quenched within our photoelectrochemical cell devices. Thus, we do not consider its contribution to the TA signal recorded in our experiments.

The time-dependence of TA signal informs on charge carrier and exciton generation, cooling, and decay in $MoS_2$. Photoexcitation of monolayer $MoS_2$ with the pump pulse will excite excitons and free charge carriers. The presence of excitons is measured as a photobleach (shown in Figure 2-5) while free carriers can contribute to excited state absorption signal (*21*, *22*). The exciton photobleach signal reports on the population and energies of excitons in the material. A higher population of excitons corresponds to a larger photobleach signal, while a smaller population of excitons produces a smaller photobleach signal. The exciton signal as a function of time reports on the dynamics of the mechanisms dominating exciton formation, cooling, and decay. Time constants for these decay processes are determined by fitting the TA signal decay as a function of time. Multiple methods can be used to fit the TA spectra and the signal decay. The different methods to analyze the TA signal as a function of both probe energy and time are discussed in depth in Chapter 5.

Transient absorption is an advantageous technique for studying charge carrier and exciton dynamics in $MoS_2$. The spectroscopic resolution of TA allows for the measurement of all three types of excitons present in monolayer $MoS_2$. Thus, the formation and decay of A-, B-, and C-excitons can be observed independently. Changes in the energy of excitons can be observed via shifting of the photobleach $\lambda_{max}$. The dynamics of all excitons can also be measured on ultrafast timescales that are simply not achievable with electrical measurements such as electrochemical impedance spectroscopy or intensity-modulated photocurrent spectroscopy. Additionally, the use of an electromagnetic probe allows for measurement of dynamics *in-operando* so that carrier and

exciton dynamics can be studied under the presence of electrolyte and applied potential to evaluate actual device operation conditions.

**2.6 Project Goals**

This dissertation focuses on proof-of-concept monolayer $MoS_2$ photoelectrodes for solar energy conversion applications. The research goals of this body of work are:

*Research Goal #1:* to determine how applied potential affects hot carrier cooling and extraction in a proof-of-concept monolayer $MoS_2$ photoelectrochemical cell via Transient Absorption spectroscopy.

*Research Goal #2:* to illuminate the underlying mechanism causing broadening and shifting of steady-state and transient optical spectra of 2D TMDs.

Understanding the dynamics of free charge carrier and exciton generation, cooling, and decay in $MoS_2$ flow cells will provide fundamental insight into how charge carrier cooling and extraction can be tuned. This knowledge can be used to further the design of hot carrier devices with higher efficiencies than are possible with current technology. Understanding the cause of observed shifting of the steady-state and transient absorption spectra of 2D TMDs within our photoelectrochemical devices will provide foundational understanding of the many-body physics affecting the complex doping-, fluence-, and time-dependent shifts observed in optical spectra of 2D TMDs.

The details of the design of the proof-of-concept monolayer $MoS_2$ photoelectrochemical cell, electrochemical characterization of the $MoS_2$ cell with photocurrent spectroscopy, potential-dependent UV-Vis absorbance, and transient absorption measurements of the electrochemical cell under a range of applied potentials are given in Chapter 3. Discussion of these results are given in Chapters 4 and 5.

**References**


1. A. Chernikov, T. C. Berkelbach, H. M. Hill, A. Rigosi, Y. Li, O. B. Aslan, D. R. Reichman, M. S. Hybertsen, T. F. Heinz, Exciton binding energy and nonhydrogenic Rydberg series in monolayer WS2. *Phys Rev Lett* **113** (2014).
2. K. F. Mak, K. He, C. Lee, G. H. Lee, J. Hone, T. F. Heinz, J. Shan, Tightly bound trions in monolayer MoS 2. *Nat Mater* **12**, 207–211 (2013).
3. S. Dal Conte, C. Trovatello, C. Gadermaier, G. Cerullo, Ultrafast Photophysics of 2D Semiconductors and Related Heterostructures. Cell Press [Preprint] (2020). https://doi.org/10.1016/j.trechm.2019.07.007.
4. B. Peng, P. K. Ang, K. P. Loh, Two-dimensional dichalcogenides for light-harvesting applications. *Nano Today* **10**, 128–137 (2015).
5. J. Gusakova, X. Wang, L. L. Shiau, A. Krivosheeva, V. Shaposhnikov, V. Borisenko, V. Gusakov, B. K. Tay, Electronic Properties of Bulk and Monolayer TMDs: Theoretical Study Within DFT Framework (GVJ-2e Method). *Physica Status Solidi (A) Applications and Materials Science* **214**, 1–7 (2017).
6. A. Carvalho, R. M. Ribeiro, A. H. Castro Neto, Band nesting and the optical response of two-dimensional semiconducting transition metal dichalcogenides. *Phys Rev B Condens Matter Mater Phys* **88** (2013).
7. Enyashin, A., Seifert, G., Enyashin, A. N., & Seifert, G. Electronic properties of $MoS_2$ monolayer and related structures. *Nanosyst.: Phys. Chem. Math*. **5**, 517–539 (2014).
8. C. Zhang, A. Johnson, C. L. Hsu, L. J. Li, C. K. Shih, Direct imaging of band profile in single layer MoS2 on graphite: Quasiparticle energy gap, metallic edge states, and edge band bending. *Nano Lett* **14**, 2443–2447 (2014).

9. G. Wang, A. Chernikov, M. M. Glazov, T. F. Heinz, X. Marie, T. Amand, B. Urbaszek, Colloquium: Excitons in atomically thin transition metal dichalcogenides. *Rev Mod Phys* **90**, 21001 (2018).

10. S. Brem, M. Selig, G. Berghaeuser, E. Malic, Exciton Relaxation Cascade in two-dimensional Transition Metal Dichalcogenides. *Sci Rep* **8**, 1–8 (2018).

11. P. D. Cunningham, K. M. McCreary, A. T. Hanbicki, M. Currie, B. T. Jonker, L. M. Hayden, Charge Trapping and Exciton Dynamics in Large-Area CVD Grown MoS2. *Journal of Physical Chemistry C* **120**, 5819–5826 (2016).

12. D. Andrzejewski, M. Marx, A. Grundmann, O. Pfingsten, H. Kalisch, A. Vescan, M. Heuken, T. Kümmell, G. Bacher, Improved luminescence properties of MoS2 monolayers grown via MOCVD: Role of pre-treatment and growth parameters. *Nanotechnology* **29** (2018).

13. L. Wang, J. B. Sambur, Efficient Ultrathin Liquid Junction Photovoltaics Based on Transition Metal Dichalcogenides. *Nano Lett* **19**, 2960–2967 (2019).

14. M. X. Tan, P. E. Laibinis, S. T. Nguyen, J. M. Kesselman, C. E. Stanton, N. S. Lewis, *Principles and Applications of Semiconductor Photoelectrochemistry* (2007)vol. 41.

15. I. Robel, M. Kuno, P. V. Kamat, Size-dependent electron injection from excited CdSe quantum dots into TiO2 nanoparticles. *J Am Chem Soc* **129**, 4136–4137 (2007).

16. W. A. Tisdale, X. Y. Zhu, Artificial atoms on semiconductor surfaces. *Proc Natl Acad Sci U S A* **108**, 965–970 (2011).

17. B. F. Wright, K. Sunahara, A. Furube, A. Nattestad, T. M. Clarke, G. C. Bazan, J. D. Azoulay, A. J. Mozer, Driving Force Dependence of Electron Transfer Kinetics and Yield

in Low-Band-Gap Polymer Donor-Acceptor Organic Photovoltaic Blends. *Journal of Physical Chemistry C* **119**, 12829–12837 (2015).

18. J. Wu, Y. Huang, W. Ye, Y. Li, CO2 Reduction: From the Electrochemical to Photochemical Approach. Wiley-VCH Verlag [Preprint] (2017). https://doi.org/10.1002/advs.201700194.

19. J. Garoz-Ruiz, J. V. Perales-Rondon, A. Heras, A. Colina, Spectroelectrochemical Sensing: Current Trends and Challenges. Wiley-VCH Verlag [Preprint] (2019). https://doi.org/10.1002/elan.201900075.

20. C. Ruckebusch, M. Sliwa, P. Pernot, A. de Juan, R. Tauler, Comprehensive data analysis of femtosecond transient absorption spectra: A review. *Journal of Photochemistry and Photobiology C: Photochemistry Reviews* **13**, 1–27 (2012).

21. T. Borzda, C. Gadermaier, N. Vujicic, P. Topolovsek, M. Borovsak, T. Mertelj, D. Viola, C. Manzoni, E. A. A. Pogna, D. Brida, M. R. Antognazza, F. Scotognella, G. Lanzani, G. Cerullo, D. Mihailovic, Charge photogeneration in few-layer MoS2. *Adv Funct Mater* **25**, 3351–3358 (2015).

22. H. Shi, R. Yan, S. Bertolazzi, J. Brivio, B. Gao, A. Kis, D. Jena, H. G. Xing, L. Huang, Exciton dynamics in suspended monolayer and few-layer MoS2 2D crystals. *ACS Nano* **7**, 1072–1080 (2013).

# Chapter 3 : EXPERIMENTAL DESIGN[1]

## 3.1 Synopsis

This chapter details material characterization, device construction, and data collection methods. The objective of this chapter is to offer a concise guide through each essential step required to replicate these measurements. Included in this chapter is characterization methods for the 2D TMD thin films, construction of 2D TMD photoelectrochemical cells, electrochemical and photo-electrochemical measurements, potential-dependent absorbance measurements, lock-in detected photocurrent spectroscopy, and transient absorption spectroscopy. Included at the end of this chapter is a discussion of ongoing modifications to the transient absorption spectrometer for future experiments related to this work. Rachelle Austin assembled and characterized photoelectrochemical cells, as well as performed electrochemical and photo-electrochemical measurements and data analysis. Rachelle Austin and Yusef Farah performed transient absorption spectroscopy measurements and TA data analysis.

## 3.2 Characterization of 2D TMD Samples

*Photoluminescence and Raman Spectroscopy*

Monolayer $MoS_2$ films (1 cm x 1 cm, 6Carbon Technology, Shenzhen, China) were synthesized via chemical vapor deposition (CVD) on sapphire substrates and mechanically transferred to ITO-coated glass slides using a polymethyl methacrylate stamp and stored in a nitrogen-purged glovebox until use. Raman and photoluminescence (PL) micro-spectroscopy

[1] This chapter contains adaptations from the methods and supplementary information published in Austin, R. Farah, Y. R. Sayer, T. Hot carrier extraction from 2D semiconductor photoelectrodes. *PNAS*, 120 (15) 2023.

experiments were done to quantify the quality and layer-thickness of the commercial samples (Figure 3-1).

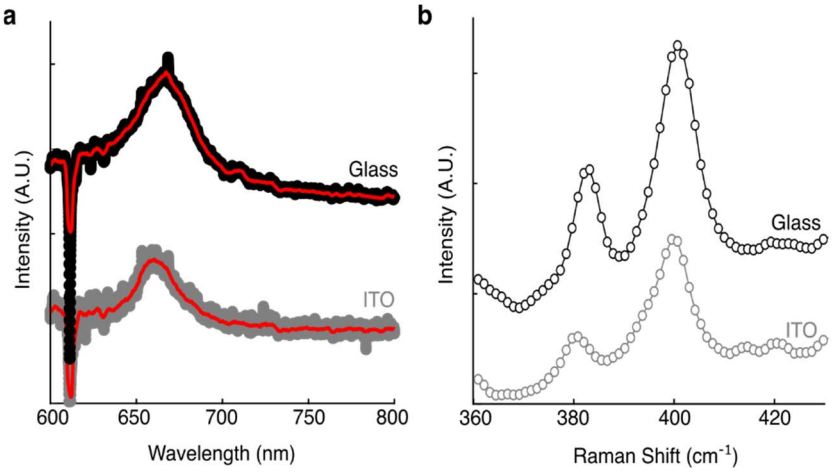


Figure 3-1. (a) Photoluminescence spectra of monolayer $MoS_2$ on glass (black data) and ITO (grey data) in air. The red lines represent a 5-point smooth trend line. (b) Raman spectra of monolayer $MoS_2$ on glass (black data) and ITO (grey data).

The PL and Raman spectra were measured on an inverted Olympus IX73 optical microscope by directing an Ondax 532 nm laser excitation source through a 100× NA0.95 air objective (Olympus PlanFL N100X) onto the sample. Both signals were collected in a backscatter geometry, filtered by the Ondax 532 nm THz Raman system to remove the fundamental excitation light, passed through a Horiba iHR 550 spectrometer, and then detected by a Synapse charge-coupled device detector. The PL peak at 660 nm (1.88 eV) is consistent with ML-MoS2 (*1*). The PL intensity is quenched on the conducting ITO substrate, likely due to additional recombination pathways or charge transfer on ITO (*2*). The Raman peaks at 380 $cm^{-1}$ and 400 $cm^{-1}$ are the $E_{2g}{}^1$ and $A_{1g}$ modes of ML-$MoS_2$, respectively, and the 20 $cm^{-1}$ Raman peak-splitting is consistent with ML-$MoS_2$ (*1*). PL and Raman spectra were measured both before and after transient absorption measurements

*Spatially-resolved UV-Vis Absorbance Spectroscopy*

Visible light absorption of ML-$MoS_2$ samples were collected on a microscope to test for spatial variation of optical density. Samples were excited via monochromatic light from a Horiba OBB Tunable PowerArc Illuminator. A 20× microscope objective collected the light transmitted through the sample and a Photometrics Prime 95B back illuminated complementary metal–oxide–semiconductor (CMOS) camera acquired widefield images of the sample at different monochromatic excitation wavelengths. A representative widefield image is shown in Figure 3-2a.

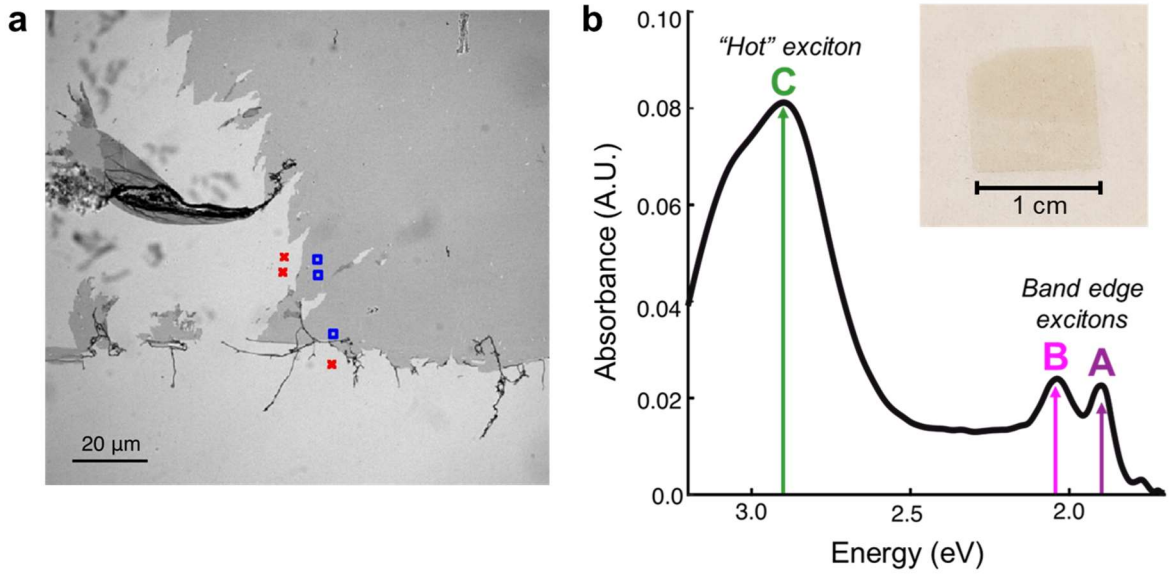


Figure 3-2. a) Optical microscope image of ML-$MoS_2$ on ITO. b) Measured absorbance spectrum of ML-$MoS_2$ on ITO.

Absorbance spectra were calculated from the hyperspectral imaging data by spatially selecting the light transmitted through the sample ($I$) and the ITO substrate ($I_0$), where $A(\lambda) = -\log_{10}(I(\lambda)/I_0(\lambda))$. Figure 3-2a shows representative pixels used as $I$ (blue squares) and $I_0$ (red squares) for absorbance spectra calculations. The images and absorbance data were acquired at the film edge to obtain $I_0$ measurements. All other spectroscopic data were acquired in the film interior,

where the sample morphology is >90% pure ML-$MoS_2$. An image of the entire 1 cm x 1 cm ML-$MoS_2$ film is shown in the inset of Figure 3-2b.

The measured absorbance spectrum of ML-$MoS_2$ from our hyperspectral imaging process is plotted in Figure 3-2b. There are three notable features in this spectrum, labelled as A-, B-, and C-exciton "peaks." These features are excitonic transitions that arise from electrons in the valence band of ML-$MoS_2$ absorbing photons to transition to higher energy states in the conduction band. The positive hole in the valence band is coulombically bound to the electron in the conduction band to form an exciton. It has been well-reported that excitons in 2D TMDs are strongly bound and dominate the optical spectrum at room temperature (*3*, *4*). The band-edge A- and B-excitons have energies of 1.88 eV (655 nm) and 2.01 eV (620 nm) respectively and are split due to spin-orbit coupling in the valence band (*5*). The high energy C-exciton has energy of 2.98 eV (435 nm) and arises due to band nesting of the valence and conduction bands (*6*). The C-exciton has significantly larger absorbance than the band-edge excitons, contributing to the three-atom thin monolayer absorbing nearly 10% of visible light (*7*), making the 1 cm x 1 cm films used in our experiments visible to naked eye, as shown in the Figure 3- inset.

**3.3 Construction of optically transparent photoelectrochemical cells**

The 1 cm x 1 cm $MoS_2$ films on ITO were constructed into optically transparent three-electrode microfluidic flow cells as described in our previous publications (*8–10*). The design of the cell is shown in Figure 3-3. Inlet and outlet ports for electrolyte flow through the cell were achieved by drilling holes in the ITO substrate and inserting Teflon tubing into the holes. Two pieces of approximately 50 μm-thick polytetrafluorethylene (PTFE) spacers were placed between the ITO substrate and a glass coverslip (Thermo Scientific) to form a microfluidic channel. An electrode chamber containing an Ag/AgI reference electrode and Pt counter electrode was attached

to the outlet port. All components were attached and sealed with Loctite epoxy. Aqueous electrolyte solution (1M NaI, Fisher Scientific) was flowed through the cell at a constant rate of 0.5 mL/hr using a Kent Scientific syringe pump. After experiments, the flow cells were prepared for storage by flowing approximately 20 mL of 18.2 MΩ ultrapure water through the flow cell at a rate of 5 mL/hour to remove iodine residue, then drying in air.

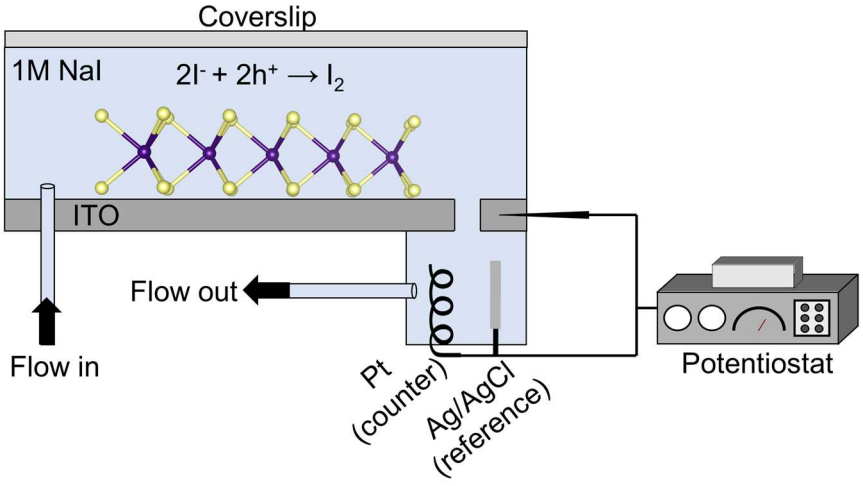


Figure 3-3. Scheme of the photoelectrochemical cell construction.

### 3.4 Photoelectrochemical characterization

All electrochemical measurements were made using an Ivium Compactstat Potentiostat in a 3-electrode configuration. The open circuit potential of the $MoS_2$|1M $I^-$ cell was measured as 0.27 V vs. Ag/AgI.

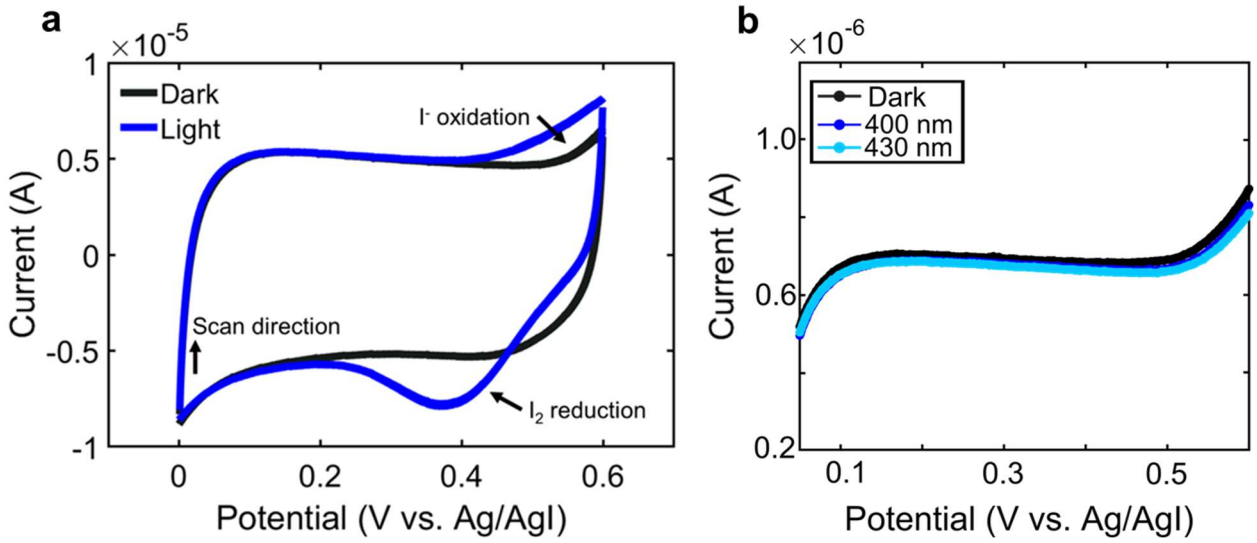


Figure 3-4. a) Cyclic voltammogram of ML-$MoS_2$ photoelectrochemical cell with no illumination (black trace) and under white light illumination (blue trace). Increased anodic current is seen under illumination at potentials > 0.4 V vs. Ag/AgI. The corresponding reduction of $I_2$ in the CV is shown on the return scan. b) Control current response of a bare ITO electrode in 1 M NaI electrolyte under C-exciton peak wavelength illumination (430 nm, 20 μW), 400 nm illumination, and dark conditions.

Cyclic voltammograms (CVs) were taken to determine onset potentials of photoelectrochemical reactions. Representative CVs of the ML-$MoS_2$ photoelectrochemical cell under no light (dark) and white light illumination conditions are shown in Figure 3-4a. We assigned anodic (positive) current to iodide oxidation at the working electrode (the $MoS_2$-ITO electrode) in accordance with previous work (*8*). We assigned reductive (negative) current to iodine reduction. Figure 3-4b shows a control experiment of a bare ITO electrode in 1M NaI under multiple illumination conditions. No photo-induced current of bare ITO is observed. Notably, the magnitude of dark current from the bare ITO is an order of magnitude less than the current of the $MoS_2$-ITO electrode in Figure 3-4a.

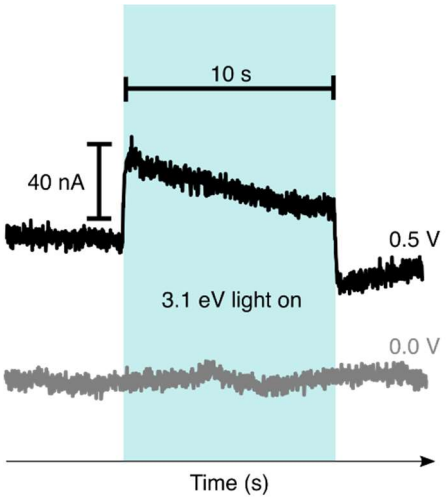


Figure 3-5. Photocurrent onset with 400 nm (3.1 eV) light excitation. Observation of a potential-dependent photocurrent generated by the transient absorption pump laser (3.1 eV) in the monolayer $MoS_2$ photoelectrochemical cell.

We performed chopped-light experiments to observe the magnitude of photo-induced current (photocurrent) at different applied voltages. A constant potential was applied to the ML-$MoS_2$ working electrode while a 400 nm light source was focused onto the ML-$MoS_2$ and chopped in 10 second on/20 second off increments. The current response was recorded. At low applied potentials, no photocurrent was observed (grey data in Figure 3-5). At sufficiently high applied potentials, current induced by the light source was measured (black data in Figure 3-5), indicating the dependence of the anodic iodide oxidation on photogenerated charge carriers from the illuminated ML-$MoS_2$.

### 3.5 Potential-dependent optical absorbance measurements

Potential-dependent absorbance measurements were performed by collecting spatially-resolved UV-Vis absorbance spectra of the ML-$MoS_2$ within the photoelectrochemical cell. The working electrode was held at a fixed potential versus the Ag/AgI reference electrode during the entirety of the absorbance measurement. The applied potential, images, and monochromator output

were synced in time using a data acquisition card (DATAQ Instruments). The in-situ absorbance was taken at applied potentials ranging from 0.00 V to 0.55 V vs. Ag/AgI in steps of 0.025 V. The Matlab code used to process potential-dependent absorbance data and produce Figure 3-6 is given in Appendix II. Multiple spectra at each applied potential were taken across multiple days and samples to test for sample stability and degradation. No changes in the absorbance spectrum were observed after multiple days of experiments.

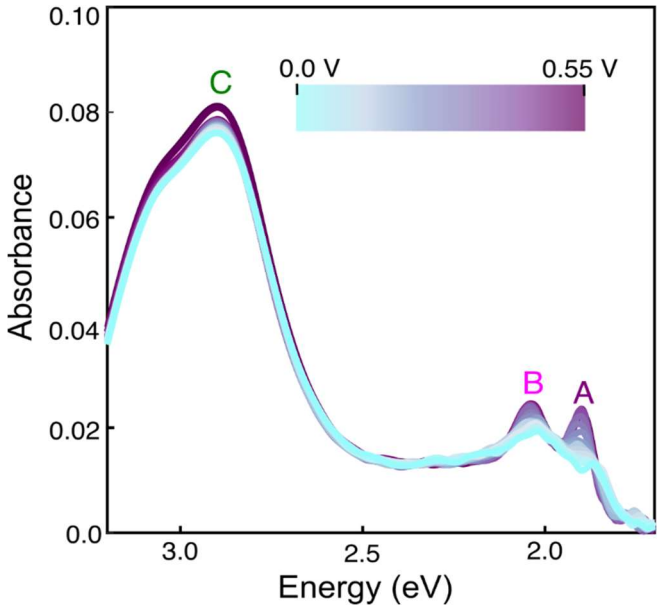


Figure 3-6. Potential-dependent absorbance spectra of the ML-$MoS_2$ photoelectrochemical cell in 0.025 V increments from 0.00 V to 0.55 V.

### 3.6 Photocurrent spectroscopy

A lock-in amplifier was used to detect small photocurrents from the ML-$MoS_2$, which were typically on the order of nanoamps at low voltages. A chopper was placed between the light source and the sample and chopped the light at 10 Hz. The current output from the potentiostat was connected to the input channel of a Stanford Research Systems SR830 lock-in amplifier. The light source was scanned from 750 nm to 375 nm in 1 nm steps. The detected lock-in current and

monochromator output were synced in time using a data acquisition card (DATAQ Instruments). A schematic of the lock-in photocurrent spectroscopy setup is given in Figure 3-7.

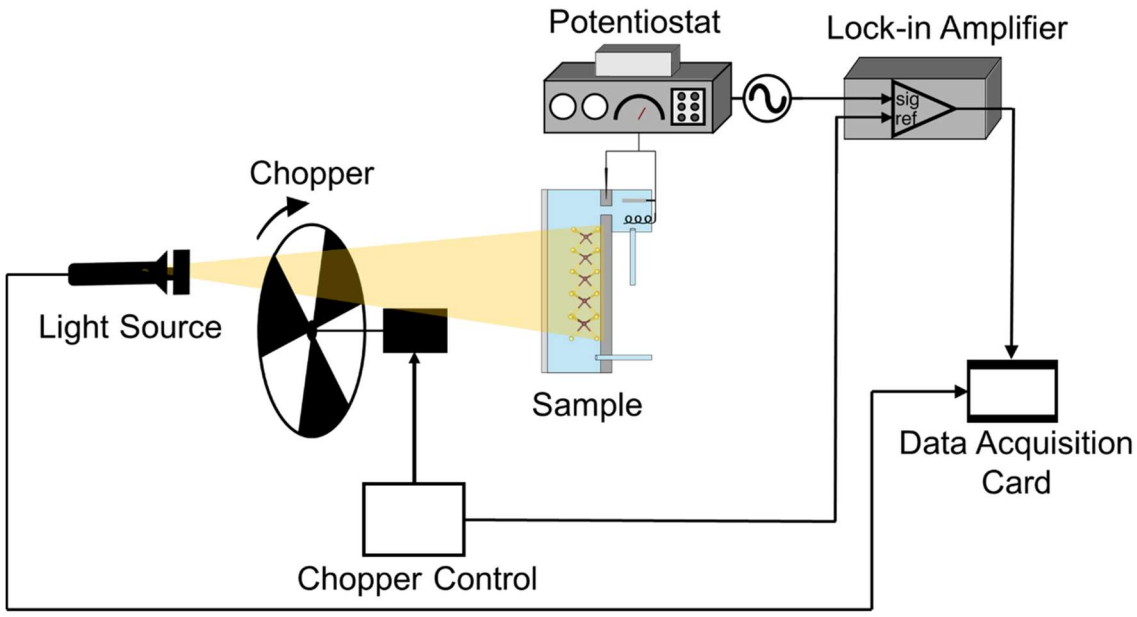


Figure 3-7. Diagram of light source, chopper, sample, lock-in amplifier, and DAQ card setup for photocurrent lock-in detection (not to scale).

The lock-in signal was converted from arbitrary units to units of amperes through calculation of the lock-in proportionality constant. The lock-in amplifier signal is proportional to the photocurrent magnitude. The lock-in proportionality constant is calculated by measuring the photocurrent response of the sample under identical conditions with and without the lock-in amplifier.

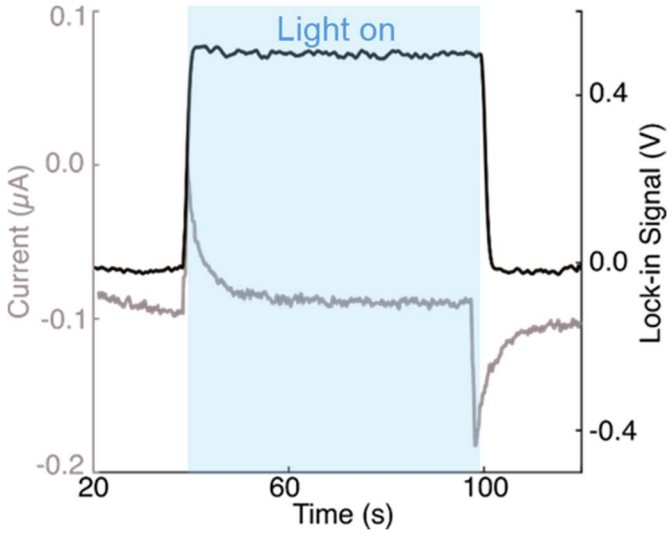


Figure 3-8. Comparison of steady-state current (grey, left-axis) with lock-in current (black, right axis) for determination of lock-in proportionality constant. Both signals are measured with the same photoelectrochemical cell with the same applied bias and identical illumination.

First, the steady state photocurrent was measured by recording the current response at 0.5 V vs. Ag/AgI using the potentiostat and illuminating the sample with white light (grey trace in Figure 3-8). The sample was then hooked up to the lock-in amplifier and the photocurrent response of the sample at the sample applied voltage with chopped illumination was recorded (black trace in Figure 3-8). The peak in the steady state current signal (in A) divided by the lock-in signal magnitude (in V) gives the proportionality constant in A/V.

The wavelength-dependent photocurrent response (photocurrent spectra) of the monolayer $MoS_2$ photoelectrochemical cells were acquired by applying a fixed potential to the $MoS_2$-ITO working electrode and measuring the resulting current as a function of monochromatic illumination wavelength. The light source used was a Horiba OBB Tunable PowerArc Illuminator. The light source was set up to illuminate the entire sample area in order to maximize the photocurrent signal. Monochromatic current-voltage curves were measured from 0.00 V to 0.55 V vs. Ag/AgI while monochromatic light resonant with the A-, B-, or C-excitons (1.87 eV, 2.11

eV, and 2.98 eV, respectively) illuminated the sample. The Matlab code used to process photocurrent data and produce the following figures is given in Appendix II.

Photocurrent spectra (Figure 3-9a) and monochromatic current vs. potential curves (Figure 3-9b) were converted to external quantum efficiency (EQE). EQE is calculated from the equation

$$\mathrm{EQE}(\lambda) = \frac{i}{qI_o}, \qquad Eq.3-1$$

where $i$ is the photocurrent in units of C/s (Amperes), $q$ is the elementary charge in units of C, and $I_0$ is the incident laser power measured at the cover glass in units of (photons $s^{-1}$).

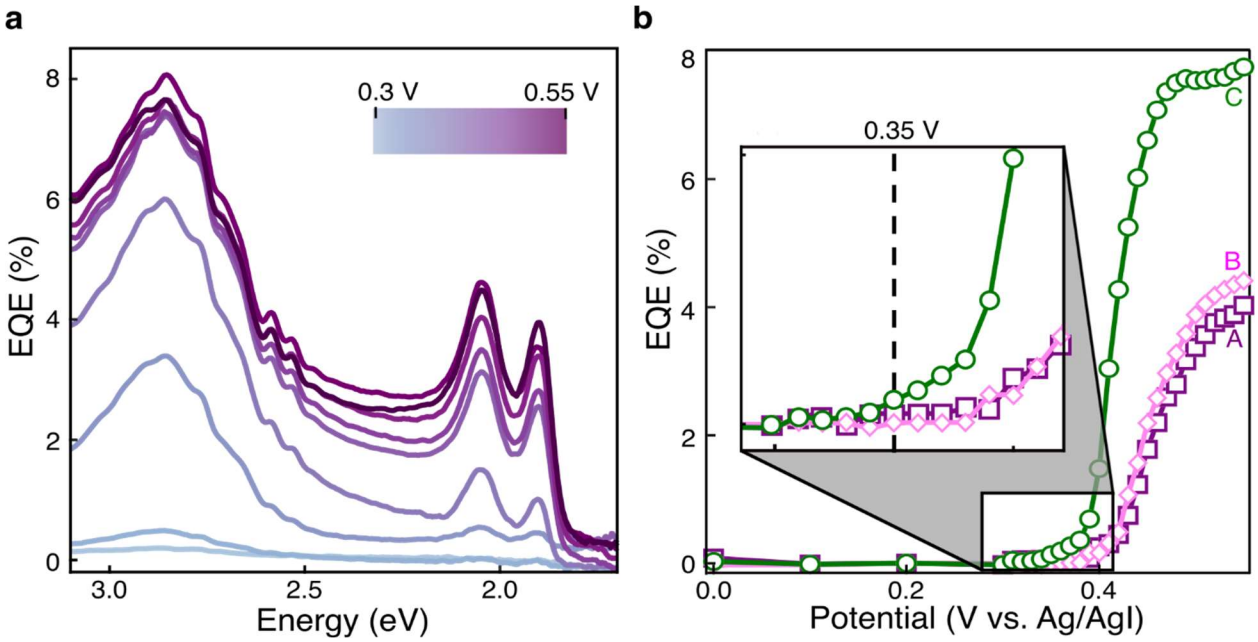


Figure 3-9. (a) EQE spectra vs. applied potential from 0.35 V to 0.55 V in 0.025 V increments. (b) Monochromatic i-E (current-voltage) measurements for resonant A-, B-, and C-exciton excitation (i.e., 650 nm, 605 nm, and 432 nm, respectively).

The photocurrent response of the $MoS_2$ photoelectrochemical cell as a function of wavelength was used to observe at which potentials the different excitons dissociate and contribute to current flow in the cell. It is important to note that the measured current response is a direct

measurement of the number of free electrons/holes and not bound excitons, so this technique reports only on free charge carrier dynamics and not on exciton dynamics. The photocurrent spectra shown in Figure 3-9a closely resemble the absorbance spectrum in Figure 3-2b, indicating that the applied potential generates a robust interfacial electric field, leading to the effective dissociation of all three excitonic species. Increasing the applied potential results in a higher yield of dissociated charge carriers and consequently a higher current. Notably, when light resonant to the C-exciton (425 nm) is used for excitation, the maximum current response is recorded, thereby indicating the maximum extraction of free charge carriers. Differences in the photocurrent onset potential for the A-, B-, and C-excitons are shown in monochromatic current-voltage curve measurements (Figure 3-9b). Notably, photocurrent generation onsets at less positive potentials for the C-exciton, and the slope of its current-voltage curve is notably steeper than that of the A-/B-excitons. Importantly, photocurrent is not observed when directly exciting the A/B-excitons at the same applied potential as that of the C-exciton (specifically E = 0.35 V in Figure 3-9b). Further discussion of this data is provided in Chapter 4.

### 3.7 Ultrafast transient absorption spectroscopy

Transient absorption measurements were performed with a home-built, femtosecond, pump-probe spectrometer (shown in Figure 3-10). Compressed light from a Ti:sapphire regenerative amplifier (Wyvern 1000, KM Laboratories) produced sub-50 fs pulses centered at 790 nm carrying 3.3 mJ of energy per pulse at a repetition rate of 1kHz. Front reflections off a beam splitter and wedged $CaF_2$ plate were used to lower the light intensity before splitting the light with a half-wave plate ($\lambda/2$) and polarizer. A fraction of the light was sent through a delay stage controlled by a Newport motion controller driver (XPS model) to control timing and then directed onto a 1 mm beta barium borate (BBO) crystal to frequency double the light by second harmonic

generation to 395 nm. The 395 nm light served as the pump pulse in TA measurements. A tunable neutral density (ND) filter was used to adjust the pump fluence.

The probe pulse was created by taking the remaining portion of the split light and focusing it down in a 2 mm quartz cuvette filled with 18.2 MΩ ultrapure water, creating a white-light continuum spanning 400 nm to 800 nm. The pump and probe pulses were focused down to a spot size of approximately 30 $\mu$m full-width half-max (FWHM) and overlapped at the sample in a non-collinear beam geometry. A Mightex CMOS camera was used to overlap the pump and probe bemas at the sample position. The temporal overlap of the pump and probe beams was collected by scattering the 800 nm fundamental light of the pump and probe beams off of a glass microscope slide and measuring the resulting interferogram of the two beams. The probe light transmitted through the sample was collected, collimated, and focused into a spectrometer (iHR550, Horiba) with a 200 mm slit opening, equipped with a 100 line/mm grating (450 blaze), and detected by a single line 2048 element array detector (OctoPlus, Teledyne e2V) with an exposure time of 1.3 μs. The spectrometer was calibrated with a neon spectral calibration lamp (Oriel Instruments). The spectral and temporal resolution of the setup was 0.6 nm and ~50 fs, respectively. The pump pulse was modulated by an optical chopper (Thorlabs) triggered by the pump laser and set to operate at half the repetition rate of the laser (500 Hz). The spectrally resolved "pumped" ($I^*(\lambda, \tau)$) and "unpumped" ($I_0(\lambda)$) signals are acquired and used to calculate the ΔA spectrum.

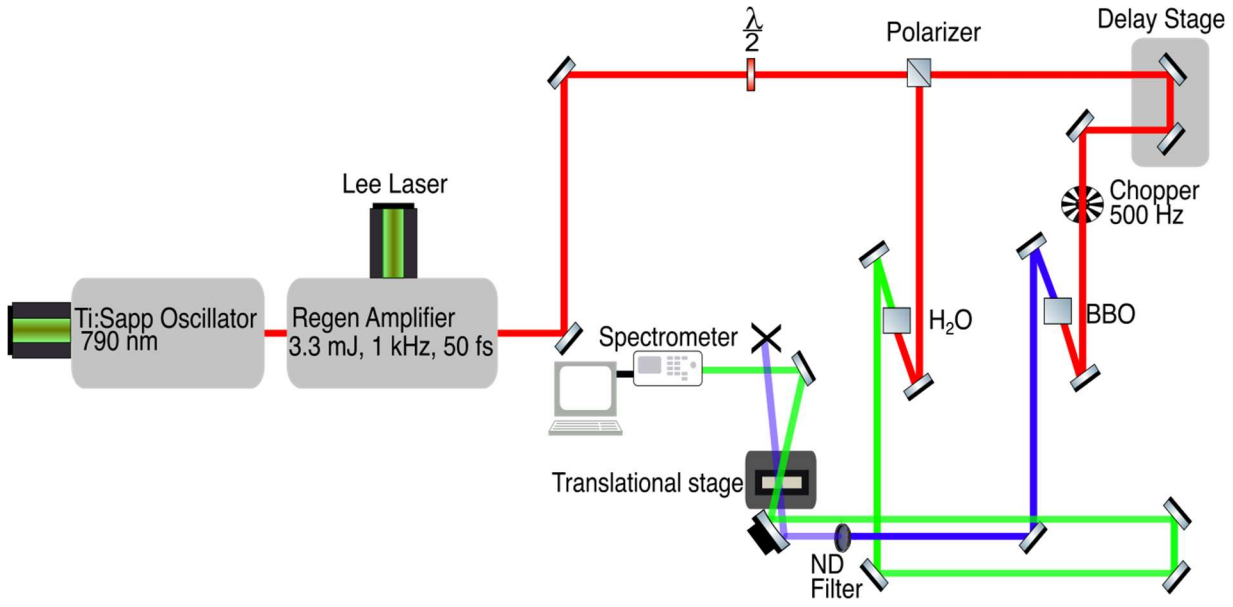


Figure 3-10. Transient absorption spectrometer optical table layout.

*Pump fluence measurements*

The transient absorption signal of monolayer $MoS_2$ on ITO was measured as a function of pump fluence (calculated using the half-width half-maximum as the radius of the beam) to determine the optimal fluence for our experiments. The time delay between pump and probe was kept fixed while the power of the pump beam was modulated with a variable ND filter. The pump fluence was calculated with the equation

$$pump\ fluence = \frac{Energy\ per\ pulse}{\pi * (beam\ radius)^2} \qquad Eq. 3-2$$

for the Gaussian beam profile. The power was measured with a laser power meter (Thorlabs) and the beam radius was measured from the spatial profile of the beam at the sample position with a CMOS camera (Mightex).

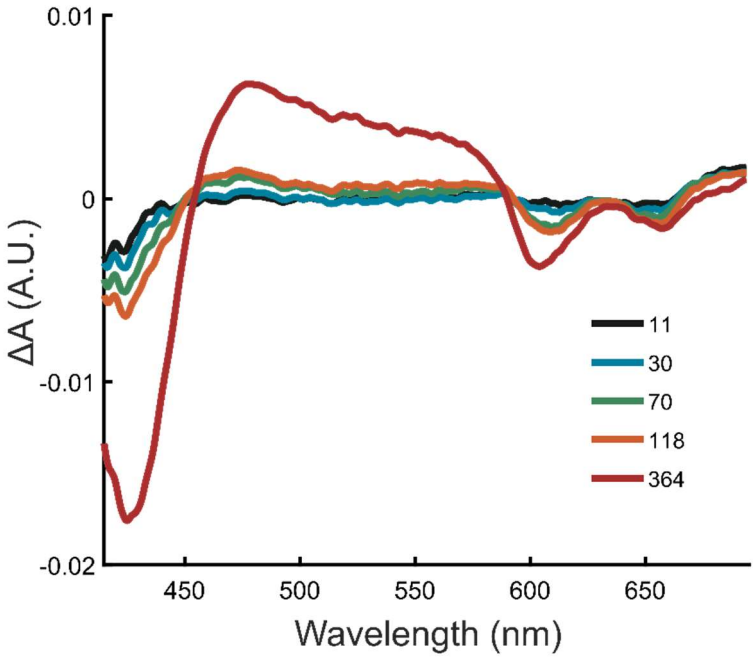


Figure 3-11. Wavelength-resolved transient absorption signal of monolayer $MoS_2$ on ITO at 0.6 ps time delay at different fluences (listed fluences have units of μJ $cm^{-2}$).

Figure 3-11 shows the transient absorption spectra for the five pump fluences at the peak signal intensity time delay (0.6 ps). The photobleach signal of the A, B, and C excitons increases with pump fluence. When first-order recombination mechanisms dominate, the photobleach signal increases linearly with pump fluence (*11*). At high pump fluence, many-body recombination mechanisms like Auger recombination and exciton-exciton annihilation become major decay pathways and the photobleach signal deviates from linearity with the pump fluence (*12*).

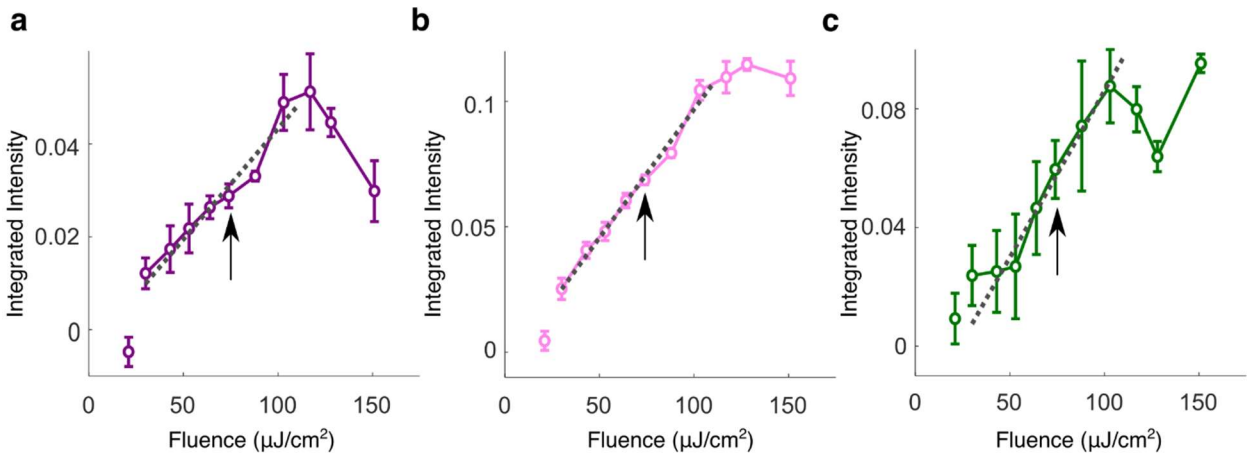


Figure 3-12. Pump fluence dependence of integrated excitonic bleach peak intensity (at a probe delay of 1 ps) for the (a) A-exciton, (b) B-exciton, and (c) C-exciton. The black arrow highlights the pump fluence of 75 $\boldsymbol{\mu}$J/cm$^2$ that was chosen for all in situ TA data.

To determine the range of pump fluences over which the induced change in the TA signal scales linearly, we integrated the area under each exciton photobleach under different pump fluence conditions. Figure 3-12 shows that the integrated photobleach signal of all excitons is linear below 118 μJ cm$^{-2}$ thus, all potential-dependent transient absorption experiments were carried out at 75 μJ cm$^{-2}$, within the regime of linear pump fluence dependence. The TA bleach intensities are non-linear with pump fluences when the pump fluence exceeds 100 $\boldsymbol{\mu}$J/cm$^2$, in agreement with literature (*13*). We also note that the data point at 20 μJ/cm$^2$ is at the detection limit for our system, so we do not include it in the linear-dependence evaluation. The probe fluence was set to the lowest fluence with a reasonable signal-to-noise response on our detector (115 μJ cm$^{-2}$).

*Ex-situ control measurements of ML-$MoS_2$*

The transient absorption of monolayer $MoS_2$ on bare ITO was measured as a function of time delay from -0.2 picoseconds (ps) to 200 ps to determine exciton energies and decay constants in the absence of electrolyte and applied potential.

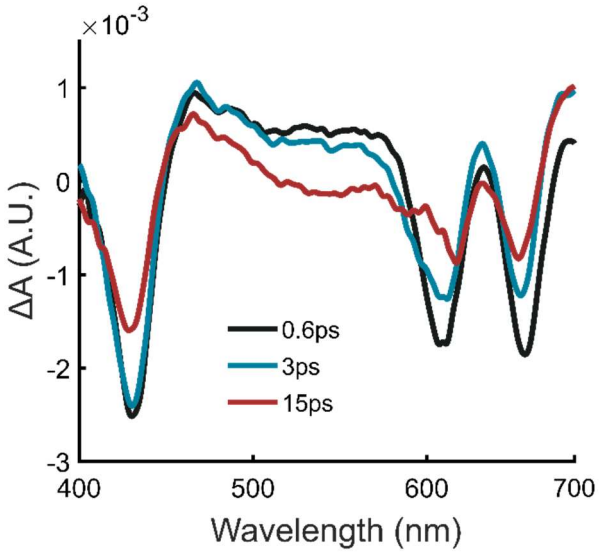


Figure 3-13. Control measurement of wavelength-resolved transient absorption signal of monolayer $MoS_2$ on ITO at various time delays.

Figure 3-13 shows three negative ΔA peaks which correspond to photobleaching (PB) of the A, B, and C excitons based on the steady-state absorption shown in Figure 3-2b. These PB peaks are consistent with previous transient absorption experiments on monolayer $MoS_2$ (*11*, *14*, *15*).

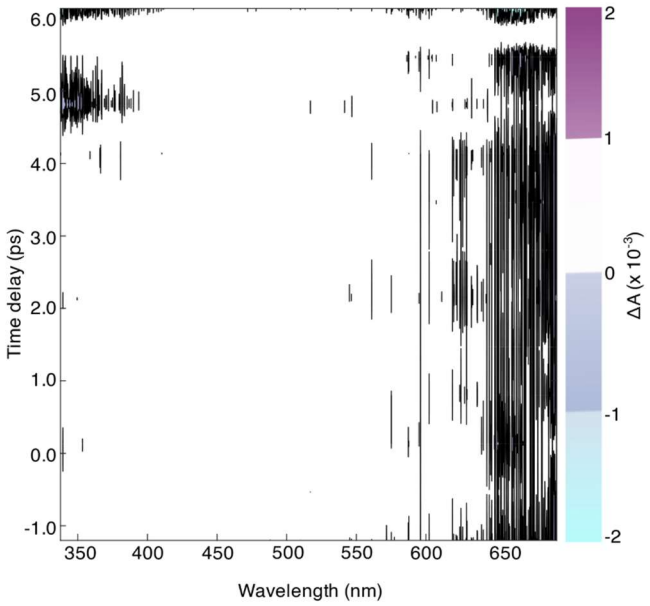


Figure 3-14. Control measurement of transient absorption signal of a bare ITO electrode in 1M NaI under 3.1 eV pump illumination.

Figure 3-14 shows the transient absorption signal taken of a blank photoelectrochemical cell (i.e. all components of the cell minus the ML-$MoS_2$ sample). No transient absorption signal from the bare ITO or electrolyte was measured.

*In-operando TA measurements of ML-$MoS_2$*

We used *in-operando* TA spectroscopy on ML-$MoS_2$ photoelectrochemical cells to collect TA spectra as a function of both time delay (to observe exciton dynamics) and as a function of applied voltage (to compare dynamics under a range of charge extraction conditions). The TA spectra as a function of applied potential is shown in Figure 3-15. The spectra shown were all collected at a time delay of 1 ps.

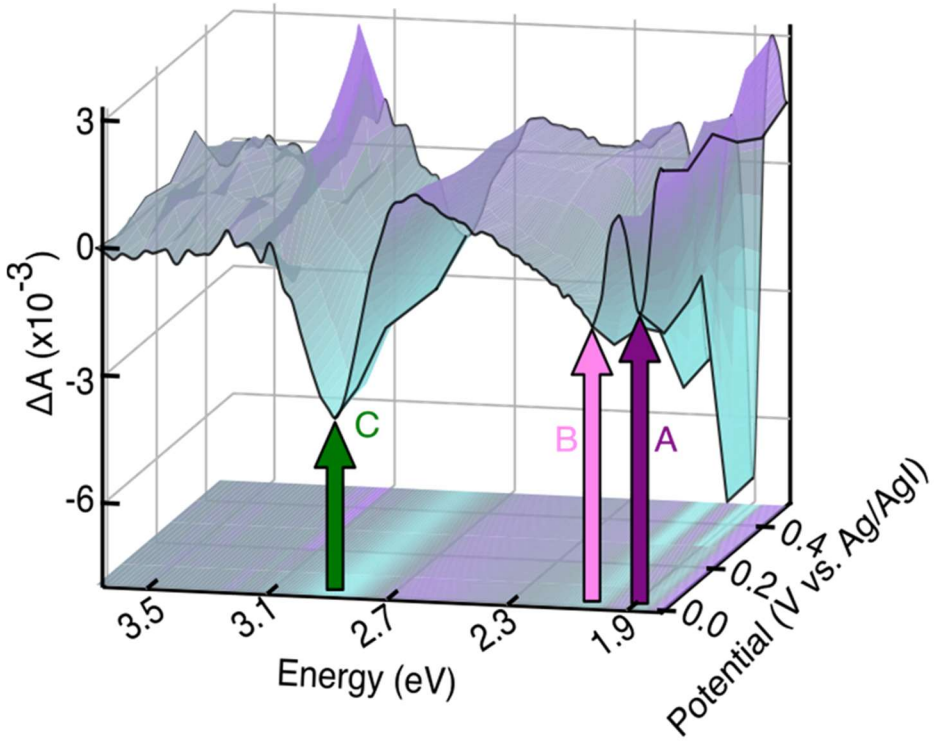


Figure 3-15. Potential-dependent TA spectra at τ = 1 ps.

### 3.8 TA Temporal Decay Analysis

Analysis of the transient absorption data for the publication "Hot Carrier Extraction from 2D Semiconductor Photoelectrodes" is provided here. A more detailed analysis of the A-exciton peak, its spectral fitting, and its decay analysis are given in Chapter 5.

Following literature (*11*, *16*), the A-exciton and B-exciton bleach intensity versus time data were fit using a tri-exponential function convoluted with a rising exponential of the form

$$\Delta A(\lambda, t) = A_0 + \left(\sum_{i=1}^{3} A_i(\lambda) \cdot exp\left(-\frac{t}{\tau_i}\right)\right) \cdot \left(A_4 - exp\left(-\frac{t}{\tau_4}\right)\right). \qquad Eq.\ 3-3$$

The fast, medium, and slow components of the triexponential decay have been assigned to defect and carrier-carrier scattering, carrier-phonon scattering, and electron-hole recombination processes (*4*). The rising exponential function captures the exciton formation process.

The C-exciton TA data could be fit with a biexponential function convoluted with the instrument response function of the TA spectrometer:

$$\Delta A(\lambda, t) = A_0 + \sum_{i=1}^{2} \frac{A_i(\lambda)}{2} \cdot exp\left(\left(-\frac{1}{\tau_i}\right)\left(t - \frac{\sigma^2}{2\tau_i}\right)\right) \cdot \left(1 - erf\left(\frac{t - \sigma^2}{\sqrt{2}\sigma\tau_i}\right)\right). \quad Eq. 3-4$$

The fast and slow components of the C-exciton decay dynamics have been assigned to carrier-phonon scattering and intervalley relaxation processes. For all fits, a static offset ($A_0$) is used in the functional form to capture long-lived signal that extends beyond the temporal window of our experiment, in agreement with literature (*17*). Additional fitting methods for this data are described in Chapter 5. Fit constants for the A-, B-, and C-excitons are given in Table 1.

Table 1. Fitting parameters for exciton decay curves. Extracted time constants from A-, B-, and C-exciton temporal decay fits.

| Exciton | Potential (V vs. Ag/AgI) | 0.0 | 0.1 | 0.2 | 0.3 | 0.4 | 0.5 |
|---|---|---|---|---|---|---|---|
| A-exciton | $\tau_1$ (ps) | 0.31 ± 0.05 | 0.24 ± 0.01 | 0.31 ± 0.004 | 0.22 ± 0.03 | 0.18 ± 0.009 | 0.21 ± 0.004 |
| | $\tau_2$ (ps) | 3.5 ± 1 | 3.7 ± 0.1 | 11 ± 0.07 | 4.4 ± 2 | 10 ± 0.7 | 9.5 ± 0.7 |
| | $\tau_3$ (ps) | 22 ± 2 | 45 ± 8 | 130 ± 30 | 82 ± 10 | 260 ± 150 | 220 ± 40 |
| | $\tau_4$ (ps) | 1.1 ± 0.3 | 0.82 ± 0.2 | 0.49 ± 0.04 | 0.64 ± 0.06 | 0.36 ± 0.02 | 0.54 ± 0.05 |
| B-exciton | τ1 (ps) | 0.24 ± 0.04 | 0.35 ± 0.02 | 0.30 ± 0.03 | 0.22 ± 0.02 | 0.20 ± 0.002 | 0.23 ± 0.01 |
| | τ2 (ps) | 4.0 ± 1 | 7.2 ± 0.02 | 8.1 ± 2 | 9.6 ± 2 | 9.0 ± 1 | 6.5 ± 1 |
| | τ3 (ps) | 61 ± 16 | 65 ± 24 | 45 ± 4 | 70 ± 27 | 250 ± 170 | 67 ± 8 |

| | | | | | | | |
|---|---|---|---|---|---|---|---|
| | τ4 (ps) | 1.7 ± 0.2 | 1.5 ± 0.2 | 0.47 ± 0.1 | 0.37 ± 0.05 | 0.44 ± 0.002 | 0.66 ± 0.005 |
| C-exciton | τ1 (ps) | 13 ± 5 | 17 ± 2 | 21 ± 2 | 16 ± 7 | 20 ± 4 | 21 ± 5 |
| | τ2 (ps) | 82 ± 40 | 150 ± 30 | 150 ± 20 | 120 ± 20 | 380 ± 110 | 150 ± 40 |

### 3.9 Development Of Pump-Selective Transient Absorption for Heterogeneous 2D-Electrode Photocurrent Mechanism Studies

*Modified spectrometer design*

In the TA experiments discussed in Chapters 4 and 5, the pump energy used to excite all TMD samples was 3.1 eV (395 nm). However, photocurrent measurements presented earlier in this chapter and in Chapter 4 show that monolayer $MoS_2$ exhibits different quantum efficiencies when excited with different wavelengths of light. To determine the mechanism of charge extraction when exciting resonant to the A-exciton versus exciting resonant to the C-exciton, we have modified the spectrometer with the goal of having a tunable pump wavelength to do pump-selective measurements.

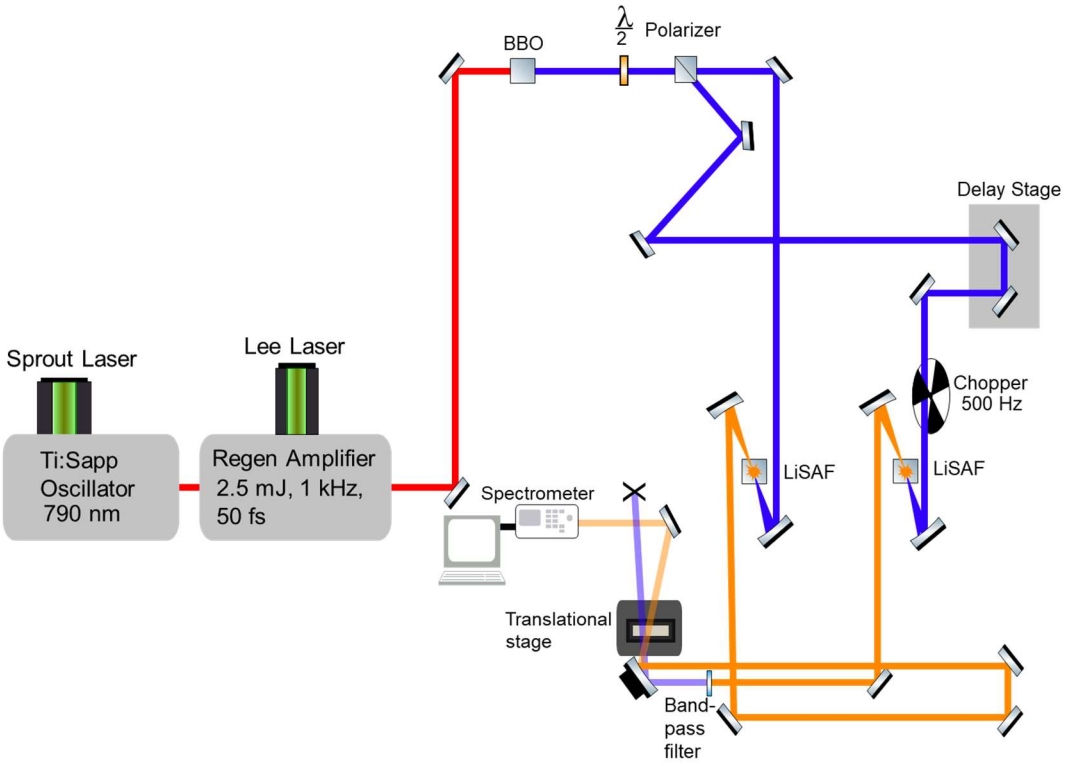


Figure 3-16. Schematic of the new transient absorption spectrometer layout.

The altered spectrometer layout includes three significant alterations shown in Figure 3-16. The first is the frequency-doubling of the fundamental 790 nm beam. This will be done by sending the full power of the beam collimated through a large area BBO (Eskma Optics) to achieve a moderate fluence. The 395 nm doubled light is then split into pump and probe lines with a half-waveplate and thin-film polarizer. The second alteration is the generation of white light on both the pump and probe lines. White light is still generated on the probe line for broadband probing. On the pump line, a white light pump is generated for the purpose of selecting out specific pump wavelengths using narrowband (10 nm bandwidth) bandpass filters (Andover Corporation). The filter allows for pump-selective measurements (as shown in Figure 3-17) on the ML-$MoS_2$ photoelectrochemical cell devices as well as other samples.

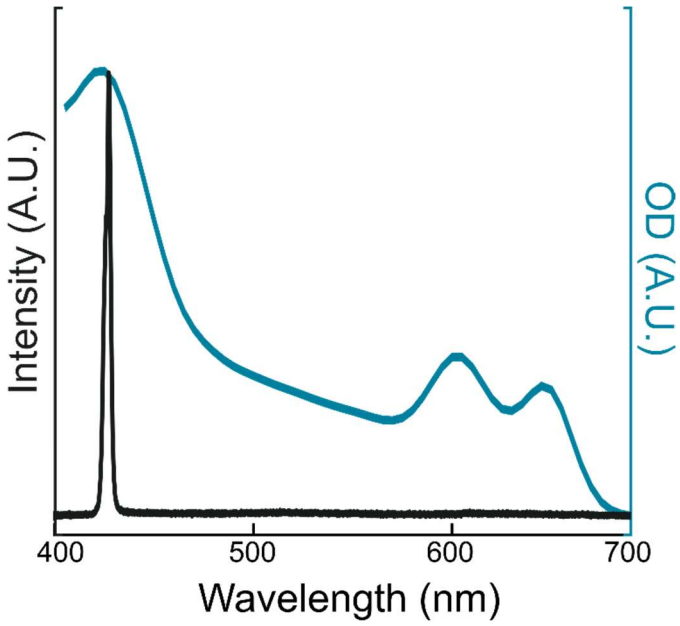


Figure 3-17. Demonstration of pump-wavelength selectivity. A 430 nm bandpass filter in the pump line selects out a narrow range of wavelengths centered at 430 nm (black spectrum). This pump will excite resonant to the C-exciton in ML-$MoS_2$ (shown in the OD spectrum plotted in blue).

The third alteration made to the spectrometer is the medium used for white light generation. In our previous experiments, we used a quartz cuvette filled with ultrapure water for white light generation. It has been shown that solid media typically produces more stable white light output than fluids (*18*), consistent with instability of our white light generated in water. We then searched for an alternative solid material that could produce white light ranging from 400-700 nm.

*White light generation and stability testing*

Efforts to generate broadband white light continuum that is stable and efficient down to 400 nm is a longstanding challenge in the field of ultrafast spectroscopy (*19*, *20*). Recently, LiSAF was found to be an efficient nonlinear material for white light generation down to UV wavelengths (*21*). We tested the stability of this material with our 800 nm, 1 kHz laser system to determine the bandwidth of white light generation and stability on the order of both shot-to-shot and on the order of experiment length.

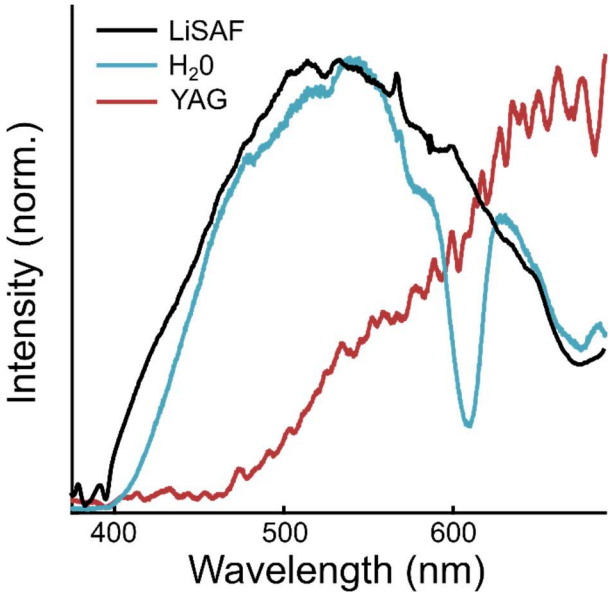


Figure 3-18. Comparison of white light generated by LiSAF (black), water (blue), and YAG (red) on our spectrometer.

The comparison of white light generated by LiSAF on our spectrometer to the other media we have used for white light generation (water and YAG) is shown in Figure 3-18. We found that 5mm-thick LiSAF (Optogama) does generate bluer (400 – 450 nm) light than both water and YAG. We then tested the stability of the generated LiSAF spectrum to quantify signal-to-noise and experimental viability, as TA data collection typically occurs over multiple hours on our system.

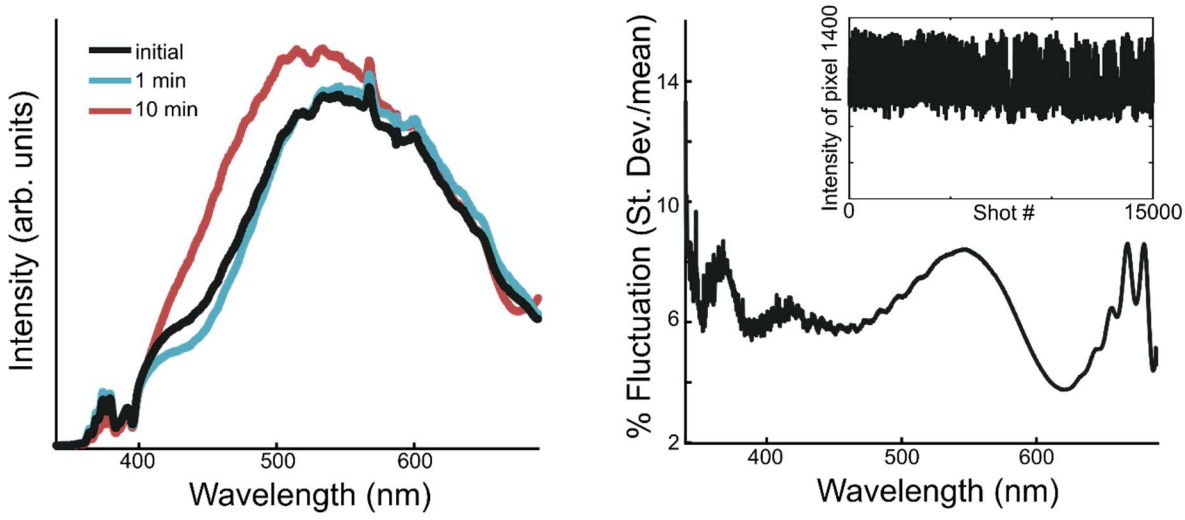


Figure 3-19. Left. The spectrum of white light generated in LiSAF at multiple durations of operation. Right. The percent fluctuation across the LiSAF spectrum for 15,000 consecutive shots. Inset: the intensity of a single pixel on the detector tracked over 15,000 shots.

We observed that the spectrum of the LiSAF output changed over time, as evidenced in Figure 3-19. The spectrum remained stable over the first couple of minutes but increased in fluctuations over longer timescales of 10 minutes to an hour. We observed that the white light would grow more intense and more unstable after multiple minutes of operation, as shown in Figure 3-20 left. Reducing the beam power into the LiSAF appeared to return stability temporarily. Additionally, we found that the fluctuations of the spectrum are wavelength-dependent, meaning that different wavelengths fluctuated in different amounts, as shown in the right panel of Figure 3-20. The next step of this project is to pump LiSAF with the frequency-doubled 400 nm light instead of 790 nm light, as it has been reported that LiSAF produces a more stable supercontinuum output with 400 nm pumping (*21*)

*In-operando imaging of heterogeneous samples*

Our previous experiments used costly large-area CVD-grown 2D TMDs (*22*). A popular lower-cost method to make 2D TMDs is to exfoliate them from bulk samples, or to wet-transfer

them from MOCVD films. However, exfoliation and transfer methods typically produce spatially heterogeneous samples that can have folds, tears, and holes. To be able to perform future measurements of these samples with our TA spectrometer, we must precisely image the pump and probe sample areas to determine if we are on monolayer area, multilayer area, folded area, or any other morphological area of interest. We therefore designed an in-operando imaging technique for the TA spectrometer. The technique images the sample and pump-probe overlap, as shown in Figure 3-20.

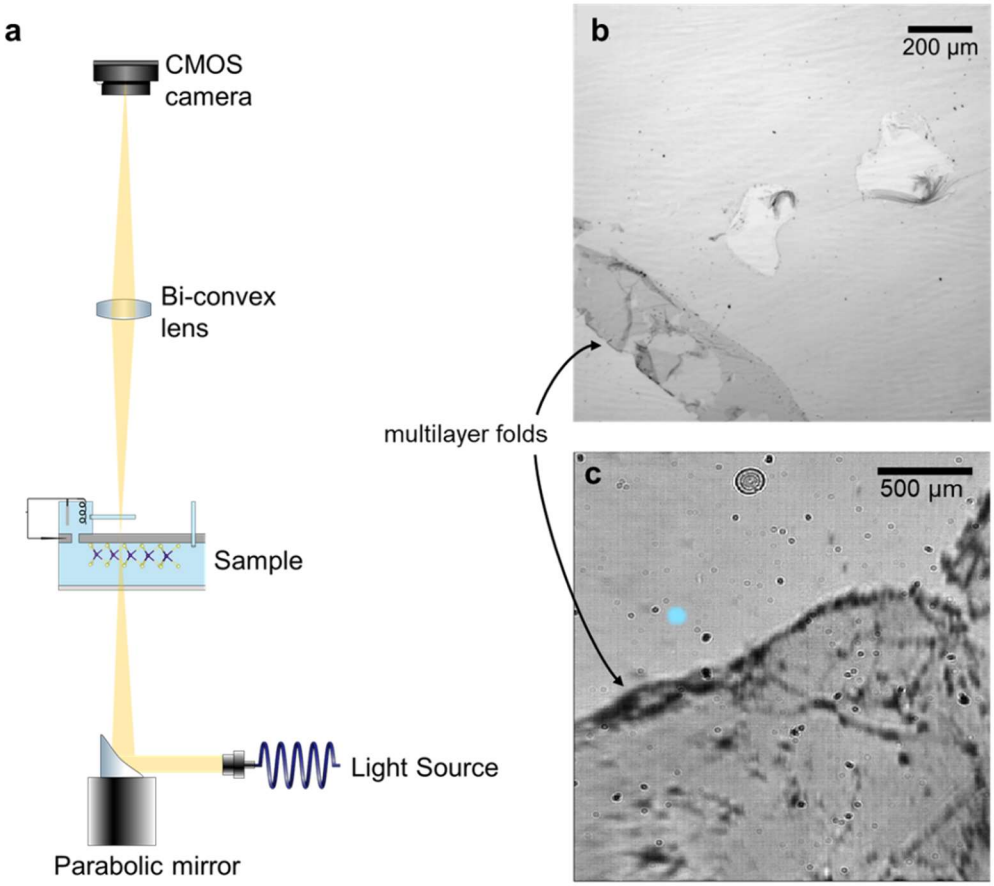


Figure 3-20. a) The imaging setup on the spectrometer. b) A microscope image of a transferred ML-$MoS_2$ sample grown by MOCVD. c) An image of the transferred ML-$MoS_2$ sample taken on the TA spectrometer imaging setup. An image of the pump beam at the sample was taken and overlaid in blue. The pump beam is on the substrate (ITO) for this image.

The imaging technique requires only a light source, a bi-convex lens with 50 mm focal length (Thorlabs), and a CMOS 1280 x 1024 pixel camera (Mightex Systems), assembled as shown in Figure 3-20a. The image technique produces images at 1x magnification and allows for precise alignment of the pump and probe beam onto the sample. As shown in Figure 3-20c, the multilayer folds of the transferred sample can be seen as darker than the monolayer areas. With this technique, transient absorption measurements can be taken at specific morphological areas to determine layer-thickness dependence and edge-vs-interior dependence of exciton dynamics.

**References**


1. C. Lee, H. Yan, L. E. Brus, T. F. Heinz, J. Hone, S. Ryu, Anomalous lattice vibrations of single- and few-layer MoS2. *ACS Nano* **4**, 2695–2700 (2010).
2. C. H. Lee, G. H. Lee, A. M. Van Der Zande, W. Chen, Y. Li, M. Han, X. Cui, G. Arefe, C. Nuckolls, T. F. Heinz, J. Guo, J. Hone, P. Kim, Atomically thin p-n junctions with van der Waals heterointerfaces. *Nat Nanotechnol* **9**, 676–681 (2014).
3. G. Wang, A. Chernikov, M. M. Glazov, T. F. Heinz, X. Marie, T. Amand, B. Urbaszek, Colloquium: Excitons in atomically thin transition metal dichalcogenides. *Rev Mod Phys* **90**, 21001 (2018).
4. S. Dal Conte, C. Trovatello, C. Gadermaier, G. Cerullo, Ultrafast Photophysics of 2D Semiconductors and Related Heterostructures. *Trends Chem* **2**, 28–42 (2020).
5. B. Peng, P. K. Ang, K. P. Loh, Two-dimensional dichalcogenides for light-harvesting applications. *Nano Today* **10**, 128–137 (2015).
6. J. Gusakova, X. Wang, L. L. Shiau, A. Krivosheeva, V. Shaposhnikov, V. Borisenko, V. Gusakov, B. K. Tay, Electronic Properties of Bulk and Monolayer TMDs: Theoretical Study Within DFT Framework (GVJ-2e Method). *Physica Status Solidi (A) Applications and Materials Science* **214**, 1–7 (2017).
7. M. Bernardi, M. Palummo, J. C. Grossman, Extraordinary sunlight absorption and one nanometer thick photovoltaics using two-dimensional monolayer materials. *Nano Lett* **13**, 3664–3670 (2013).
8. L. Wang, J. B. Sambur, Efficient Ultrathin Liquid Junction Photovoltaics Based on Transition Metal Dichalcogenides. *Nano Lett* **19**, 2960–2967 (2019).

9. R. C. Evans, R. Austin, R. C. Miller, A. Preston, Z. N. Nilsson, K. Ma, J. B. Sambur, Surface-Facet-Dependent Electrochromic Properties of WO3Nanorod Thin Films: Implications for Smart Windows. *ACS Appl Nano Mater* **4**, 3750–3759 (2021).

10. R. C. Evans, A. Ellingworth, C. J. Cashen, C. R. Weinberger, J. B. Sambur, Influence of single-nanoparticle electrochromic dynamics on the durability and speed of smart windows. *Proceedings of the National Academy of Sciences*, doi: 10.1073/pnas.1822007116 (2019).

11. H. Shi, R. Yan, S. Bertolazzi, J. Brivio, B. Gao, A. Kis, D. Jena, H. G. Xing, L. Huang, Exciton dynamics in suspended monolayer and few-layer MoS2 2D crystals. *ACS Nano* **7**, 1072–1080 (2013).

12. D. Sun, Y. Rao, G. A. Reider, G. Chen, Y. You, L. Brézin, A. R. Harutyunyan, T. F. Heinz, Observation of rapid exciton-exciton annihilation in monolayer molybdenum disulfide. *Nano Lett* **14**, 5625–5629 (2014).

13. L. Wang, Z. Wang, H. Y. Wang, G. Grinblat, Y. L. Huang, D. Wang, X. H. Ye, X. Bin Li, Q. Bao, A. S. Wee, S. A. Maier, Q. D. Chen, M. L. Zhong, C. W. Qiu, H. B. Sun, Slow cooling and efficient extraction of C-exciton hot carriers in MoS2 monolayer. *Nat Commun* **8** (2017).

14. T. Borzda, C. Gadermaier, N. Vujicic, P. Topolovsek, M. Borovsak, T. Mertelj, D. Viola, C. Manzoni, E. A. A. Pogna, D. Brida, M. R. Antognazza, F. Scotognella, G. Lanzani, G. Cerullo, D. Mihailovic, Charge photogeneration in few-layer MoS2. *Adv Funct Mater* **25**, 3351–3358 (2015).

15. P. D. Cunningham, K. M. McCreary, A. T. Hanbicki, M. Currie, B. T. Jonker, L. M. Hayden, Charge Trapping and Exciton Dynamics in Large-Area CVD Grown MoS2. *Journal of Physical Chemistry C* **120**, 5819–5826 (2016).

16. S. H. Aleithan, M. Y. Livshits, S. Khadka, J. J. Rack, M. E. Kordesch, E. Stinaff, Broadband femtosecond transient absorption spectroscopy for a CVD Mo S2 monolayer. *Phys Rev B* **94** (2016).

17. C. Ruckebusch, M. Sliwa, P. Pernot, A. de Juan, R. Tauler, Comprehensive data analysis of femtosecond transient absorption spectra: A review. *Journal of Photochemistry and Photobiology C: Photochemistry Reviews* **13**, 1–27 (2012).

18. M. Bradler, P. Baum, E. Riedle, Femtosecond continuum generation in bulk laser host materials with sub-μJ pump pulses. *Appl Phys B* **97**, 561–574 (2009).

19. A. Brodeur, S. L. Chin, Ultrafast white-light continuum generation and self-focusing in transparent condensed media. *Journal of the Optical Society of America B* **16**, 637 (1999).

20. M. Kolesik, G. Katona, J. V. Moloney, E. M. Wright, Physical Factors Limiting the Spectral Extent and Band Gap Dependence of Supercontinuum Generation. *Phys Rev Lett* **91** (2003).

21. A. Šuminienė, V. Jukna, R. Šuminas, G. Tamošauskas, M. Vengris, A. Dubietis, Lisaf: An efficient and durable nonlinear material for supercontinuum generation in the ultraviolet. Lithuanian Physical Society [Preprint] (2020). https://doi.org/10.3952/physics.v60i4.4357.

22. R. Austin, Y. Farah, T. Sayer, B. M. Luther, A. Montoya-Castillo, A. Krummel, J. Sambur, Hot carrier extraction from 2D semiconductor photoelectrodes. (2022).

# Chapter 4 : HOT CARRIER EXTRACTION FROM 2D SEMICONDUCTOR PHOTOELECTRODES

The work presented in this chapter is a publication of the National Academy of Sciences in the journal Proceedings of the National Academy of Sciences from April 2023. Authors of the paper are Rachelle Austin, Yusef R. Farah, Brad M. Luther, Amber T. Krummel, and Justin B. Sambur from the department of Chemistry, Colorado State University, Fort Collins, CO, as well as Thomas Sayer and Andrés Montoya-Castillo from the Department of Chemistry, University of Colorado Boulder; Boulder, CO. Rachelle Austin, Yusef R. Farah, and Thomas Sayer are co-first authors. R.A., Y.R.F., T.S., B.M.L., A.M.-C., A.T.K., and J.B.S. designed research; R.A., Y.R.F., and T.S. performed research; R.A., Y.R.F., T.S., A.M.-C., A.T.K., and J.B.S. analyzed data; and R.A., Y.R.F., T.S., A.M.-C., A.T.K., and J.B.S. wrote the paper. This research was supported by the U.S. Department of Energy, Office of Science, Office of Basic Energy Sciences, under Award DE–SC0021189 and under Award DE-SC0016137.

## 4.1 Synopsis

Hot carrier-based energy conversion systems could double the efficiency of conventional solar energy technology or drive photochemical reactions that would not be possible using fully thermalized, “cool” carriers, but current strategies require expensive multi-junction architectures. Using an unprecedented combination of photoelectrochemical and in situ transient absorption spectroscopy measurements, we demonstrate ultrafast (<50 fs) hot exciton and free carrier extraction under applied bias in a proof-of-concept photoelectrochemical solar cell made from earth-abundant and potentially inexpensive monolayer (ML) $MoS_2$. Our approach facilitates ultrathin 7 Å charge transport distances over 1 $cm^2$ areas by intimately coupling ML-$MoS_2$ to an electron-selective solid contact and a hole-selective electrolyte contact. Our theoretical investigations of the spatial distribution of exciton states suggest greater electronic coupling

between hot exciton states located on peripheral S atoms and neighboring contacts likely facilitates ultrafast charge transfer. Our work delineates future 2D semiconductor design strategies for practical implementation in ultrathin photovoltaic and solar fuels applications.

## 4.2 Introduction

All semiconductors absorb photon energies greater than their bandgap, temporarily creating hot carriers with excess energy. In a conventional solar cell material like Si, 40% of the absorbed solar energy is lost as heat because hot carriers rapidly cool in <100 fs (1). This ultrafast hot-carrier cooling process prevents current solar cell technology from reaching theoretical efficiency limits (2).

A longstanding challenge in the field is to develop materials and selective charge-extraction contacts that efficiently collect hot carriers before they cool (3). The first experimental demonstration of hot-carrier extraction involved the transfer of photogenerated hot carriers from a bulk InP crystal to *p*-nitrobenzonitrile molecules in an electrochemical cell (4). Unfortunately, a significant fraction of hot-electrons thermalized in the InP bulk. Recent efforts in solid-state photovoltaics have focused on enhancing hot carrier populations in the semiconductor absorber and using charge energy-selective contacts to preferentially extract hot electron and hole populations (e.g., $In_{0.78}Ga_{0.22}As_{0.81}P_{0.19}$ quantum well surrounded by thick $In_{0.8}Ga_{0.2}As_{0.435}P_{0.565}$ barriers contacted by n- and p-doped InP contact layers (5)). Unfortunately, such multi-layer structures require expensive materials and growth methods, especially for the critical charge-selective contacts.

Nanostructured materials possess unique photophysical and structural properties that could make hot-carrier-based energy conversion systems both efficient and inexpensive, but this remains a formidable challenge (6). For example, while hot carrier extraction in graphene optoelectronics

is possible (7), graphene-based photovoltaics exhibit low quantum efficiency and small photovoltages (8, 9). Plasmonic metal nanostructure solar energy conversion systems suffer from low power conversion efficiency due to fast hot carrier cooling (10). While hot carrier extraction at model interfaces made of solution-processed organic–inorganic lead halide perovskite (11) and lead chalcogenide nanocrystals (12) has been demonstrated, electrical measurements of hot-carrier effects in a working solar energy conversion system are scant. Indeed, recent ultrafast X-ray measurements of lead halide perovskites highlight the need for concurrent electrical measurements because interpretation and quantification of hot electron and hole temperatures can be difficult using optical measurements alone (13).

In this work, we investigate the intriguing possibility of using inexpensive, earth-abundant, and potentially scalable (14) transition metal dichalcogenides (TMDs) such as monolayer (ML) $MoS_2$ for hot carrier extraction using a proof-of-concept photoelectrochemical solar cell. The bulk $MoS_2|I^-,I_3^-|Pt$ photoelectrochemical cell is a stable >14%-efficient solar cell (15) that is limited by a small 0.6 V photovoltage, which hot carrier collection could potentially circumvent. ML TMDs are exciting absorber materials because high energy photons generate hot excitons that are 0.98 eV above the optical band gap, often called C-excitons, with >100 ps lifetimes (16). These long and tunable (17) lifetimes exceed ultrafast photocurrent response in optoelectronic devices (18), which suggests hot carriers could be contributing to current in the device. Optical signatures of hot carrier transfer from $MoS_2$ to graphene (16) and gold (19) also suggest hot carrier transfer could outpace cooling, but electrical signatures of hot carrier transfer have remained elusive. Electrical measurements of solid-state ML TMD devices typically require edge-on contacts for charge extraction, meaning charge carriers travel micron-long distances to the charge-collecting interfaces. The long transport distances promote cooling and recombination, which likely explains

why hot carrier-induced currents have not been reported in any 2D TMD-based solar energy conversion device. The advantage of employing TMD absorbers in a photoelectrochemical cell is that photogenerated charge carriers need only travel across three atoms (0.7 nm) to reach the electron-selective indium tin oxide (ITO) substrate and hole-collecting redox electrolyte (Fig. 1a). The long lifetime of C-excitons combined with short charge-transfer distances and intimate charge carrier-selective contacts thus raises the exciting possibility of extracting hot carriers in the model ML-$MoS_2$|$I^-$,$I_3^-$|Pt solar cell.

Using an unprecedented combination of photoelectrochemical and in situ time-resolved spectroscopic techniques, here we show hot carrier extraction outcompetes exciton formation and relaxation in a working photoelectrochemical cell. We demonstrate that hot carriers can be extracted to generate photocurrent before cooling to the band-edge and develop a picture of the photocurrent generation mechanism in ML-$MoS_2$ photoelectrodes.

### 4.3 Results and Discussion

*Optical and Photoelectrochemical Characterization of the ML-$MoS_2$ photoelectrode.*

Here we test our hypothesis that one should be able to preferentially extract hot carriers from the C-exciton manifold in ML-$MoS_2$ using the electron- and hole-selective contacts in a photoelectrochemical cell because the three atom-thick transport distance minimizes the electron and hole transport times relative to the cooling times. Photoluminescence and Raman spectroscopy confirmed the chemical vapor deposition (CVD) growth method produced ML-$MoS_2$ (see Chapter 3). To probe the hot-carrier generation, recombination, and extraction processes, we constructed a transparent photoelectrochemical cell that enables in situ ultrafast spectroscopy measurements to measure relative exciton populations after photo-excitation (Fig. 4-1a). The ML-$MoS_2$-coated ITO electrode serves as the working electrode in a three-electrode microfluidic electrochemical cell

containing 1 M NaI electrolyte. Fig. 4-1a schematically shows that under illumination and applied positive potentials, photogenerated holes move to the semiconductor/liquid interface and oxidize $I^-$ to $I_2$ while photogenerated electrons transfer to the ITO substrate, generating net anodic current flow through the cell.

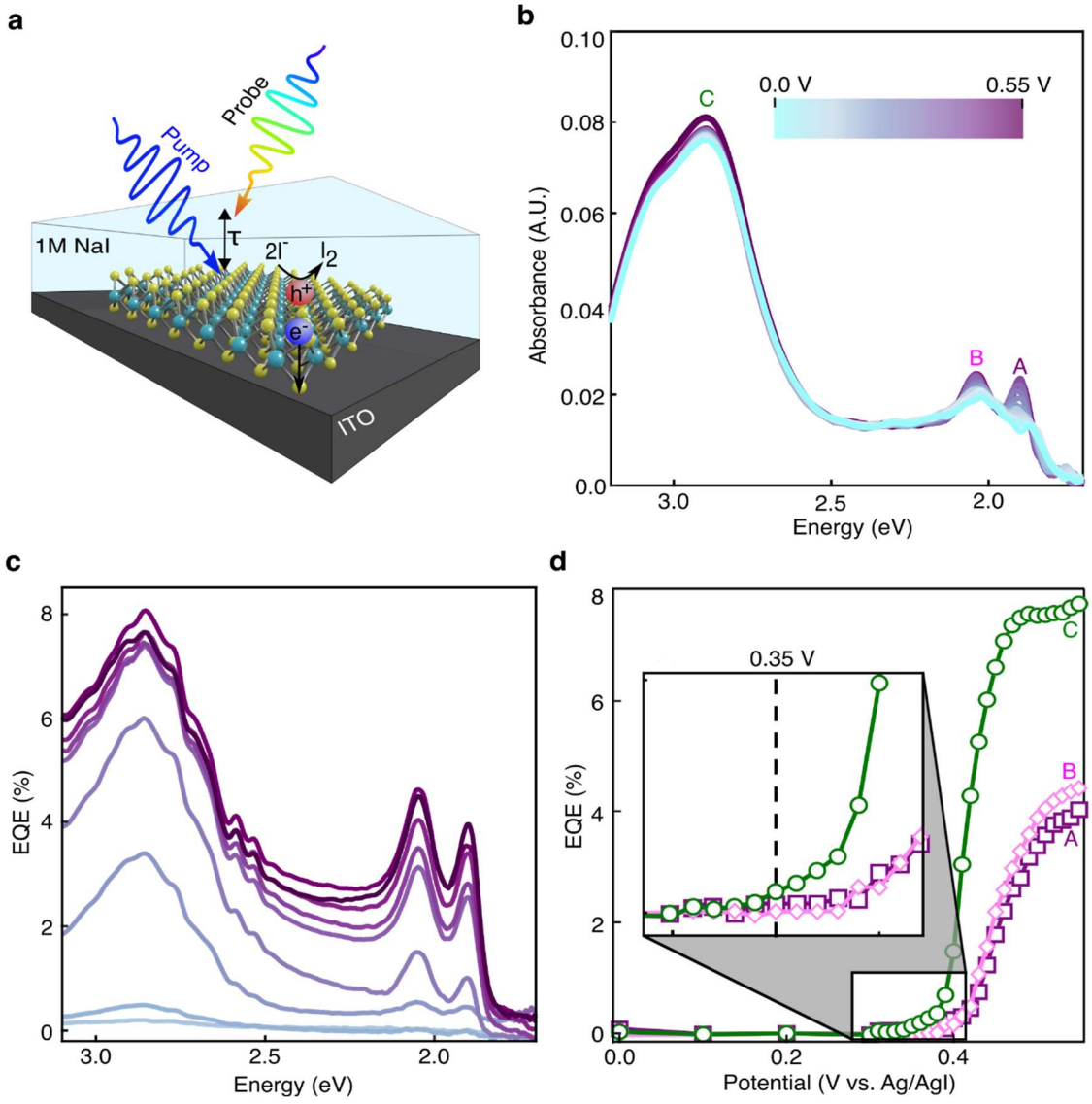


Figure 4-1. Optoelectronic properties of the monolayer $MoS_2$ photoelectrochemical cell. (a) Cartoon illustration of the three-electrode photoelectrochemical cell. The solid blue and rainbow arrows indicate pump and probe pulses for TA measurements. Pt counter and Ag/AgI reference electrodes are omitted for clarity. (b) Absorbance spectra in 0.025 V increments from 0.0 V to 0.55

V. (c) EQE spectra versus applied potential from 0.35 V to 0.55 V. EQE($\boldsymbol{\lambda}$)=qi/$I_0$($\boldsymbol{\lambda}$), where q is the electronic charge (in units of C), i is the photocurrent (in units of A), and $I_0$ is the monochromatic light power (in units of $s^{-1}$). **(d)** Monochromatic i-E measurements for resonant A-, B-, and C-exciton excitation (i.e., 650 nm, 605 nm, and 405 nm, respectively).

To assess which excitonic transitions contribute to current flow in the ML-$MoS_2$ photoelectrode, we simultaneously measured optical absorbance and photocurrent signals under working photoelectrochemical conditions. Fig. 4-1b shows absorbance spectra of ML-$MoS_2$ as a function of the applied potential, referenced to the Ag/AgI electrode. All spectra feature three peaks corresponding to the band-edge A (1.99 eV) and B (2.01 eV) excitons, and the higher energy C-exciton (2.98 eV). The A and B-exciton peak intensities increase and blue shift with increasing positive potential, in agreement with literature, while the high energy C-exciton increases slightly with positive bias and does not shift with potential. The origin of this potential-dependent absorption behavior can be explained as follows. Two distinct optical transitions contribute to the absorption feature in the A-exciton region. The neutral A-exciton absorbance dominates at positive potentials. At more negative potentials, the negatively charged trion absorbs strongly, resulting in a shoulder feature at 670 nm. The A-exciton absorption feature increases in intensity and narrows in width as the potential moves from negative to positive values because oscillator strength transfers from the trion to the neutral exciton (20). The shifting and intensity change of the A-exciton is discussed in more detail in Chapter 5. The observed potential-dependent absorbance changes (Fig. 4-1b) have important consequences for interpreting the relative populations of excitons gleaned from ultrafast TA measurements, as will be discussed below.

Photocurrent measurements performed concurrently with the absorbance measurements revealed at which potentials the different excitons dissociate and contribute to current flow in the cell. Figure 1c shows potential dependent external quantum efficiency (EQE) spectra, where $EQE = i/qI_0$ and $i$ is the photocurrent, $q$ is the elementary charge, and $I_0$ is the light power. At positive

bias (e.g., $E > 0.5$ V), the EQE spectrum mimics the absorbance spectrum (solid purple line in Fig. 4-1c), indicating the applied potential generates a sufficiently strong interfacial electric field to effectively dissociate all three excitonic species. Close examination of the potential-dependent spectra reveals subtle differences between the photocurrent onset potential ($E_{on}$) for the A, B, and C-excitons that are further distinguished in monochromatic current-voltage curve measurements (Fig. 4-1d). Interestingly, photocurrent generation onsets first (i.e., less positive potentials) for the C-exciton and the slope of the C-exciton current-voltage curve is significantly steeper than that of the A/B-excitons. The photovoltage, defined as $E_{on}$ - $E^{0'}(I^-,I_2)$, where $E^{0'}(I^-,I_2)$ is the formal potential of the iodide/iodine couple (0.63 V vs Ag/AgI), is largest for C-exciton illumination. The lower $E_{on}$ value means that, under conditions of equivalent interfacial electric field strength, photo-excited C-excitons require less driving force to dissociate and contribute to current flow in the cell compared to the lower energy A/B-excitons (23). Since we did not observe photocurrent upon directly exciting the A/B-excitons at the same applied potential as that of the C-exciton (specifically $E$ = 0.35 V in Fig. 4-1d), our monochromatic current-voltage data strongly suggests that C-excitons are extracted before they cool to the band edge and form low energy A/B-excitons.

*Nature of excitonic states and their implication for charge transfer*

Why is C-exciton extraction more efficient than low energy A/B-exciton extraction in a ML-$MoS_2$ photoelectrode? To shed light on this critical question, we turned to a theoretical treatment of the spatial distribution of the A/B- versus C-excitons in ML-$MoS_2$. The goal of this theoretical investigation is to qualitatively compare the magnitude of electronic coupling between the different exciton states in the charge donor ($MoS_2$) and the electron/hole acceptors (ITO

substrate/iodide anions), which ultimately allows us to rationalize why charge transfer from the C-exciton is more efficient than A/B-excitons.

We first analyzed the excitonic wavefunctions obtained by solving the Bethe-Salpeter equation (BSE) for unsupported ML-$MoS_2$ in vacuum (see Methods). This approach accounts for excitonic effects by explicitly treating electron-hole correlation. Figure 4-2-center shows the resulting eigen spectrum of pristine ML-$MoS_2$, where the bound eigenstates arising from a BSE calculation are linear combinations of independent-particle states at different points in quasi-momentum (k-) space. The purple lines are the lowest energy excitonic states around the K point. The lowest energy transition is the A-exciton ($E_{\mathrm{ex}}^{A}$) and optical bandgap of $MoS_2$ while the higher energy states are the A-exciton 'hydrogenic series, consistent with literature (24, 25). The green lines represent the levels in the band nesting region between K and Γ, where the lowest energy

transition is the C-exciton $E_{\mathrm{ex}}^{C}$. The B-exciton states do not appear in Fig. 2-center because our calculations do not include spin-orbit coupling effects.

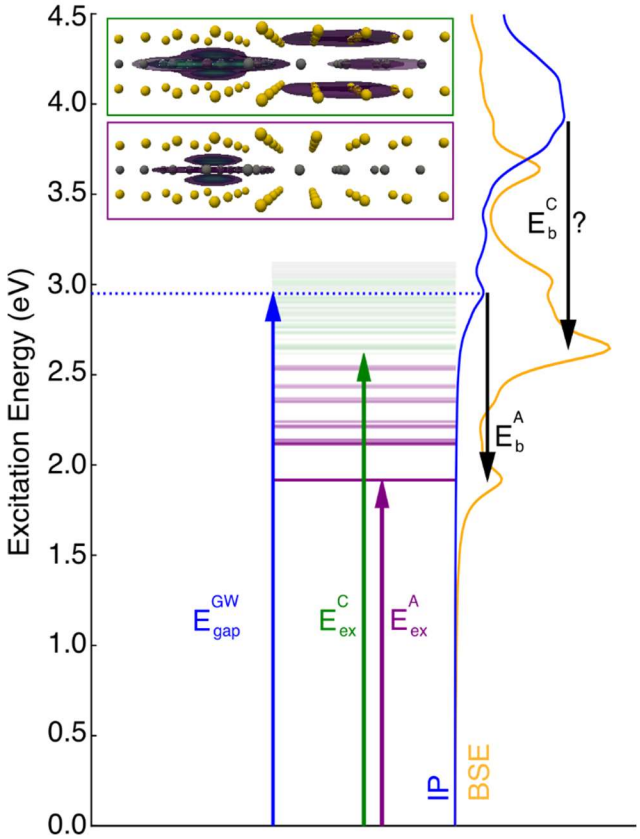


Figure 4-2. Center: Eigen spectrum of unsupported ML-$MoS_2$ in vacuum calculated from BSE. The purple and green lines represent the A-exciton `hydrogenic series' around the K point and the C-exciton states in the band nesting region between K and $\Gamma$, respectively. The transparency of each energy level is set to the oscillator strength of the transition, normalized by the A-1s transition (labeled $E_{ex}^{A}$), which is the strongest. $E_{ex}^{C}$ is the energy of the first C-exciton state. The dotted blue line represents the fundamental electronic band gap at 2.9 eV, which is at the K point. C-excitons and free-carriers at this energy (co)exist in different regions of k-space. Top: The hole-averaged isosurface plots for the electron density in the aforementioned A-exciton (below, purple box) and C-exciton (above, green box) states. Right: The absorption spectra as calculated for the BSE states pictured (orange) and the underlying single particle states (blue). The energy difference between peaks represents the A- and C-exciton binding energies ($E_b^A$ and $E_b^C$).

We now consider the comparative ease of extracting electrons from the photo-excited C-exciton in contrast to A/B-excitons from a classic Marcus-type charge transfer (26, 27) pathway comparing the relative magnitude of the electronic coupling associated with electron (hole) transfer from the C- vs A/B-excitons in $MoS_2$ to ITO (iodide). Marcus-type arguments have been previously employed to analyze charge transfer characteristics between TMDs and quantum dots or molecular species (28). When the rate of electron (hole) transfer to the ITO substrate (iodide) is in the small electronic coupling regime, then the rate of charge transfer is proportional to $|V|^2$, the absolute value of the electronic coupling that connects the donor and acceptor states. The A- and C-excitons, formed from states in different regions of the band structure, have different spatial distributions within the $MoS_2$ layer. Figure 4-2-top illustrates that A-excitons are localized on interior Mo atoms whereas C-excitons have significant electron density on the peripheral S atoms, consistent with the atomic orbital composition of these k-space regions in previous DFT calculations (29–31). Since $V$ decays exponentially with the distance between the donor and acceptor, one would expect that the C-excitons' closer approach to the ITO/aqueous interfaces results in a faster charge transfer rate. To make this a quantitative Marcus-type analysis, one would additionally require the construction of charge localized states, the calculation of their energies and couplings, the calculation of exciton/charge phonon coupling, and its modulation by the disorder of the solution. Methods for these calculations are still under development (32–36). Nevertheless, our results and calculations provide unique insight into the origin of distinct photocurrent efficiencies for the A/B- and C-excitons in a ML-$MoS_2$ photoelectrode. Furthermore, since the hole density of the C-exciton is localized on the interior Mo atoms and less electronically

coupled to the iodide acceptors, one might hypothesize that the redox mechanism is a sequential one of electron transfer to ITO preceding hole transfer to the iodide acceptor in solution.

We now turn to ultrafast optical measurements to probe the mechanism of photocurrent generation in greater detail.

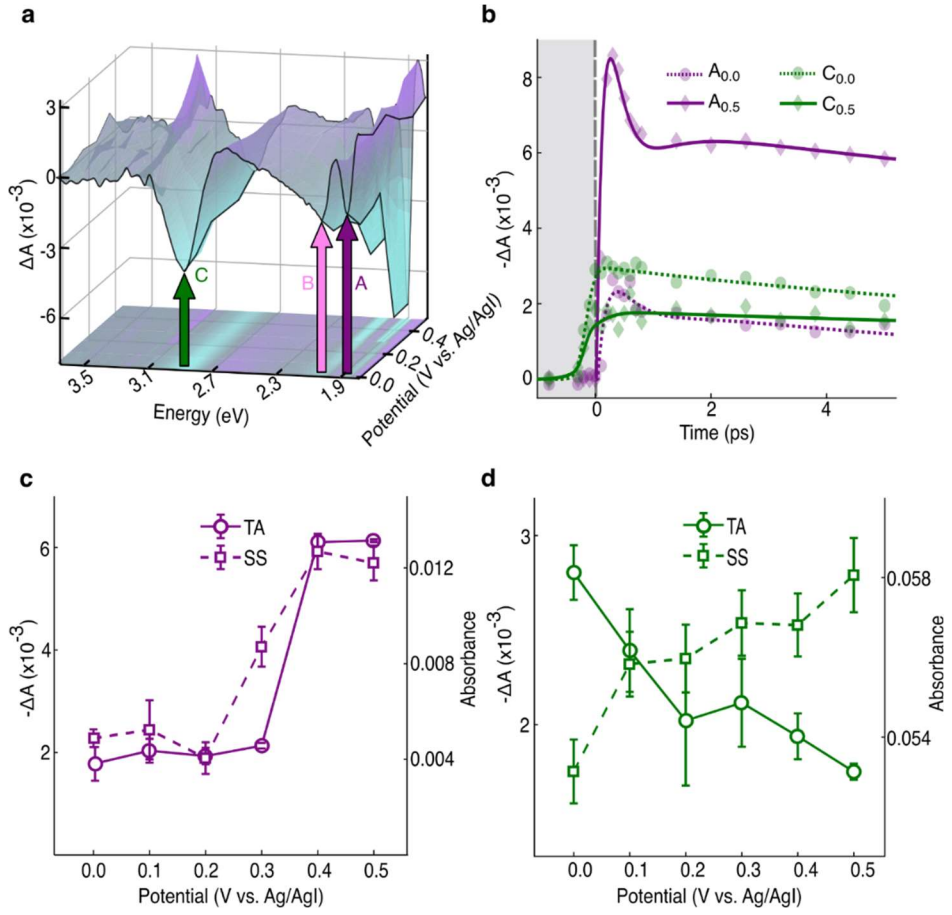


Figure 4-3. Transient absorption of monolayer $MoS_2$ photoelectrochemical cell. (a) Potential-dependent TA spectra at $\tau$ = 1 ps. (b) Temporal trace of the A-exciton (purple) and C-exciton (green) bleach intensity for 0.0 V (filled circles) and 0.5 V (filled diamonds). Solid and dashed lines are fits to Eq. 3-3 and 3-4 in Chapter 3. The –ΔA values were determined using a Gaussian peak fitting procedure to obtain the maximum bleach signal regardless of peak shifts induced by unavoidable BGR effects. (c-d) Steady-state absorbance (squares) and TA bleach intensity at $\tau$ = 1 ps (circles) for the (c) A- and (d) C-excitons.

*Exciton Population Dynamics via Ultrafast Transient Absorption Spectroscopy*

We leveraged ultrafast pump-probe transient absorption (TA) spectroscopy to assess the feasibility and elucidate the mechanism of hot carrier extraction in ML-$MoS_2$ photoelectrodes. In situ TA spectroscopy allowed us to measure relative changes in exciton populations under working photoelectrochemical conditions. In this experiment, we employ a <50 fs, 3.1 eV pump pulse corresponding to the high energy side of the C-exciton to generate a distribution of excited states, including hot free carriers in continuum states of ML-$MoS_2$. Experiments were performed with a pump fluence of 75 μJ/cm$^2$, where the exciton bleach intensities are linear with pump fluence (see Chapter 3), in agreement with literature (16). A white light continuum probe pulse spanning 3.1 eV - 1.65 eV was used to measure the absorbance changes of the sample as a function of pump-probe delay time ($\tau$) (see Chapter 3). A potential-dependent anodic current flows through the cell upon photoexcitation of the sample with the pump pulse (Chapter 3), further confirming that the TA experiment reports on exciton populations under working photoelectrochemical conditions. Figure 4-3a shows TA spectra at $\tau$ = 1 ps as a function of applied potential. The $\tau$ = 1 ps condition yields spectra whose excitonic features are not dominated by the influence of hot electrons or free carriers and, therefore, this delay time provides a clear picture of the relative changes in exciton population versus applied potential (37). The TA signal is given by $\Delta A(\tau) = A_{\mathrm{pump}}(\tau) - A_{\mathrm{unpumped}}$, where $A_{\mathrm{pump}}(\tau)$ and $A_{\mathrm{unpumped}}$ represent the absorbance values of the pumped and unpumped samples, respectively. Figure 4-3a shows bleach features (negative $\Delta A(\tau)$) at the exciton peak energies due to exciton formation. The fact that we observe bleach signals from all exciton states indicates that free electrons and holes in unbound states relax into A, B, and C-exciton populations, in agreement with literature (38). However, C-excitons do not decay into A/B-exciton states, as will be discussed in further detail below. Unlike bulk semiconductors, $A_{\mathrm{unpumped}}$

(the steady state absorbance) changes significantly with applied potential (Fig. 4-1b) for ML-$MoS_2$ and must be considered when interpreting relative exciton populations from in situ TA data.

Before discussing changes in the relative exciton populations, we first examine the exciton formation and depletion processes in the ML-$MoS_2$ photoelectrode. Figure 4-3b shows A and C-exciton TA decay dynamics at 0.5 V and 0.0 V, corresponding to conditions of significant anodic photocurrent and no photocurrent, respectively. The B-exciton behavior closely follows that of the A-exciton (see Chapter 3) and is omitted from Fig. 4-3b for visual clarity. The temporal behavior of the C-exciton and the band edge A/B-excitons display three key differences (see Fig. 4-3b). First, the C-exciton bleach intensity reaches a maximum value almost instantaneously (i.e., $\tau = 0$ ps), indicating C-excitons form on a faster timescale than our instrument response (<50 fs), which aligns with previous work (38) and is expected since the pump pulse is tuned to the high energy side of the C-exciton spectrum. The C-exciton bleach signal increases at –400 fs because in our transient absorption experiments, the pump pulse and probe pulse overlap at the sample to produce the third order signal. The instrument response function of this pump-probe overlap is approximately 100 fs full-width-half-maximum (see Chapter 3). The pump energy is also nearly resonant with the C-exciton, which is why the early rise time occurs for the C-excitons and not the A-excitons. The A-exciton bleach reaches a maximum value at longer times ($\tau = 200$ fs). During this time, we observe no decay of the C-exciton bleach, *indicating that C-excitons do not cool to A-excitons on the 200 fs timescale*; if C-excitons decayed to A-excitons over this timescale, we would expect to observe a fast C-exciton decay component commensurate with the A-exciton rise time, but no such decay is observed. We observed that the A/B-exciton bleach signals decay *slower* under conditions of charge extraction (Chapter 3), suggesting that photo-excited C-excitons do not cool to form band edge A/B-excitons that then dissociate and inject into the ITO electrode. Instead,

after C-exciton formation, the fast component for C-exciton decay occurs within the first tens of picoseconds, consistent with intervalley relaxation mechanisms (16, 17). Third, the C-exciton bleach magnitude at $\tau$ = 0 ps is greater (i.e., more negative) at 0.0 V than +0.5 V, but the opposite trend occurs for the A-exciton. This third observation is critical for interpreting how the exciton populations change as a function of applied potential and will be discussed below.

We now exploit steady-state absorbance and ultrafast TA measurements to disentangle the relative exciton population changes. Recalling the TA signal, $\Delta A(\tau) = A_{\mathrm{pump}}(\tau) - A_{\mathrm{unpumped}}$, and recognizing that steady-state absorbance measurements represent $A_{\mathrm{unpumped}}$, we extract relative changes in the exciton populations from $A_{\mathrm{pumped}}$, where a larger magnitude indicates more exciton population. Figure 3c-d compares steady-state absorbance and TA bleach intensities of the A- and C-excitons as a function of applied potential. For the A-exciton (Fig. 4-3c), the TA and steady-state data closely follow one another, suggesting that the increase in $\Delta A(\tau)$ can be attributed to $A_{\mathrm{unpumped}}$ instead of $A_{\mathrm{pumped}}$. In contrast to the A-exciton, $A_{\mathrm{unpumped}}$ for the C-exciton slightly increases with positive bias (Fig. 4-1b), but $\Delta A(\tau)$ significantly decreases for the

C-exciton (Fig. 4-3d), suggesting that fewer C-excitons contribute to the TA signal under these conditions.

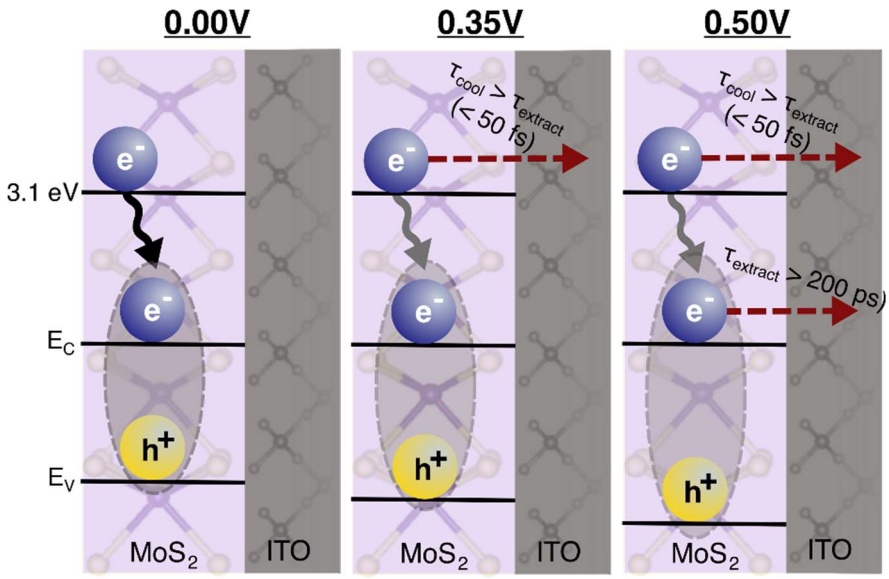


Figure 4-4. Scheme of hot carrier extraction process in the ML-$MoS_2$ photoelectrochemical cell.

Two scenarios could explain why C-excitons contribute less to the TA signal with positive bias. First, bound C-excitons may dissociate, producing photocurrent in the external circuit via the Marcus-type scheme introduced above. This scenario requires that photocurrent generation occurs faster than TA signal generation. The second possibility is that a portion of the hot, free electrons (charge carriers that have not cooled to the band edge A/B-exciton states) created by the pump pulse in the continuum levels of the conduction band do not cool to form C-excitons. Instead, *the hot electrons inject directly into the ITO electrode before C-exciton formation and generate photocurrent.* Figure 4-4 schematically shows the hot carrier process in the ML-$MoS_2$ photoelectrochemical cell. Exciting ML-$MoS_2$ with 3.1 eV light generates hot free carriers in continuum states. This photon energy also generates C-excitons. Under 0.00 V bias, photo-excited

free carriers cool to A/B/C-excitons. No carrier extraction occurs. Under 0.35 V bias, ultrafast carrier extraction occurs from only the high-energy free carriers/C-exciton populations. Under 0.50 V bias, ultrafast extraction from the high-energy free carriers/C-exciton population occurs in addition to some extraction from the band-edge A/B-exciton states, likely at longer times. On the ultrafast timescales of our transient absorption experiments, we observe extraction of free carriers before C-exciton formation occurs and C-excitons do not cool to the band-edge states. These are hot carrier extraction processes because the free carriers/C-excitons transfer to the ITO substrate before they cool to the band-edge. This mechanism of hot electron injection offers exciting opportunities to achieve solar energy conversion efficiencies beyond the detailed balance limit.

Theoretically, the latter mechanism of hot electron injection into the ITO is compatible with a scenario where bound C-excitons and continuum unbound carriers interconvert through isoenergetic scattering processes. Our calculations indicate that the binding energy of C-excitons is on the order of that of the A-exciton, making them degenerate with unbound continuum states elsewhere in the Brillouin zone, an observation consistent with previous calculations (40, 41). Since these bound and unbound species are degenerate, one may imagine highly efficient intra- and inter-band scattering, known to occur on timescales of tens to hundreds of femtoseconds (42), that would establish a dynamic equilibrium between C-excitons and free carriers. These unbound species could then be extracted as hot carriers by a moderate applied field or subsequently relax to the band-edge, where they would only contribute to the current at sufficiently high applied fields. In contrast, A-excitons (and their hydrogenic series) are necessarily mid-gap, and so cannot be degenerate with unbound carriers. This means that to extract an electron or hole from these species, one will always incur the additional cost of overcoming their binding energy, presumably

explaining the additional driving force (more positive potential) required for A/B-exciton photocurrent generation in Fig. 4-1d-inset.

While our theoretical treatment is presently useful in delineating the possibilities of how hot carrier extraction can occur in ML-$MoS_2$, we emphasize that these calculations are only valid for unsupported $MoS_2$ in vacuum. Indeed, it is challenging to treat the full system accurately within the BSE, since one must include the role of the ITO substrate and electrolyte screening, the finite carrier population (as a function of potential), phonon coupling, and excitonic band-dispersion (in the nesting region in particular) into an already costly computation. The aforementioned factors are in fact major areas of current research (20, 45, 46) and the results presented in this paper strongly motivate their continued study. Beyond the fundamental challenge of an affordable, unified electronic structure of this material, a full theoretical treatment will need to address the statistical, electrochemical aspects of the device, meaning this is only the first step in the construction of a predictive multiscale model of photoelectrochemical activity in ultrathin TMDs.

**4.4 Conclusions**

Steady state and ultrafast spectroelectrochemical experiments support an ultrafast, hot carrier extraction mechanism in a ML-$MoS_2$ photoelectrochemical cell. We employed theoretical treatments to construct a photophysical model of photocurrent generation and hot carrier extraction. In our working model, the extraction of hot carriers following high energy photo-excitation can be accomplished before the formation of excitonic species, leading to the high photocurrent yields in our proof of concept photoelectrochemical solar cell architecture. Calculation of excitonic states suggested two possible mechanisms: one arising from a classic Marcus picture of charge transfer that implies that the delocalized orbital composition for high energy C-excitons may facilitate efficient and ultrafast carrier extraction within the

photoelectrochemical cell, and the other invoking a rapid equilibrium between bound C-excitons and isoenergetic free carriers that can be extracted more easily than their bound counterparts. Importantly, our experimental results present a grand challenge to existing theory and motivate the continued improvement of many-body theories in 2D materials and their heterostructures.

The mechanisms we suggest delineate the development of 2D semiconductors for practical implementation in ultrathin photovoltaic and solar fuels applications. A lightweight ML 2D semiconductor photovoltaic device can achieve 70 kW/kg of specific power (47). Hot carrier effects could improve the cell photovoltage if suitable energy-selective contacts could be interfaced with the 2D semiconductor such that the hot electron and hole populations could be maintained in the external circuit after the ultrafast charge extraction process (5,48). Our work also highlights opportunities to develop large-area solid-state systems that intimately couple the ultrathin semiconductor to energy-selective contacts without short-circuiting the device. Engineering novel 2D semiconductor/substrate architectures could also maximize light absorption in these thin semiconductors (49). For photocatalysis and solar fuels research, we envision Janus-type 2D semiconductor absorbers where a reductive co-catalyst for $H_2$ production or $CO_2$ reduction is attached to one layer of S atoms and an oxidative co-catalyst is positioned on the opposing S layer; the redox potentials of the co-catalysts can be tuned relative to the excited state electron and hole levels in the 2D semiconductor. There are rich opportunities to study how the energy level alignment between redox species in the liquid electrolyte and hot electron/hole states of ML-$MoS_2$ affect hot carrier extraction rates and yields.

**References**


1. A. J. Nozik, Spectroscopy and hot electron relaxation dynamics in semiconductor quantum wells and quantum dots. *Annu. Rev. Phys. Chem.* **52**, 193-231 (2001).
2. W. Shockley, H. J. Queisser, Detailed balance limit of efficiency of p-n junction solar cells. *J Appl Phys* **32**, 510–519 (1961).
3. A. J. Nozik, Utilizing hot electrons. *Nat Energy* **3**, 170–171 (2018).
4. G. Cooper, J. A. Turner, B. A. Parkinson, A. J. Nozik, Hot carrier injection of photogenerated electrons at indium phosphide-electrolyte interfaces. *J Appl Phys* **54**, 6463–6473 (1983).
5. D. T. Nguyen, *et al.*, Quantitative experimental assessment of hot carrier-enhanced solar cells at room temperature. *Nat Energy* **3**, 236–242 (2018).
6. A. J. Nozik, Quantization effects in semiconductor nanostructures and singlet fission in molecular chromophores for photovoltaics and solar fuels. *Chem. Phys. Rev* **2**, 21305 (2021).
7. N. M. Gabor, *et al.*, Hot Carrier–Assisted Intrinsic Photoresponse in Graphene. *Science (1979)* **334**, 648–652 (2011).
8. D. Sun, *et al.*, Ultrafast hot-carrier-dominated photocurrent in graphene. *Nat Nanotechnol* **7**, 15 (2012).
9. X. Xu, N. M. Gabor, J. S. Alden, A. M. van der Zande, P. L. Mceuen, Photo-Thermoelectric Effect at a Graphene Interface Junction *Nano Lett.* **10**, 562–566 (2010).
10. Y. Zhang, C. Yam, G. C. Schatz, Fundamental Limitations to Plasmonic Hot-Carrier Solar Cells. *J. Phys. Chem. Lett* **7**, 43 (2016).
11. M. Li, *et al.*, Slow cooling and highly efficient extraction of hot carriers in colloidal perovskite nanocrystals. *Nat Commun* **8**, 3–12 (2017).

12. W. A. Tisdale, *et al.*, Hot-Electron Transfer from Semiconductor Nanocrystals. *Science (1979)* **328**, 1543–1547 (2010).

13. M. Verkamp, *et al.*, Carrier-Specific Hot Phonon Bottleneck in CH3NH3PbI3 Revealed by Femtosecond XUV Absorption. *J. Am. Chem. Soc* **143**, 30 (2021).

14. C. Wadia, A. P. Alivisatos, D. M. Kammen, Materials Availability Expands the Opportunity for Large-Scale Photovoltaics Deployment. *Environ. Sci. Technol.* **43**, 2072–2077 (2009).

15. G. Kline, K. Kam, D. Canfield, B. A. Parkinson, Efficient and stable photoelectrochemical cells constructed with WSe2 and MoSe2 photoanodes. *Sol. Energy Mater.* **4**, 301-308 (1981).

16. L. Wang, *et al.*, Slow cooling and efficient extraction of C-exciton hot carriers in MoS2 monolayer. *Nat Commun* **8** (2017).

17. A. H. Rose, T. J. Aubry, H. Zhang, D. Vigil-Fowler, J. van de Lagemaat, Ultrastrong Coupling Leads to Slowed Cooling of Hot Excitons in Few-Layer Transition-Metal Dichalcogenides. *J. Phys. Chem. C*, **126**, 8710–8719 (2022).

18. K. T. Vogt, S. F. Shi, F. Wang, M. W. Graham, Ultrafast Photocurrent and Absorption Microscopy of Few-Layer Transition Metal Dichalcogenide Devices That Isolate Rate-Limiting Dynamics Driving Fast and Efficient Photoresponse. *J. Phys. Chem. C* **124**, 15195–15204 (2020).

19. A. Grubišić Čabo, *et al.*, Observation of Ultrafast Free Carrier Dynamics in Single Layer MoS2. *Nano Lett* **15**, 5883–5887 (2015).

20. Y. W. Chang, D. R. Reichman, Many-body theory of optical absorption in doped two-dimensional semiconductors. *Phys Rev B* **99** (2019).

21. G. M. Carroll, H. Zhang, J. R. Dunklin, E. M. Miller, N. R. Neale, Unique interfacial thermodynamics of few-layer 2D MoS 2 for (photo) electrochemical catalysis. *Energy Environ. Sci.* **12**, 1648–1656(2019).

22. E. J. Sie, *et al.*, Observation of Exciton Redshift-Blueshift Crossover in Monolayer WS2. *Nano Lett* **17**, 4210–4216 (2017).

23. A. R. Klots, *et al.*, Probing excitonic states in suspended two-dimensional semiconductors by photocurrent spectroscopy. *Sci Rep* **4** (2014).

24. D. Y. Qiu, F. H. da Jornada, S. G. Louie, Optical spectrum of MoS2: Many-body effects and diversity of exciton states. *Phys Rev Lett* **111** (2013).

25. A. Molina-Sánchez, D. Sangalli, K. Hummer, A. Marini, L. Wirtz, Effect of spin-orbit interaction on the optical spectra of single-layer, double-layer, and bulk MoS2. *Phys Rev B Condens Matter Mater Phys* **88** (2013).

26. R. A. Marcus, Electron transfer reactions in chemistry. Theory and experiment. *Rev. Mod. Phys.* **65**, 599 (1993).

27. C. E. D. Chidsey, Free Energy and Temperature Dependence of Electron Transfer at the Metal-Electrolyte Interface. *Science* **251**, 919–922 (1991).

28. D. B. Sulas-Kern, E. M. Miller, J. L. Blackburn, Photoinduced charge transfer in transition metal dichalcogenide heterojunctions-towards next generation energy technologies. *Energy Environ Sci* **13**, 2684–2740 (2020).

29. S. Fang, *et al.*, Ab initio tight-binding Hamiltonian for transition metal dichalcogenides. *Phys Rev B Condens Matter Mater Phys* **92** (2015).

30. E. S. Kadantsev, P. Hawrylak, Electronic structure of a single MoS2 monolayer. *Solid State Commun* **152**, 909–913 (2012).

31. A. Kormányos, *et al.*, Erratum: K.p theory for two-dimensional transition metal dichalcogenide semiconductors. *2D Mater* **2** (2015).

32. A. Migliore, A. Nitzan, On the evaluation of the Marcus-Hush-Chidsey integral. *Journal of Electroanalytical Chemistry* **671**, 99–101 (2012).

33. S. Ghosh, A. v. Soudackov, S. Hammes-Schiffer, Electrochemical Electron Transfer and Proton-Coupled Electron Transfer: Effects of Double Layer and Ionic Environment on Solvent Reorganization Energies. *J Chem Theory Comput* **12**, 2917–2925 (2016).

34. F. Giustino, Electron-phonon interactions from first principles. *Rev Mod Phys* **89** (2017).

35. J. J. Zhou, *et al.*, Ab Initio Electron-Phonon Interactions in Correlated Electron Systems. *Phys Rev Lett* **127** (2021).

36. H. Y. Chen, D. Sangalli, M. Bernardi, Exciton-Phonon Interaction and Relaxation Times from First Principles. *Phys Rev Lett* **125** (2020).

37. P. D. Cunningham, A. T. Hanbicki, K. M. McCreary, B. T. Jonker, Photoinduced Bandgap Renormalization and Exciton Binding Energy Reduction in WS2. *ACS Nano* **11**, 12601–12608 (2017).

38. C. Trovatello, *et al.*, The ultrafast onset of exciton formation in 2D semiconductors. *Nat Commun* **11** (2020).

39. E. A. A. Pogna, *et al.*, Photo-induced bandgap renormalization governs the ultrafast response of single-layer MoS2. *ACS Nano* **10**, 1182–1188 (2016).

40. S. H. Aleithan, *et al.*, Broadband femtosecond transient absorption spectroscopy for a CVD Mo S2 monolayer. *Phys Rev B* **94** (2016).

41. A. R. Klots, *et al.*, Probing excitonic states in suspended two-dimensional semiconductors by photocurrent spectroscopy. *Sci Rep* **4** (2014).

42. L. Gao, Z. Hu, J. Lu, H. Liu, Z. Ni, Defect-related dynamics of photoexcited carriers in 2D transition metal dichalcogenides. *Physical Chemistry Chemical Physics* **23**, 8222–8235 (2021).

43. D. K. Efimkin, E. K. Laird, J. Levinsen, M. M. Parish, A. H. Macdonald, Electron-exciton interactions in the exciton-polaron problem. *Phys Rev B* **103** (2021).

44. S. S. Ataei, A. Sadeghi, Competitive screening and band gap renormalization in -type monolayer transition metal dichalcogenides. *Phys Rev B* **104** (2021).

45. Y. Cho, S. J. Bintrim, T. C. Berkelbach, Simplified GW/BSE Approach for Charged and Neutral Excitation Energies of Large Molecules and Nanomaterials. *Cite This: J. Chem. Theory Comput* **18**, 3446 (2022).

46. G. Antonius, S. G. Louie, Theory of exciton-phonon coupling. *Phys Rev B* **105**, 85111 (2022).

47. K. M. Islam, T. Ismael, C. Luthy, O. Kizilkaya, M. D. Escarra, Large-Area, High-Specific-Power Schottky-Junction Photovoltaics from CVD-Grown Monolayer MoS 2. *Cite This: ACS Appl. Mater. Interfaces* **14**, 24281–24289 (2022).

48. Y. Wang, *et al.*, P-type electrical contacts for 2D transition-metal dichalcogenides. *Nature* **610**, 61 (2022).

49. M. A. Green, "Third Generation Photovoltaics Advanced Solar Energy Conversion" (2003).

50. L. Wang, J. B. Sambur, Efficient Ultrathin Liquid Junction Photovoltaics Based on Transition Metal Dichalcogenides. *Nano Lett* **19**, 2960–2967 (2019).

# Chapter 5 : HIDING IN PLAIN SIGHT - THE PRESENCE OF ROOM-TEMPERATURE TRIONS IN NONLINEAR OPTICAL EXPERIMENTS OF 2D MATERIALS[2]

The work presented in this chapter is an invited perspective article publication of the American Institute of Physics in the Journal of Chemical Physics that will be submitted in May 2024. Authors of the paper are Rachelle Austin, Amber T. Krummel, Justin B. Sambur, and Yusef R. Farah from the department of Chemistry, Colorado State University, Fort Collins, CO, as well as Thomas Sayer and Andrés Montoya-Castillo from the Department of Chemistry, University of Colorado Boulder, Boulder, CO. R.A., Y.R.F., T.S., A.M.-C., A.T.K., and J.B.S. designed research; R.A., Y.R.F., and T.S. performed research; R.A. analyzed data; R.A. and J.B.S. wrote the paper; and R.A., Y.R.F., T.S., A.M.-C., A.T.K., and J.B.S. edited the paper.

## 5.1 Synopsis

Transient absorption (TA) spectroscopy is one of the most popular experimental methods to measure the excited state lifetimes and charge carrier recombination mechanisms in two dimensional (2D) semiconductors. This fundamental information is essential for designing and optimizing the next generation of ultrathin and lightweight 2D semiconductor-based optoelectronic devices. However, the interpretation of TA spectroscopy data has varied from group to group. The community lacks a unifying physical explanation for how and why experimental variables such as incident light intensity, sample-substrate interactions, and/or applied bias affect TA spectral data. This Perspective article (1) compares the physical chemistry-dominated TA literature to solid state physics-dominated literature from a historical perspective, (2) reviews

[2] This chapter contains work adapted from Sayer, T. Farah, Y. R. Austin, R. Trion formation resolves observed peak shifts in the optical spectra of transition metal dichalcogenides. *Nano Letters*, 23 (13) 6035-6041, 2023 & Almaraz, R. Sayer, T. Toole, J. Austin, R. Farah, Quantifying interfacial energetics of 2D semiconductor electrodes using in situ spectroelectrochemistry and many-body theory. *EES*, 16 (10) 4522-4529, 2023.

multiple physical explanations that the TA community developed to explain spectral features and experimental trends; (3) provides a unifying explanation for how and why trions contribute to TA spectra; and (4) quantifies the extent to which different physical interpretations and data analysis procedures yield different timescales and mechanisms for the same set of experimental results. We highlight the importance of considering trions in TA measurements and their implications for advancing our understanding of 2D material properties.

**5.2 Introduction**

Atomically thin semiconductor transition metal dichalcogenides (2D TMDs) are potentially transformative materials for lightweight and efficient opto-electronic devices (*1*, *2*). The fundamental physical processes for any light-driven applications such as photodetectors or photovoltaics are charge carrier generation, separation, and transport. The charge carrier generation step involves incident photon absorption by the 2D semiconductor, creating either free carriers (electrons and holes) or Coulombically bound electron-hole pairs (excitons) depending on the excitation energy. Excitons can also bind to or interact with an excess electron (or hole) to create a stable trion due to the enhanced Coulombic interaction in 2D TMDs (*3*). Accurately characterizing the exciton and trion lifetimes and factors that shorten or prolong those lifetimes are critical for optoelectronic device design. In general, the probability of separating and transporting free carriers, excitons, and/or trions to electrical contacts increases if the species lifetime increases. Hence, quantifying carrier lifetimes and recombination pathways is extremely valuable for designing and optimizing 2D optoelectronic devices.

One of the most widely used techniques to characterize exciton dynamics and lifetimes in 2D materials is transient absorption (TA) spectroscopy. However, the 2D TMD TA literature data varies vastly from group to group even though the experiments are performed with nominally

identical materials and similar experimental setups. While there is general agreement on reported exciton lifetimes (10-100s of ps), different physical explanations and mechanisms have been proposed to explain how and why TA spectral peaks shift, broaden, and change in intensity. While there have been numerous ultrafast TA spectroscopy studies and review articles (*4–18*) focusing on exciton formation and decay dynamics in 2D TMDs, we believe the dynamics of many-body particles, particularly trions, remain largely underappreciated and misunderstood. Researchers have yet to extensively investigate discrepancies observed between samples and how experimental conditions influence many-body dynamics. The key point of this Perspective article is that trion formation contributes to the observed optical spectrum of 2D TMDs and complicates the interpretation of ultrafast TA spectroscopy data. The magnitude of the trion-induced effects on TA data depends on *both* the carrier concentration ($n$), or doping, of the sample *and* the carrier generation rate (i.e., pump fluence) employed in the spectroscopic experiment. In this Perspective, we aim to provide a unifying physical explanation for TA experiments of 2D semiconductors and point out how and why TA data varies from experiment to experiment.

This Perspective article begins with a brief overview of the optical properties of 2D semiconductors. We discuss how TA data is collected and point out how spectral features vary from group to group. We present a timeline of the seminal papers in the field and discuss the evolution of TA data analysis and interpretation from 2013 to today. We then provide a new perspective that bridges the gap between disparate research communities and emphasizes the significance of trion formation in room temperature TA measurements.

### 5.3 Optical Properties and TA Spectroscopy Data of 2D TMDs

*What spectral features appear in 2D TMD absorbance measurements and how do their intensity fluctuations and energy shifts teach us about exciton and trion lifetimes?* We discuss the answers to these questions in the context of the most widely studied 2D TMD sample: monolayer

(ML) $MoS_2$. Note, trion formation is common to all 2D TMDs (*19*). Figure 5-1a-b shows a simple energy level scheme that depicts the electronic transitions responsible for the steady-state absorbance spectrum of a ML-$MoS_2$ sample. Three prominent peaks appear in the absorbance spectrum. The lower energy peaks at 1.87 eV and 2.11 eV are due to the A and B excitons, respectively. The high energy C-exciton at 2.98 eV is shown in green shading in Figure 5-a (*20*). The C-exciton comprises a broad distribution of states (represented by thick shaded region in Figure 5-1a) and, therefore, has a much larger absorbance signal than the A and B excitons (*21*).

The steady state absorbance spectrum can vary from sample to sample. Figure 5-c shows representative absorbance spectra of three different ML-$MoS_2$ samples. The exciton peak heights, energies, and lineshapes exhibit subtle variations. *Why do researchers observe different absorbance spectra for nominally identically prepared samples?* The short answer is the 2D semiconductor's electronic properties (i.e., *n*) matter. Later, we describe the fundamental many-body physics that connects the sample's electronic properties (i.e., *n*) to the observed absorbance peak heights, positions, and widths.

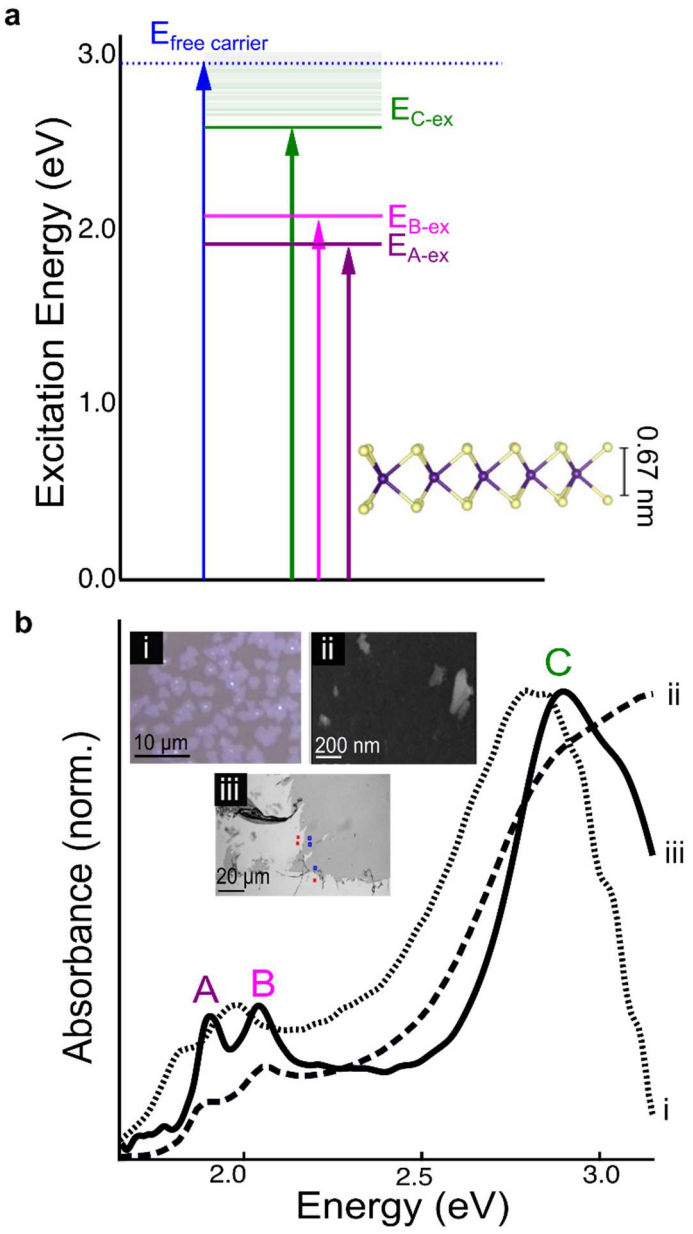


Figure 5-1. a) Band energy scheme of monolayer $MoS_2$ adapted from Austin et al. (*22*). B) Steady-state absorbance spectrum of multiple ML-$MoS_2$ samples reproduced from literature. Dotted absorbance spectrum corresponds to image i, dashed absorbance spectrum corresponds to image ii, and solid absorbance spectrum corresponds to image iii. Inset: i) image of ML triangle $MoS_2$ reprinted with permission from Aleithan et al (ref (*23*). Copyright 2016 by the American Physical Society. ii) Image of liquid-phase exfoliation $MoS_2$ flakes reproduced from Morabito et al. (ref (*24*)with permission from the Royal Society of Chemistry iii) CVD-grown large area ML-$MoS_2$ from Austin et al (ref 22).

Before we discuss the complicated nature of 2D TMD TA data, we briefly review how TA experiments work and define the necessary terminology for researchers who do not work in the TA community. In a typical TA experiment (Figure 5-2a), a femtosecond pump pulse creates an excited state population of excitons and/or free carriers in the sample. For ML-$MoS_2$, a pump pulse whose energy is equal to or greater than the C-exciton energy in Figure 5-1a generates both free carriers and C-excitons (*22*). On the other hand, a pump pulse whose energy equals the A and B transitions in Figure 5-1a generates only bound excitons. After a tunable delay time ($\tau$), a broadband probe pulse measures the absorbance of the sample in the excited state. The absorbance of the sample changes with time as the excited state populations decay between electronic states and eventually to the electronic ground state. The TA signal is given by $\Delta A(\tau) = A_{pump}(\tau) - A_{unpumped}$, where $A_{pump}(\tau)$ and $A_{unpumped}$ represent the absorbance values of the pumped and unpumped samples, respectively. One common feature in TA spectra is a so-called photobleach signal (Figure 5-2b). A photobleach signal appears in a TA spectrum as a peak with a negative DA value because a fraction of the electrons in the ground state have been promoted to the excited state and, therefore, the ground-state absorption in the excited sample is less than that in the non-excited sample (i.e., $A_{unpumped} > A_{pump}(\tau)$). A larger photobleach peak signal (i.e., more negative $\Delta A$) indicates a larger excited state population remains in the sample. Typically, a plot of the photobleach signal versus delay time starts at a large negative value and decays to zero as the excited state population decays back to the ground state.

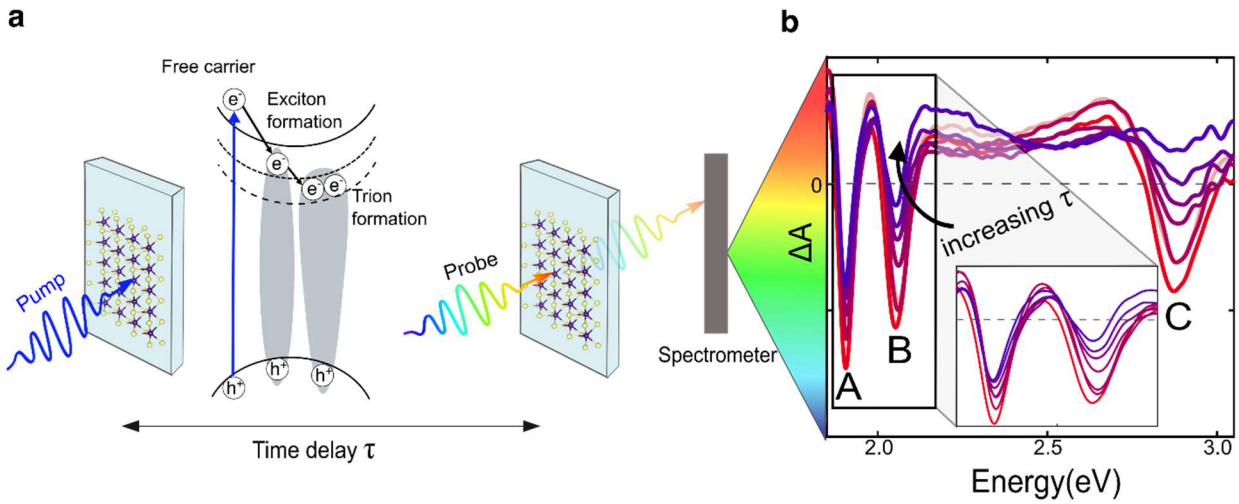


Figure 5-2. (a) Cartoon illustration of the pump-probe pulse sequence in a TA measurement. The pump pulse excites a ML-$MoS_2$ sample on a transparent substrate. The pump pulse excites electrons from the $MoS_2$ valence band to the conduction band, generating free electrons and holes. Those free carriers cool to form excitons. The broadband probe laser pulse is sent through the sample after a time delay $\tau$ and the transmitted light intensity is measured by the spectrometer as a change in the absorbance ($\Delta A$) versus probe energy (wavelength). (b) Representative TA data spectra of ML-$MoS_2$ at various time delays.

Having described the steady state absorbance spectrum and TA spectroscopy terminology, we now discuss what TA spectral features appear in ML-$MoS_2$ samples and how those spectral features vary from experiment to experiment. Consider the situation in Figure 5-2b, where a high energy 3.1 eV pump pulse creates free carriers in the sample. Figure 5-2c shows representative TA spectra at different time points following the pump pulse. A key observation in Figure 5-2c is that the A-exciton bleach signal exhibits significant peak shifting and broadening as a function of $\tau$. The peak shift direction and magnitude differs from experiment to experiment for the same material (*11*, *14*, *25*, *26*), as shown in Figure 5-3. Figure 5-3a shows TA data of a Si-supported ML-$WS_2$ sample over a range of pump intensities. At low pump fluence, a single sharp peak appears at about 2.0 eV, which can be assigned to the A-exciton. As pump fluence increases, the A-exciton broadens and shifts to lower energy (a "red-shift"). A clear shoulder appears at the highest pump fluences (indicated by black arrow in Figure 5-3a). The shoulder feature is caused

by trion formation. Figure 5-b shows ultrafast reflectance spectroscopy data of ML-$WS_2$ on fused silica (*25*). The A-exciton "splits" into two peaks at high pump fluence; the black arrow in Figure 5-3b. This pump fluence-dependent A-exciton shift/broadening effect is not unique to $WS_2$; all 2D TMDs exhibit this behavior. Figure 5-c-d shows pump-fluence dependent TA and reflectance data of ML-$MoS_2$. At high pump fluence, a second peak at 1.87 eV appears next to the A-exciton peak (see black arrow in Figure 5-3c) (*11*). In Figure 5-3d, a shoulder feature appears on the low-energy side of the A-exciton upon exciting a sapphire-supported ML-$MoS_2$ sample in a TA experiment.(*26*) All the black arrows in Figure 5-3 highlight the same common spectral signature: the trion. One interesting point about the "hiding place" of the trion in ML-$MoS_2$ absorbance spectra is that the shoulder peak is very close in energy to the exciton peak because the trion and exciton energy transitions differ by only 30 meV for this particular 2D semiconductor (*3*, *27*). In summary, the black arrows in Figure 5-3 indicate the trion "hiding in plain sight", where the subtle shoulder feature was either not assigned or the entire broad "superpeak" was collectively referred to as the A-exciton. The next section presents a historical timeline of how the trion spectral feature was discovered and discussed in two different research communities.

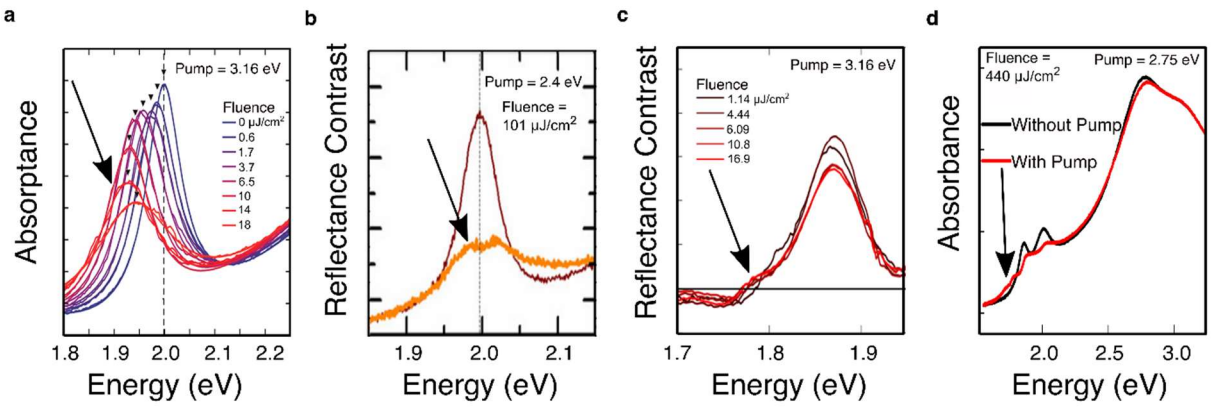


Figure 5-3. Examples of the trion spectral feature hiding in plain sight (indicated by black arrows). a) Pump fluence-dependent TA spectroscopy of Si-supported ML-$WS_2$ (*14*). Adapted with permission from Sie et at. Copyright 2017 American Chemical Society. b) Reflectance contrast measurements of ML-$WS_2$ on fused silica substrate (*25*). Adapted with permission from Ruppert

et al. Copyright 2017 American Chemical Society. c) Pump fluence-dependent reflectance contrast measurements of ML-$MoS_2$ on $SiO_2$/Si substrate (*11*). Adapted with permission from Trovatello et al. d) Comparison of ground state absorbance (black) with excited-state absorbance (red) of ML-$MoS_2$ on sapphire substrate (*26*). Reprinted with permission from Bera et al. Copyright 2021 by the American Physical Society.

### 5.4 Historical Timeline of the Hidden Trion

Here we provide our interpretation of how the 2D TMD TA spectroscopy literature evolved over time and compare that body of literature to the solid-state physics research community. Figure 5-4 shows a historical timeline of selected literature results from two "Camps". Camp 1 is largely a physics community performing steady state spectroscopy measurements of 2D semiconductors under electrical control in field effect transistor (FET) configurations. Camp 2 is largely a physical chemistry community performing ultrafast laser spectroscopy experiments of 2D semiconductors on various substrates. We mostly limited the literature references in Figure 5-4 to ML TMDs on substrates. However, we included selected ultrafast laser spectroscopy results of few layer-thick TMD dispersions (indicated by red boxes in Figure 5-4) because those papers specifically assign the trion feature in their spectra.

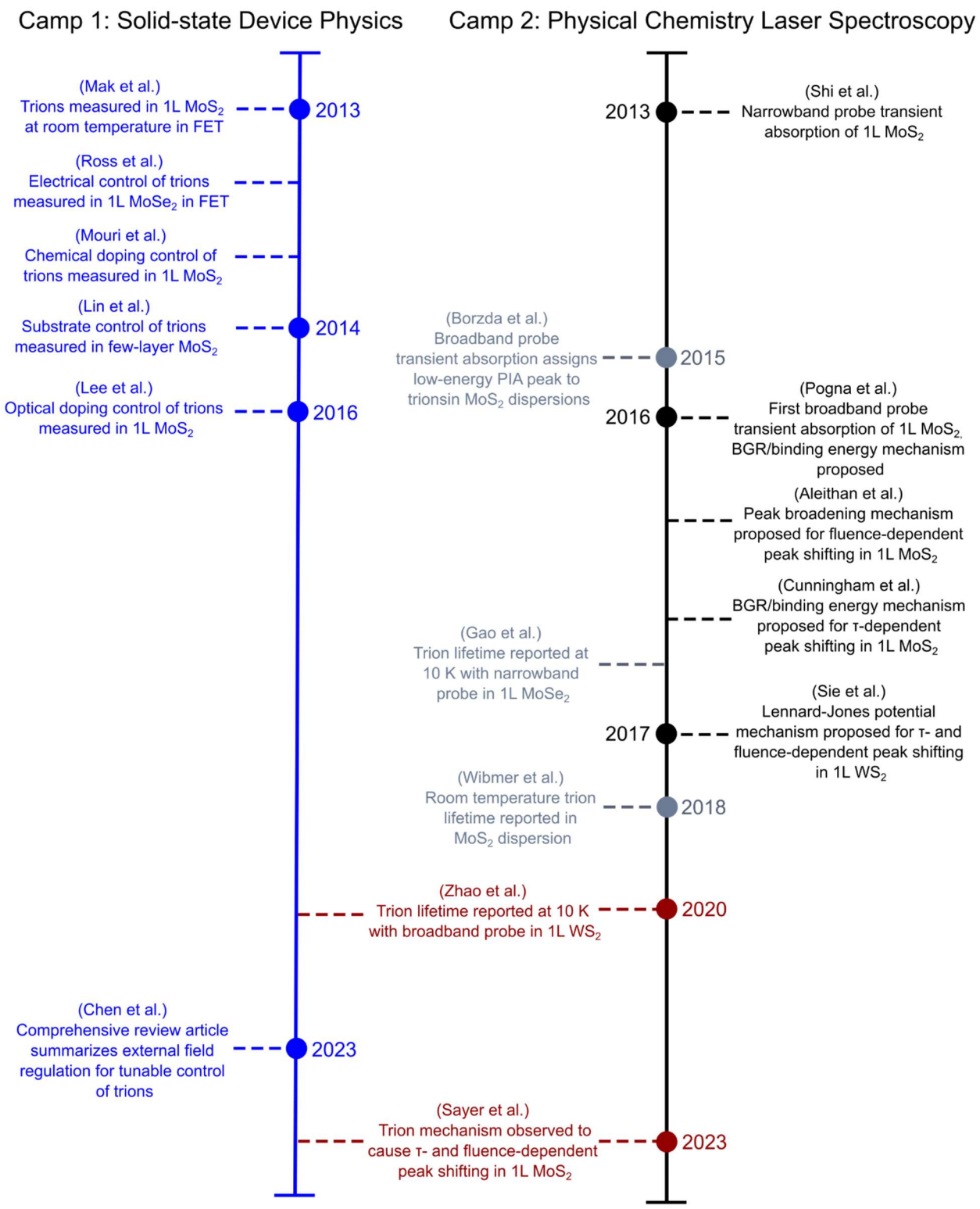


Figure 5-4. Historical timeline of selected 2D TMD TA spectroscopy literature alongside solid state physics-dominated trion literature.

*Camp 1: The solid state device physics literature*

In 2013, Mak et al (*3*) reported the first observation of trions in 2D semiconductors. To do so, the authors studied a ML-$MoS_2$ sample in a field-effect transistor (FET) configuration and measured temperature-dependent photoluminescence (PL) and absorbance spectra as a function of the gate voltage (which modulates *n*). The authors observed two distinct absorbance and PL peaks in the energy range from 1.8 to 2.0 eV. The authors used a many-body optical response model to assign the low and high energy peaks to the A-trion ($A^-$) and A-exciton ($A^0$), respectively. Their model explained how and why the back-gate voltage modulated the relative intensities and energies of $A^-$ and $A^0$, and the emergence of the trion with increasing *n* at room temperature. This work established a clear link between *n* and steady state absorbance/PL spectral features. Over the next few years, this camp produced additional studies that demonstrated how trion concentrations could be controlled in 2D TMDs using electrical doping (*28*), chemical doping (*29*), optical doping (*27*), and dielectric screening via substrate effects (*30*). The optical spectroscopy signatures of trions were further confirmed by negative photoconductivity measurements (*31*). We do not review that body of literature in this Perspective article and instead refer readers to comprehensive reviews (*19*, *32–34*). A recent review discusses other trion population modulation strategies, including using defect engineering, strain engineering, and electric, magnetic, and optical fields (*35*).

*Camp 2: Physical chemistry laser spectroscopy literature*

The first transient absorption experiments on ML TMDs were conducted by Shi et al. in 2013(*7*), just one year after the discovery of room temperature trions in 2D TMDs (*36*). In this experiment, a 3.20 eV laser pumped a freely suspended ML-$MoS_2$ sample, and the authors measured the TA signal at a fixed energy (1.85 eV). The authors fit the time-dependent TA signal at 1.85 eV with a tri-exponential decay function to extract time constants for three recombination

processes: (1) a fast 2-4 ps decay process due to exciton trapping by surface trap states; (2) an intermediate 30-80 ps decay process due to interband carrier-phonon scattering; and (3) a slow 300-1000 ps decay process due to direct interband electron-hole recombination. The exciton decay dynamics accelerated in regions of the sample supported by a $SiO_2/Si_3N_4$ substrate. However, the experimental setup did not allow the authors to acquire TA spectra as a function of probe wavelength, which precluded them from observing peak broadening and shifting in the A-exciton spectral region. We will explore how analyzing TA decay dynamics at a fixed energy affects the fitted time constant values in Section IV.

Pogna et al. performed the first broadband probe TA experiment on ML-$MoS_2$ in 2016(*37*). The broadband probe pulse enabled the authors to acquire spectral data and observe photo-bleach signals for the A-, B-, and C-exciton resonances. Importantly, the authors observed a photo-induced absorption (PIA) signal at a lower energy than the A-exciton. The authors attributed this red-shifted PIA signal to the bandgap renormalization (BGR) effect, where the electronic bandgap decreases with increasing carrier density due to excess photoexcited carriers generated by the pump pulse. The excess photogenerated carriers also cause a charge-screening effect. This screening effect reduces the Coulomb interaction between the electron and hole, thereby reducing the exciton binding energy. The authors concluded that the binding energy reduction opposes the BGR shift and results in only small, if any, observed changes in the optical gap. This rationale explains why the A-exciton peak (i.e., the optical gap) exhibits only minor energy shifts in the TA experiment. However, this work did not discuss the possibility that trions are responsible for the PIA signal.

A few months later, two separate broadband probe experiments on ML-$MoS_2$ were published by Aleithan et al (*23*) and Cunningham et al (*6*). Aleithan et al. observed shifting of the

A-exciton photobleach peak with increasing pump fluence. The authors proposed a new peak broadening mechanism to explain the observed peak shift. This physical explanation invokes collisional linewidth broadening due to collisions between excitons (*38*). On the other hand, Cunningham et al. attributed shifting of the A-exciton photobleach peak with increasing $\tau$ to the combination of BGR and binding energy reduction, as discussed above by Pogna et al (*37*). This combination of BGR and binding energy reduction quickly became a common explanation for A-exciton shifting in TA literature. A key point here is that two different research groups were studying similar samples with nearly identical techniques and proposed alternative explanations for similar data sets.

Before 2016, the TA spectroscopy community working with ML semiconductor samples on substrates did not assign the weak low energy spectral signature to trions. One possible explanation for the ambiguity of the trion spectral feature is that it overlapped heavily with the A-exciton signal, especially for ML-$MoS_2$. Researchers in Camp 1 already pointed out that increased linewidth broadening at high temperatures convolved the A-exciton and trion peaks (especially for ML-$MoS_2$) unless sufficiently high carrier concentrations were achieved (*3*). Interestingly, researchers who were performing TA experiments on 2D TMD dispersions assigned the trion peak in their spectral data (literature cited in grey font in Figure 5-). In 2015, Borzda et al (*39*) performed room-temperature TA spectroscopy measurements of few-layer $MoS_2$ dispersions and observed a red-shift of the A-exciton. The red-shifted signal was more pronounced at higher pump intensities and for shorter $\tau$. This work assigned the low-energy PIA signal at 1.85 eV to the trion for the first time. The authors analyzed the time-dependent TA signal using a pair of rate equations but did not discuss or quantify trion decay dynamics.

In 2016, Gao et al published the first low temperature TA measurements of substrate-supported ML 2D semiconductor samples (*40*). The authors cooled a ML-$MoSe_2$ sample to 10 K, then probed the sample at the peak trion resonance energy of 1.623 eV (taken from PL measurements). They fit their data to a biexponential decay function and reported a fast (5-35 ps) and slow (25-175 ps) timescale for trion decay dynamics. The authors did not assign the decay timescales to specific recombination processes; however, they did observe that trion lifetime increased as pump fluence increased. Since this experimental procedure did not allow for spectral data acquisition, peak shifting in the A-exciton spectral regions was not observed. Later, Zhao et al. performed similar low temperature measurements of ML-$WS_2$ in 2020, but with a broadband probe that enabled spectral data acquisition (*13*). This measurement finally provided TA data where the trion spectral signature was discernable from the A-exciton. The authors analyzed the TA decay signal at a fixed 2.05 eV energy with a biexponential decay function and reported two trion decay time constants: 0.6 ps and 108.6 ps, like the values reported by Gao et al. in 2016. They attributed these decay times to hot carrier relaxation and radiative decay of trions, respectively. While these papers advanced our ability to detect and assign the trion feature in TA experiments, the authors did not develop an explanation for why A-exciton and trion peaks shift and change in intensity with pump fluence and $\tau$.

Shortly after the initial low temperature TA measurements by Gao et al., Sie et al. reported an alternative explanation for how and why TA spectra in the A-exciton energy region vary with pump fluence and $\tau$ (*14*). In this experiment, the authors pumped a ML-$WS_2$ sample with 3.16 eV photons and observed a "redshift-blueshift crossover" in the A-exciton peak. The authors attributed the redshift-blueshift crossover to plasma effects and an attraction−repulsion crossover of the exciton−exciton interaction that mimics the Lennard-Jones potential between atoms. In this work,

the authors interpreted the entire spectral feature in the A-exciton energy region as a single peak (i.e., the A-exciton) and analyzed its time-dependent amplitude with a single component Gaussian function. Bera et al. also adopted this approach to explain the TA dynamics of ML-$MoS_2$ samples (*26*). In these room temperature experimental conditions, the trion "hides" beneath the A-exciton signal (note the trion "peaks out" of the data between $\tau$ = 0 and 0.12 ps in Figure 4a of ref (*14*)). The authors did not consider how trions influence the apparent A-exciton peak shift in their material-realistic computations and phenomenological modeling.

The first TA paper to report room-temperature trion dynamics was published three years later by Wibmer et al (*41*). The authors performed TA measurements on few-nm-thick $MoS_2$ dispersions and assigned the low energy photo-induced absorption peak at 1.75 eV to the trion, just like Borzda et al in 2015. However, the authors used a global analysis software (*42*) to assign the growth and decay of the trion to four timescales: two for the growth (3 ps and 45 ps) and two for the decay (250 ps and 1.6 ns). They observed that trion concentration increases with increasing pump fluence. Interestingly, their solvent-dependent results also agreed well with previous literature from the low-temperature FET community that showed sample preparation methods and local environment surrounding the sample affected the trion and exciton formation dynamics and lifetimes. Overall, the small community of researchers studying exciton dynamics in TMD dispersions were the only community during this time to report on room-temperature trion dynamics. However, this community was tracking trion dynamics using a photoinduced absorption feature (a positive-going peak in TA spectra) rather than resolving exciton versus trion peaks, as seen in low temperature TA measurements like Gao et al (*40*).

In our perspective, the TA spectroscopy literature of 2D TMD samples remained confusing until 2023, a decade after Heinz and co-workers observed trions at room temperature in ML-

$WS_2$(*3*). Some authors assigned the trion spectral feature while others did not. Multiple explanations were developed to explain the complicated spectral dynamics in these technically difficult measurements of ultrathin samples. The alternative explanations affected how the community processed, analyzed, interpreted, and ultimately quantified carrier recombination kinetics and mechanisms. By 2023, the community lacked a unifying explanation and physical model that could predict how variations in the experimental conditions (i.e., sample composition, pump fluence, and $\tau$) translate to changes in measured quantities (i.e., peak energy positions, intensities, and widths). In the next section, we describe our progress toward developing a model of minimal complexity that explains TA spectra of 2D TMDs using recent steady-state and time-resolved spectroscopy data of electrochemically gated ML-$MoS_2$ samples.

**5.5 Tag: the Trion's it - Influence of Trions on TA Spectra**

Before we discuss how we developed the ability to model 2D TMD TA spectra using many body theory, we first discuss how we developed and applied the model to fit steady state absorbance measurements of a ML-$MoS_2$ sample that served as a working electrode in an electrochemical cell (*43*). In this experiment, a ML-$MoS_2$ film was transferred to an indium doped tin oxide (ITO) substrate and immersed in a non-aqueous electrolyte. This electrochemically gated configuration (*44*) allowed us to control *n*; applying negative potentials increases *n* whereas positive potentials decrease *n*. Figure 5-5a shows potential-dependent absorbance data in the A and B-exciton energy region. The neutral A-exciton absorbance ($A^0$) dominates at more positive potentials. At more negative potentials, the negatively charged trion ($A^-$) dominates, resulting in a shoulder feature at 670 nm (Figure 5-5a). The potential-dependent trends in Figure 5-5a agree with literature spectroelectrochemistry data for thin films of few-layer $MoS_2$ nanosheets and colloidal film electrodes (*45*, *46*). However, previous electrochemical gating studies did not attempt to analyze the potential-dependent A-exciton lineshape. Next, we describe an approach to

quantitatively link the measured absorbance spectrum to *n* using a many-body model of minimal complexity to describe trion formation in ML transition metal dichalcogenides (TMDs) such as $MoS_2$ (*47*, *48*).

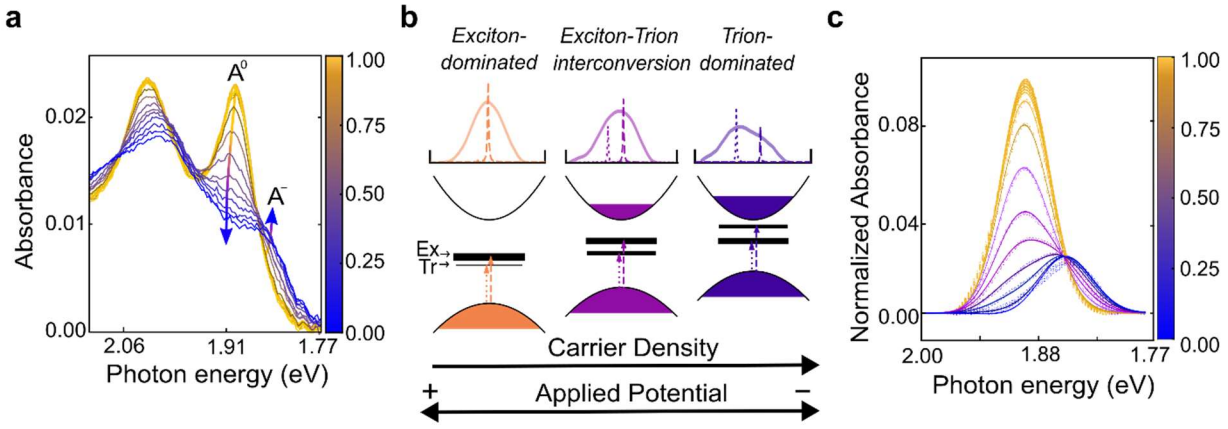


Figure 5-5. (a) Potential-dependent absorbance spectra of ML-$MoS_2$ in 0.25 M tetrabutylammonium hexafluorophosphate acetonitrile electrolyte. (b) Cartoon illustration of ML-$MoS_2$ electronic structure changes predicted by the MND model. The shading represents the carrier density. The exciton and trion optical transitions are labelled Ex and Tr, respectively. The simulated exciton and trion peaks are shown as short-dashed and long-dashed lines, respectively; and the solid line is the observed optical data. (c) Simulated and optimized absorbance spectra (solid lines) for each experimentally measured spectrum (circles).

We adopted a minimal many-body model of a Fermi polaron, put forth by Chang and Reichmann (*47*), to quantitatively analyze the steady state absorbance data. Our implementation is based on the Mahan-Noziéres-De Dominicis (MND) Hamiltonian (*49*) and computes an effective *n* that best describes the measured absorbance spectrum at each applied potential (*E*). The framework can be generally applied to 2D TMDs and is not specific to ML-$MoS_2$. A key feature of the model is its ability to capture how $A^0$ and $A^-$ resonances shift in energy and transfer oscillator strength between one another as a function of *n* (schematically shown in Figure 5-5b). The MND model considers the ML-$MoS_2$ sample is an *n*-doped 2D semiconductor at T = 0 K (*50*, *51*) where the majority carriers are conduction band electrons. For an unbiased or undoped sample (low *n*

condition in Figure 5-5b), the MND model predicts two peaks for the $A^0$ and $A^-$ transitions (dashed and dotted lines in Figure 5-5b-c). The oscillator strength is mostly associated with the higher energy $A^0$ transition, as indicated by the thick black line in Figure 5-5b. After convolving the calculated $A^0$ and $A^-$ linewidths to account for Gaussian broadening and the instrument response, we obtain a single broad peak (solid line in Figure 5-5c). The key point here is that the experimentalist observes a single gaussian-like absorbance peak at positive potentials because the oscillator strength is mostly associated with $A^0$ at low *n*. The situation changes as *n* increases (Figure 5-5b). The MND model predicts oscillator strength transfers from $A^0$ to $A^-$, as indicated by thicker lines for the $A^-$ transition in Figure 5-5b. The oscillator strength shift changes the $A^0$:$A^-$ peak intensity ratio. Also, the $A^0$ and $A^-$ peak energy shifts complicate the observed spectrum. The experimentalist observes a ‘‘superpeak’’ split into two discernable peaks (see convolved spectrum in Figure 5-5c). A key point of Figure 5-5 is that the MND model predicts how and why the ‘‘superpeak’’ absorbance feature at low *n* transitions to two separate peaks at high *n*. Next, we developed a fitting procedure that background subtracts the data and determines the single best *n* value at each *E* for the experimental data in Figure 5-5 (fitting procedure details are provided in references (*43*, *48*)). Figure 5-5c shows the results of the fitting procedure. The model captures all potential-dependent “superpeak” features, specifically how the $A^0$ and $A^-$peak intensities, positions, and widths change with applied potential (i.e., *n*).

A critical point of the above discussion is that the experimentalist measures the “superpeak” in room temperature absorbance spectroscopy of 2D TMD samples. In TA experiments, the “superpeak” evolves with pump fluence and $\tau$ in a complicated way because *n* continuously changes throughout the TA experiment. The magnitude and timescale of the observed “superpeak” shifts will depend on $n_0$ (defined by the sample growth conditions) and $\Delta n$ (defined by any charge

transfer between sample and substrate, the pump fluence, and the charge recombination dynamics). In our perspective, 2D TMD TA measurements may be performed in three different regimes that ultimately dictate the observed "superpeak" trends, as summarized in Figure 5-6.

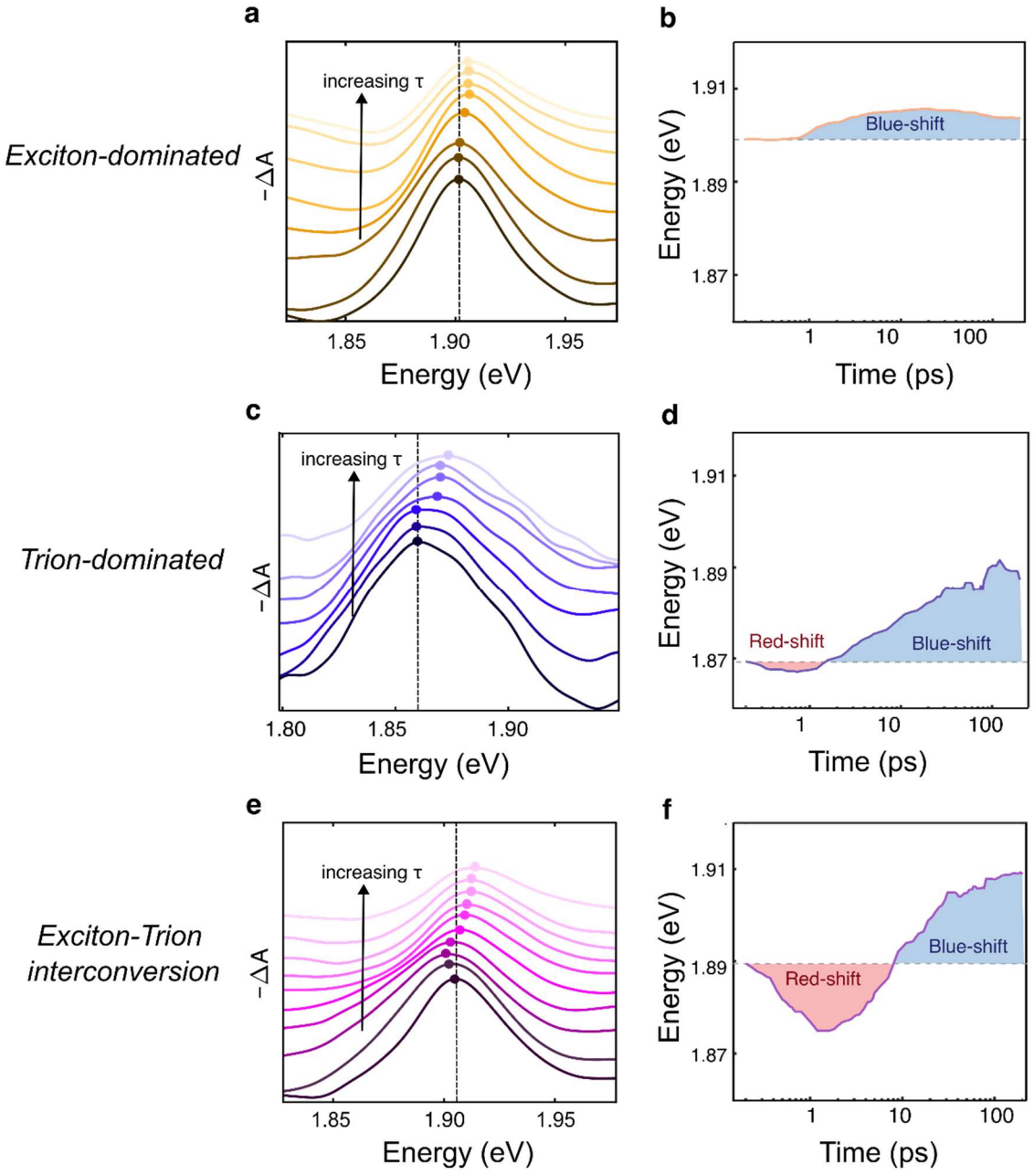


Figure 5-6. (A,C,E) "Superpeak" shifts observed for the exciton-dominated regime (low *n*), trion-dominated regime (high *n*), and the exciton-trion interconversion regime (intermediate *n*),

respectively. See main text for discussion. All these data stem from ML-$MoS_2$ experimental data in Figure 3 of reference (*22*). (B,D,F) Superpeak energy (denoted with a filled circle in panels A, C, E) versus $\tau$ for the three different regimes.

The exciton-dominated regime (Figure 5-6a-b) is a low *n* regime where $A^0$ dominates the observed "superpeak" at all time delays. For ML-$MoS_2$, an initial large negative photobleach signal is observed at 1.90 eV that can be assigned to $A^0$. The superpeak photobleach magnitude decreases with increasing $\tau$ as the A-exciton population decreases. A hallmark of this regime is that the "superpeak" exhibits a small blueshift over the first 10 ps, followed by no further shifting (Figure 5-6a-b). This blueshift could be due to (1) slight changes in the optical bandgap due to the combined effects of bandgap renormalization and binding energy reduction as shown in Figure 5-5b; both change with *n*; or (2) the Stark effect due to the local field of photogenerated charges (*39*).

The trion-dominated regime (Figure 5-6c-d) is a high *n* regime where $A^-$ dominates the spectrum at all time delays. Initially, a broad red-shifted "superpeak" appears at 1.86 eV that can be assigned to $A^-$ (Figure 5-6c). The "superpeak" shifts due to the *n*-dependent change in electronic band gap and trion binding energy. The hallmark of this regime is that the "superpeak" exhibits an initial small redshift with increasing $\tau$ (typically during the $1^{st}$ ps) due to the pump pulse increasing *n*, followed by a blueshift as *n* decreases with time.

Finally, the exciton-trion interconversion regime is an intermediate *n* regime where $A^0$ and $A^-$ contribute to the observed "superpeak" (Figure 5-6e-f). The "superpeak" exhibits dramatic energy shifts and broadening because the $A^0$ and $A^-$ resonances shift in energy and transfer oscillator strength between one another as *n* changes throughout the TA experiment (Figure 5-6e). As a result, the experimentalist observes a large redshift during the first 1-10 ps due to trion formation (Figure 5-6f), followed by a large blueshift as the trion population decays and oscillator strength transfers to the higher-energy $A^0$ peak. The magnitude of the redshift is nearly equal to that of the

blueshift because $A^0$ and $A^-$ contribute nearly equally to the observed "superpeak". This exciton-trion interconversion explains the observed "redshift-blueshift crossover" behavior observed in 2D TMD materials (*14*, *45*).

Another significant finding of our MND model is its prediction that the trion appears as a positive ΔA signal in TA experiments at low doping conditions (*48*). Figure 5-7 shows TA spectra of an electrochemically gated ML-$MoS_2$ sample at $\tau$ = 1 ps (*22*). The positive ΔA signal at low energy (<1.9 eV) is approximately the same magnitude at low (orange) and high *n* (purple) but is significantly higher at intermediate *n* (pink). This feature arises from pump-induced trion formation. The origin of the positive ΔA signal can be explained using steady-state absorbance spectral data. Figure 5-7b shows representative A-exciton region data at low and high *n* conditions. Figure 5-7c shows the difference between those two conditions. This steady-state difference spectrum matches the TA spectral lineshapes in Figure 5-7a. Hence, TA experiments will produce this positive ΔA signal if the experiment is conducted at low *n* conditions (e.g., low pump fluence and for low-doped samples). Trion formation explains the low energy "photo-induced absorption" feature in the A-exciton region of ML-$MoS_2$ TA data (*48*). Literature data has assigned this positive ΔA signal feature to the trion (*39*, *41*, *52*), but the origin of its time-dependent energy shift and dynamics were not discussed or quantitatively analyzed. In the next section, we demonstrate the MND model's unique ability to quantify both exciton and trion dynamics in TA experiments and compare those results to other data analysis approaches reported in the literature.

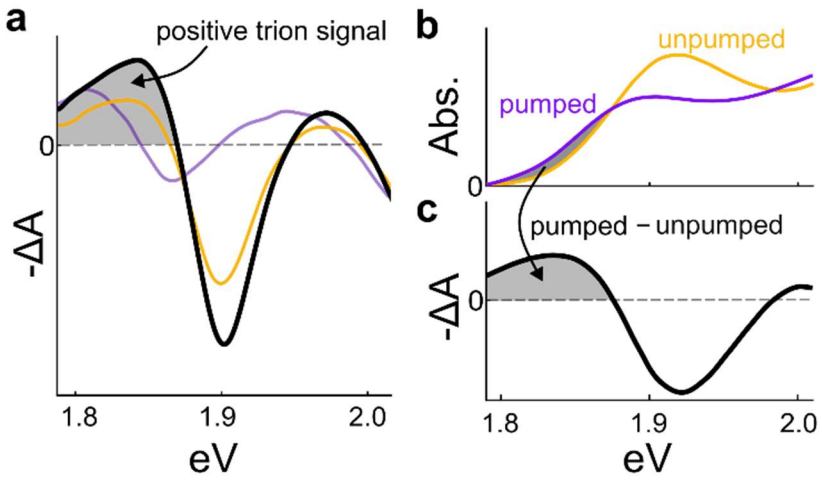


Figure 5-7. a) The positive TA signal caused by trions at specific carrier densities (black) highlighted with grey shading. The spectra for high doping (purple) and zero doping (orange) are overlayed for comparison. (b- c) Explanation of the black TA spectrum in panel (a) using steady state absorbance data. (b) Orange spectrum represents the low doping sample condition. The purple spectrum represents the trion-dominated regime (high doping) that occurs upon pumping the sample in a TA experiment. (c) The change in absorbance between the low and high doping regimes from panel (b).

Note, we did not discuss the B-exciton and B-trion in all the above cases. The B-exciton "superpeak" also shifts and broadens with increasing *n* (Figure 5-2b). Our implementation of the MND model (*43*, *48*) does not consider spin-orbit coupling due to the increased computational cost. The B-exciton "superpeak" likely contributes to the minor disagreement between theory and experiment in the high energy tail region of h. Future work could expand the MND model to include spin orbit coupling so that the spectral contribution and dynamics of the B-exciton and B-trion could be accurately quantified from 2D TMD TA data.

### 5.6 Influence of TA Data Analysis Methods on the Interpretation and Quantification of Exciton and Trion Dynamics of 2D TMDs.

Researchers in the physical chemistry community developed different physical explanations for, and data analysis methods to quantify, 2D TMD data. Note, the MND model is the only method that explicitly considers the population dynamics of both the exciton and trion. Here we analyze the same data set with three different approaches and discuss the outcomes of

each procedure. Figure 5-8a,c,e shows background subtracted TA data in the A-exciton energy for two different delay times: 1 ps and 25 ps (black and grey circles, respectively). This data set stems from a CVD-grown ML $MoS_2$ sample on a glass substrate excited by a 3.1 eV pump pulse (more experimental details are provided in the Supplementary Information of ref (*22*).

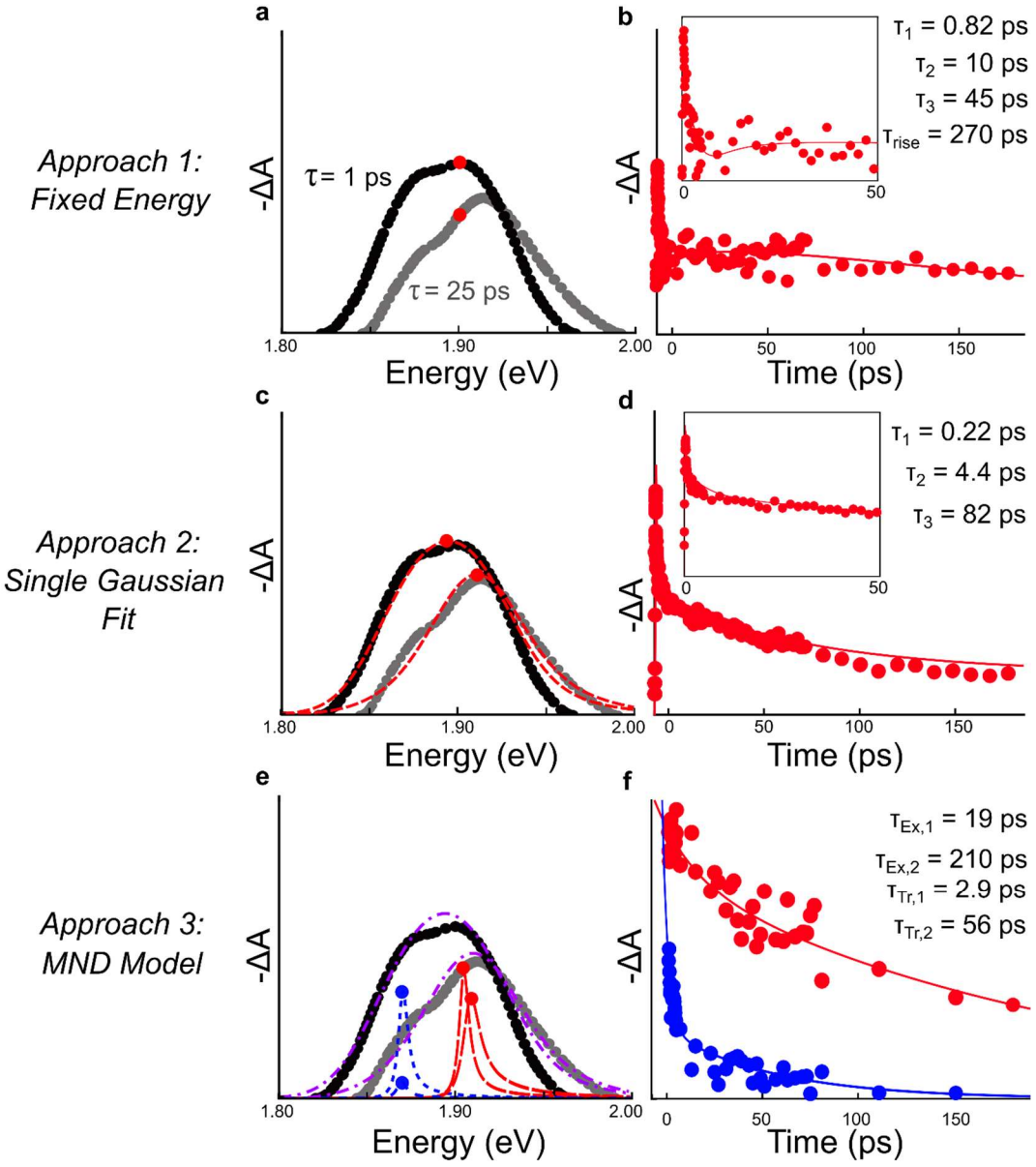


Figure 5-8. Comparison of 2D TMD TA data analysis approaches. (a-b) Illustration of the fixed energy analysis approach. (a) Background corrected TA data at two different pump-probe delay times: 1 ps and 25 ps (black and grey circles, respectively). This data set stems from a ML-$MoS_2$

sample on glass excited by a 3.1 eV pump pulse. The red circles denote the ΔA value obtained from each spectrum. (b) Kinetic trace (i.e., ΔA versus time values plotted as red circles) and multi-exponential fitting result (red line). (c-d) Illustration of the single gaussian fit approach. c) Same data as plotted in a) but using a gaussian function to fit the "superpeak" at each time delay. The peak of the gaussian fit (red circles) is obtained and plotted versus time in (d). (e-f) Illustration of the MND model approach. e) Same data as plotted in a) and c) but using the MND model to extract out both the trion peak (blue) and exciton peak (red) at each time delay. The magnitude for the trion (blue circle) and exciton (red circle) peaks are plotted versus time in f).

In Approach 1 (Figure 5-8a-b), the TA signal is analyzed at a fixed wavelength versus $\tau$ (red circles in Figure 5-8a), where the fixed wavelength value is typically defined as the "superpeak" maximum photobleach signal at some early time delay. One immediate problem with this approach is highlighted in Figure 5-8a. The "superpeak" position and lineshape expectedly changes with $\tau$ but the fixed energy approach does not take such changes into consideration. As a result, the interpretation and quantification of the carrier recombination mechanisms and timescales change dramatically. Figure 5-8b shows how the photobleach signal (–ΔA) versus $\tau$, or a kinetic trace, exhibits amplitude variance and an overall signal increase over the first 50 ps. These effects likely originate due to energy and intensity shifts of the underlying exciton and trion peaks that are convolved in the "superpeak." These effects drastically alter the interpretation of charge carrier dynamics mechanisms and timescale. Fitting this kinetic trace with a multiexponential function requires a second rising exponential term with a longer time constant (10s-100s of ps). The decay portion of the kinetic trace can be fit with three exponential decay terms, yielding fast, intermediate, and slow time constants that are consistent with literature and have been assigned to surface-defect trapping, carrier–phonon scattering, and electron–hole recombination processes, respectively (*7*, *9*). This fitting term suggests a longer population growth of the A-exciton, which could be assigned to B- and/or C-excitons cooling to form A-excitons.

In Approach 2 (Figure 5-8c-d), the entire "superpeak" in the A-exciton spectral region is fit with a single component Gaussian function (*6*, *22*, *23*). Like Approach 1, this Gaussian fitting strategy does not capture the underlying many body physics, specifically trion formation. Interestingly, this approach has an overall smoothing effect on the –ΔA versus $\tau$ kinetic trace (Figure 5-8d) and removes the rising feature seen at early $\tau$. The Gaussian method produces a kinetic trace with an ultrafast rise within the first 200 fs, followed by a smooth decay that can be fit with a tri-exponential function, yielding fast, intermediate, and slow time constants as in Approach 1. Note how the different data analysis approaches yield different time constant magnitudes.

In Approach 3 (Figure 5-8e-f), the "superpeak" is fit with the MND model, as explained in Section III. The MND model captures the exciton and trion energies and relative populations (values denoted by red and blue circles in Figure 5-8e). This approach enables researchers to deconvolute the slower exciton decay dynamics from the fast trion decay dynamics (Figure 5-8). Like Approach 2, we observe no signal increase feature at early $\tau$. The absence of this dynamic signature is significant because it would affect the interpretation of the charge carrier recombination mechanisms, such as the interpretation that B/C-excitons cool to form A-excitons (which could produce the increasing –ΔA signal). Another important outcome of Approach 3 is that two exponential decay terms are required to describe the decay dynamics. The trion population decays in about 50 ps whereas the exciton population is longer lived (100s of ps), in agreement with literature (*7*, *31*, *40*) that has assigned the fast decay constant to defect trapping. The key point is that Approach 3 successfully isolates and quantifies exciton and trion dynamics whereas Approaches 1-2 convolute the trion and exciton dynamics into a single decay curve that is

dominated by the trion dynamics at early times (1-50 ps) and then by the exciton dynamics at longer times.

In our perspective, it is imperative to establish best practices for collecting and analyzing 2D TMD TA data so that researchers can reliably observe and account for trion formation in their interpretation of carrier recombination mechanisms and timescale. One best practice is to replace single energy data collection with spectral acquisition using a broadband probe pulse. Spectral acquisition is necessary to observe trion formation and to implement the MND model. Single energy image acquisition is often performed in pump-probe microscopy experiments of 2D TMDs (*12*, *53*, *54*), which could muddle interpretation and quantification of exciton versus trion diffusion lengths. Another best practice is to use a reference probe line that does not travel through the sample for calculation and comparison of shot-to-shot ground state absorbance to excited state absorbance. This procedure allows for a direct determination of excited-state shifts that are not convoluted by the TA subtraction. Another important best practice is to acquire data with high energy resolution (e.g., $\leq$2 nm) in the A-exciton region; one could acquire lower energy resolution spectral data to simultaneously capture the A, B, and C-excitons. High resolution spectral data is necessary to resolve the convoluted exciton and trion peaks that make up the "superpeak" in Figure 5-8. Finally, before implementing the MND model, one possible "simple" test for distinguishing the regimes in Figure 5-6 is to fit the "superpeak" with two Gaussian functions and analyze the energy difference and relative population magnitude of the fitted peaks. If the energy difference exceeds 30 meV, then trion formation is likely contributing significantly to the observed spectrum and, therefore, the MND model should be implemented. We hope these best practices can enhance the fidelity and unify interpretations of 2D TMD data.

## 5.7 Conclusion

Many-body effects are prevalent at room-temperature in 2D TMDs, which highlights the need for a unifying physical picture that describes how and why quasiparticles form and decay in space and time. TA spectroscopy is a powerful technique for measuring and quantifying such effects if the community of spectroscopists and theorists can work together to advance many body theory such that it captures realistic experimental conditions (substrate, material defects, temperature, spin-orbit coupling) and design experiments such as multi-dimensional TA spectroscopies that will more accurately reveal how and why exciton and trion populations evolve over time. Understanding what experimental factors contribute to exciton and trion population growth and decay should ultimately allow for their rational control and tuning in next-generation ultrathin optoelectronic device applications. We envision the MND model being implemented for real-time device characterization. Any device component that modulates $n$ (e.g., back gate in a FET or metal-semiconductor contact) will likely impact the A-exciton region lineshape of 2D TMDs, especially for ML-$MoS_2$. Excitingly, the MND model can explain the underlying many body physics in the material and provide critical insight into how and why excitons and trions form and decay during device operation. However, the model has several underlying assumptions that must be addressed so that the fitting outcome can produce more accurate materials properties (i.e., $n$) and decay dynamics from the TA measurement. We expect interdisciplinary collaboration and knowledge exchange between solid-state device physicists, experimental physical chemists, and theorists will lead to breakthroughs in adopting and implementing spectroscopic measurements for 2D device characterization and development.

**References**


1. C. Wadia, A. P. Alivisatos, D. M. Kammen, Materials Availability Expands the Opportunity for Large-Scale Photovoltaics Deployment. *Environ. Sci. Technol.* **43**, 2072–2077 (2009).
2. Q. H. Wang, K. Kalantar-Zadeh, A. Kis, J. N. Coleman, M. S. Strano, Electronics and optoelectronics of two-dimensional transition metal dichalcogenides. *Nat Nanotechnol* **7**, 699–712 (2012).
3. K. F. Mak, K. He, C. Lee, G. H. Lee, J. Hone, T. F. Heinz, J. Shan, Tightly bound trions in monolayer MoS 2. *Nat Mater* **12**, 207–211 (2013).
4. S. Dal Conte, C. Trovatello, C. Gadermaier, G. Cerullo, Ultrafast Photophysics of 2D Semiconductors and Related Heterostructures. Cell Press [Preprint] (2020). https://doi.org/10.1016/j.trechm.2019.07.007.
5. G. Moody, J. Schaibley, A. X. Xu, Exciton Dynamics in Monolayer Transition Metal Dichalcogenides. doi: 10.1364/ao.XX.XXXXXX (2016).
6. P. D. Cunningham, K. M. McCreary, A. T. Hanbicki, M. Currie, B. T. Jonker, L. M. Hayden, Charge Trapping and Exciton Dynamics in Large-Area CVD Grown MoS2. *Journal of Physical Chemistry C* **120**, 5819–5826 (2016).
7. H. Shi, R. Yan, S. Bertolazzi, J. Brivio, B. Gao, A. Kis, D. Jena, H. G. Xing, L. Huang, Exciton dynamics in suspended monolayer and few-layer MoS2 2D crystals. *ACS Nano* **7**, 1072–1080 (2013).
8. J. Yuson, D. Contreras, M. Achterman, E. Jung, A. Boulesbaa, “Dynamics of exciton formation, recombination, and trapping in monolayers of 2D-TMD materials” (SPIE-Intl Soc Optical Eng, 2022), p. 34.

9. Y. Li, X. Wu, W. Liu, H. Xu, X. Liu, Revealing the interrelation between C- And A-exciton dynamics in monolayer WS2via transient absorption spectroscopy. *Appl Phys Lett* **119** (2021).

10. B. Kaviraj, D. Sahoo, Physics of excitons and their transport in two dimensional transition metal dichalcogenide semiconductors. Royal Society of Chemistry [Preprint] (2019). https://doi.org/10.1039/c9ra03769a.

11. C. Trovatello, F. Katsch, N. J. Borys, M. Selig, K. Yao, R. Borrego-Varillas, F. Scotognella, I. Kriegel, A. Yan, A. Zettl, P. J. Schuck, A. Knorr, G. Cerullo, S. D. Conte, The ultrafast onset of exciton formation in 2D semiconductors. *Nat Commun* **11** (2020).

12. N. S. Ginsberg, W. A. Tisdale, Spatially Resolved Exciton and Charge Transport in Emerging Semiconductors. *Annu Rev Phys Chem* **71** (2020).

13. J. Zhao, W. Zhao, W. Du, R. Su, Q. Xiong, Dynamics of exciton energy renormalization in monolayer transition metal disulfides. *Nano Res* **13**, 1399–1405 (2020).

14. E. J. Sie, A. Steinhoff, C. Gies, C. H. Lui, Q. Ma, M. Rösner, G. Schönhoff, F. Jahnke, T. O. Wehling, Y. H. Lee, J. Kong, P. Jarillo-Herrero, N. Gedik, Observation of Exciton Redshift-Blueshift Crossover in Monolayer WS2. *Nano Lett* **17**, 4210–4216 (2017).

15. S. Brem, M. Selig, G. Berghaeuser, E. Malic, Exciton Relaxation Cascade in two-dimensional Transition Metal Dichalcogenides. *Sci Rep* **8**, 1–8 (2018).

16. S. Sim, J. Park, J. G. Song, C. In, Y. S. Lee, H. Kim, H. Choi, Exciton dynamics in atomically thin MoS2: Interexcitonic interaction and broadening kinetics. *Phys Rev B Condens Matter Mater Phys* **88**, 1–5 (2013).

17. Y. Li, J. Shi, H. Chen, Y. Mi, W. Du, X. Sui, C. Jiang, W. Liu, H. Xu, X. Liu, Slow Cooling of High-Energy C Excitons Is Limited by Intervalley-Transfer in Monolayer MoS 2. *Laser Photon Rev* **13** (2019).

18. L. Wang, Z. Wang, H. Y. Wang, G. Grinblat, Y. L. Huang, D. Wang, X. H. Ye, X. Bin Li, Q. Bao, A. S. Wee, S. A. Maier, Q. D. Chen, M. L. Zhong, C. W. Qiu, H. B. Sun, Slow cooling and efficient extraction of C-exciton hot carriers in MoS2 monolayer. *Nat Commun* **8** (2017).

19. X. Zheng, X. Zhang, "Excitons in Two-Dimensional Materials;" www.intechopen.com.

20. A. Carvalho, R. M. Ribeiro, A. H. Castro Neto, Band nesting and the optical response of two-dimensional semiconducting transition metal dichalcogenides. *Phys Rev B Condens Matter Mater Phys* **88** (2013).

21. D. Y. Qiu, F. H. Da Jornada, S. G. Louie, Optical spectrum of MoS2: Many-body effects and diversity of exciton states. *Phys Rev Lett* **111** (2013).

22. R. Austin, Y. R. Farah, T. Sayer, B. M. Luther, A. Montoya-Castillo, A. T. Krummel, J. B. Sambur, Hot carrier extraction from 2D semiconductor photoelectrodes. *Proc Natl Acad Sci U S A* **120** (2023).

23. S. H. Aleithan, M. Y. Livshits, S. Khadka, J. J. Rack, M. E. Kordesch, E. Stinaff, Broadband femtosecond transient absorption spectroscopy for a CVD Mo S2 monolayer. *Phys Rev B* **94** (2016).

24. F. Morabito, K. Synnatschke, J. D. Mehew, S. Varghese, C. J. Sayers, G. Folpini, A. Petrozza, G. Cerullo, K.-J. Tielrooij, J. Coleman, V. Nicolosi, C. Gadermaier, Long lived photogenerated charge carriers in few-layer transition metal dichalcogenides obtained from liquid phase exfoliation. *Nanoscale Adv*, doi: 10.1039/d3na00862b (2024).

25. C. Ruppert, A. Chernikov, H. M. Hill, A. F. Rigosi, T. F. Heinz, The Role of Electronic and Phononic Excitation in the Optical Response of Monolayer WS2 after Ultrafast Excitation. *Nano Lett* **17**, 644–651 (2017).

26. S. K. Bera, M. Shrivastava, K. Bramhachari, H. Zhang, A. K. Poonia, D. Mandal, E. M. Miller, M. C. Beard, A. Agarwal, K. V. Adarsh, Atomlike interaction and optically tunable giant band-gap renormalization in large-area atomically thin MoS2. *Phys Rev B* **104** (2021).

27. H. S. Lee, M. S. Kim, H. Kim, Y. H. Lee, Identifying multiexcitons in Mo S2 monolayers at room temperature. *Phys Rev B* **93** (2016).

28. J. S. Ross, S. Wu, H. Yu, N. J. Ghimire, A. M. Jones, G. Aivazian, J. Yan, D. G. Mandrus, D. Xiao, W. Yao, X. Xu, Electrical control of neutral and charged excitons in a monolayer semiconductor. *Nat Commun* **4** (2013).

29. S. Mouri, Y. Miyauchi, K. Matsuda, Tunable photoluminescence of monolayer MoS2 via chemical doping. *Nano Lett* **13**, 5944–5948 (2013).

30. Y. Lin, X. Ling, L. Yu, S. Huang, A. L. Hsu, Y. H. Lee, J. Kong, M. S. Dresselhaus, T. Palacios, Dielectric screening of excitons and trions in single-layer MoS2. *Nano Lett* **14**, 5569–5576 (2014).

31. C. H. Lui, A. J. Frenzel, D. V. Pilon, Y. H. Lee, X. Ling, G. M. Akselrod, J. Kong, N. Gedik, Trion-induced negative photoconductivity in monolayer MoS2. *Phys Rev Lett* **113** (2014).

32. M. V. Durnev, M. M. Glazov, Excitons and trions in two-dimensional semiconductors based on transition metal dichalcogenides. *Uspekhi Fizicheskih Nauk* **188**, 913–934 (2018).

33. W. Zheng, Y. Jiang, X. Hu, H. Li, Z. Zeng, X. Wang, A. Pan, Light Emission Properties of 2D Transition Metal Dichalcogenides: Fundamentals and Applications. Wiley-VCH Verlag [Preprint] (2018). https://doi.org/10.1002/adom.201800420.

34. J. Pei, J. Yang, T. Yildirim, H. Zhang, Y. Lu, Many-Body Complexes in 2D Semiconductors. Wiley-VCH Verlag [Preprint] (2019). https://doi.org/10.1002/adma.201706945.

35. W. Chen, C. Zheng, J. Pei, H. Zhan, External field regulation strategies for exciton dynamics in 2D TMDs. *Opt Mater Express* **13**, 1007 (2023).

36. K. F. Mak, C. Lee, G.-H. Lee, "Observation of tightly bound trions in monolayer MoS2" (2012); https://www.researchgate.net/publication/232735679.

37. E. A. A. Pogna, M. Marsili, D. De Fazio, S. Dal Conte, C. Manzoni, D. Sangalli, D. Yoon, A. Lombardo, A. C. Ferrari, A. Marini, G. Cerullo, D. Prezzi, Photo-induced bandgap renormalization governs the ultrafast response of single-layer MoS2. *ACS Nano* **10**, 1182–1188 (2016).

38. S. Sim, J. Park, J. G. Song, C. In, Y. S. Lee, H. Kim, H. Choi, Exciton dynamics in atomically thin MoS2: Interexcitonic interaction and broadening kinetics. *Phys Rev B Condens Matter Mater Phys* **88** (2013).

39. T. Borzda, C. Gadermaier, N. Vujicic, P. Topolovsek, M. Borovsak, T. Mertelj, D. Viola, C. Manzoni, E. A. A. Pogna, D. Brida, M. R. Antognazza, F. Scotognella, G. Lanzani, G. Cerullo, D. Mihailovic, Charge photogeneration in few-layer MoS2. *Adv Funct Mater* **25**, 3351–3358 (2015).

40. F. Gao, Y. Gong, M. Titze, R. Almeida, P. M. Ajayan, H. Li, Valley trion dynamics in monolayer MoSe2. *Phys Rev B* **94** (2016).

41. L. Wibmer, S. Lages, T. Unruh, D. M. Guldi, Excitons and Trions in One-Photon- and Two-Photon-Excited MoS2: A Study in Dispersions. *Advanced Materials* **30** (2018).

42. J. J. Snellenburg, S. P. Laptenok, R. Seger, K. M. Mullen, I. H. M. Van Stokkum, “Glotaran: A Java-Based Graphical User Interface for the R Package TIMP” (2012); http://www.jstatsoft.org/.

43. R. Almaraz, T. Sayer, J. Toole, R. Austin, Y. Farah, N. Trainor, J. M. Redwing, A. Krummel, A. Montoya-Castillo, J. Sambur, Quantifying interfacial energetics of 2D semiconductor electrodes using in situ spectroelectrochemistry and many-body theory. *Energy Environ Sci* **16**, 4522–4529 (2023).

44. M. Velický, Electrolyte versus Dielectric Gating of Two-Dimensional Materials. American Chemical Society [Preprint] (2021). https://doi.org/10.1021/acs.jpcc.1c04795.

45. G. M. Carroll, H. Zhang, J. R. Dunklin, E. M. Miller, N. R. Neale, J. Van De Lagemaat, Unique interfacial thermodynamics of few-layer 2D MoS2 for (photo)electrochemical catalysis. *Energy Environ Sci* **12**, 1648–1656 (2019).

46. K. M. Wurst, O. Strolka, J. Hiller, J. Keck, A. J. Meixner, J. Lauth, M. Scheele, Electronic Structure of Colloidal 2H-MoS2 Mono and Bilayers Determined by Spectroelectrochemistry. *Small* **19** (2023).

47. Y. W. Chang, D. R. Reichman, Many-body theory of optical absorption in doped two-dimensional semiconductors. *Phys Rev B* **99** (2019).

48. T. Sayer, Y. R. Farah, R. Austin, J. Sambur, A. T. Krummel, A. Montoya-Castillo, Trion Formation Resolves Observed Peak Shifts in the Optical Spectra of Transition-Metal Dichalcogenides. *Nano Lett* **23**, 6035–6041 (2023).

49. G. D. Mahan, “Many-Particle Physics THIRD EDITION” (2000).

50. K. Kang, S. Xie, L. Huang, Y. Han, P. Y. Huang, K. F. Mak, C. J. Kim, D. Muller, J. Park, High-mobility three-atom-thick semiconducting films with wafer-scale homogeneity. *Nature* **520**, 656–660 (2015).

51. A. Sebastian, R. Pendurthi, T. H. Choudhury, J. M. Redwing, S. Das, Benchmarking monolayer MoS2 and WS2 field-effect transistors. *Nat Commun* **12** (2021).

52. Y. Y. Yue, L. Y. Zhao, D. A. Han, L. Wang, H. Y. Wang, B. R. Gao, H. B. Sun, Trion dynamics and charge photogeneration in MoS2nanosheets prepared by liquid phase exfoliation. *Physical Chemistry Chemical Physics* **23**, 22430–22436 (2021).

53. Y. Wan, Z. Guo, T. Zhu, S. Yan, J. Johnson, L. Huang, Cooperative singlet and triplet exciton transport in tetracene crystals visualized by ultrafast microscopy. *Nat Chem* **7**, 785–792 (2015).

54. E. M. Grumstrup, M. M. Gabriel, E. E. M. Cating, E. M. Van Goethem, J. M. Papanikolas, Pump-probe microscopy: Visualization and spectroscopy of ultrafast dynamics at the nanoscale. Elsevier B.V. [Preprint] (2015). https://doi.org/10.1016/j.chemphys.2015.07.006.

# Chapter 6 : CONCLUSIONS

The research presented in this dissertation has covered the ultrafast dynamics of charge carriers, the prevalence of many-body effects on optical spectra, and extraction of hot carriers within 2-dimensional transition metal dichalcogenide photoelectrochemical devices. The objectives of my research were twofold: 1) to quantify the extraction of hot carriers in monolayer TMD photoelectrochemical cells under operational conditions, and 2) to investigate the influence of operational device parameters, such as applied bias and charge transfer with sub-and-superstates, on the dynamics of charge carriers, excitons, and trions in monolayer TMDs.

In Chapter 1, the broader motivations for this research and 2D TMD materials are introduced. In Chapter 2, background information on charge carrier generation in 2D semiconductors, spectroelectrochemistry as technique to study charge extraction, and transient absorption as a technique to study in-operando charge carrier energetics and dynamics are introduced. Detailed experiment design and methods are provided in Chapter 3. Chapter 4 discusses hot carrier extraction from 2D TMD photoelectrodes. Chapter 5 explores the influence of trions on the optical spectra of 2D TMDs, as well as my perspective on the presence of room-temperature trions within previously published data and their impact on the interpretation of charge carrier dynamics.

To measure hot carrier extraction and charge carrier dynamics, I employed a combination of photoelectrochemical techniques and in situ transient absorption spectroscopy measurements. Through these experiments, I have demonstrated the ultrafast (<50 fs) extraction of hot excitons and free carriers under applied bias in a proof-of-concept photoelectrochemical solar cell fabricated using abundant and potentially inexpensive monolayer $MoS_2$. Additionally, my research has revealed that both steady-state and transient absorption spectra of 2D TMDs broaden and shift

with carrier concentration, fluence, and time. This shifting phenomenon arises from the formation of negative trions, which can exist at room temperature and dominate the optical spectra of 2D TMDs at high carrier concentrations.

In summary, the results presented herein have provided valuable insights into the mechanisms governing charge carrier dynamics in 2D TMDs. These findings contribute to the design and optimization of hot carrier solar energy devices with higher efficiencies than those achievable with current technology. The findings of this work offer novel contributions to the existing body of knowledge of solar photoelectrochemistry and nonlinear spectroscopy of 2-dimensional electrodes.

# APPENDIX I: $WO_3$ NANOPARTICLES AS A PROLOGUE FOR MY PHD

The start of my PhD career began in the summer of 2019, when I joined the Sambur group working on tungsten oxide nanoparticle synthesis. I had the privilege of being mentored by Dr. R. Colby Evans, continuing work on his research project of $WO_3$ nanorods for electrochromic smart windows. Colby has published work on single particle coloration efficiency of $WO_3$ nanorods, where he showed that different surface facets of hexagonal $WO_3$ with {100} facets had different ion intercalation "windows" in the crystal structure. He posited that the coloration efficiency of $WO_3$ nanorods could be modified by synthesizing $WO_3$ with different surface facets that contained more optically-active ion channels. This was then my goal upon joining the project: to synthesize $WO_3$ nanoparticles with different surface facets.

I spent the summer synthesizing mostly unusable amorphous samples. Months of trial and error until stumbling upon success turned out to be foreshadowing for the rest of my PhD career. All was not in vain though, as my repeated attempts to make these samples did provide me with fundamental knowledge needed to start my PhD project. I learned fundamental electrochemistry, including the basics of 3-electrode electrochemical cells. I learned how to take images and measurements on optical microscopes. I learned that solving problems you didn't anticipate is what makes up about 90% of research. And I learned that valuable information can be gleaned from taking absorbance measurements.

Once I had finally synthesized $WO_3$ nanoparticles that had a defined $\{\mathbf{1}\bar{2}0\}$ surface facet, the next step was to compare them to Colby's $WO_3$ nanoparticles. We electro-optically characterized the particles by measuring their change in light absorbance when $Li^+$ ions were inserted and removed. We found that while the $\{\mathbf{1}\bar{2}0\}$ sample got less dark than Colby's {100} sample, it had better cycling stability, meaning that it could reliably darken the same amount for

more than 500 cycles. The results indicated surface facet and particle morphology engineering are viable strategies to enhance the CE and long-term stability/lifetime in electrochromic thin films for smart window applications.

This work was integral to my PhD career, as it taught me many practical lab skills that enabled my success in my future project on 2D TMDs. Using my $WO_3$ samples, I learned how to construct optically-transparent electrochemical cells. I learned how to take 3-electrode measurements on a potentiostat, how to take and interpret a cyclic voltammogram, and how to measure visible light absorbance of a sample as a function of applied voltage. This last skill became particularly essential for my 2D TMD research, as potential-dependent absorption measurements provided essential data to the work discussed in Chapters 4 and 5, and lead to three publications.

I highlight this work and my experience with it here, as this work will not be discussed in detail in my dissertation. I instead refer the reader to the publication of this work for further details.

**Reference**

Evans, R. C., Austin, R., Miller, R. C., Preston, A., Nilsson, Z. N., Ma, K., & Sambur, J. B. (2021). Surface-Facet-Dependent Electrochromic Properties of $WO_3$ Nanorod Thin Films: Implications for Smart Windows. *ACS Applied Nano Materials*, *4*(4), 3750–3759.

# APPENDIX II: MATLAB CODE

The Matlab code used to calculate photocurrent spectra is provided below for reference.

```
%% import daq

[photocurrent_time, photocurrent_lock_in_current,photocurrent_mono_lockin,
photocurrent_potential] = func_importWinDAQUVVis('C:\Users\raraa\OneDrive -
Colostate\Paper #1 all data\electrochemistry
data\Photocurrent\windaq_Ch1mono_Ch2potential_Ch3lockin_photocurrent_5nmsteps_MoS2.tx
t');

%% make wavelength axis

startpt=755; % start scan point
increment=-5; % scan increment
endpt=405; % end point of scan
photocurrent_lockin_Wavelengths=[startpt:increment:endpt]'; % make a column of
wavelengths
photocurrent_lockin_WavelengthAbs_mono =
repmat(photocurrent_lockin_Wavelengths,33,1); % repeat the wavelengths
%% plot raw daq data
photocurrent_mono_lockin = photocurrent_mono_lockin;
photocurrent_lock_in_current_flipped = photocurrent_lock_in_current *-1;
photocurrent_potential_flipped_lockin = photocurrent_potential;
figure()
hold on
plot(photocurrent_mono_lockin,'ro-')
plot(photocurrent_potential_flipped_lockin,'bo-')
plot(photocurrent_lock_in_current_flipped,'go-')
legend('mono','potential','current');
hold off

%% pick threshold values to determine on/off points for the triggers

figure()

plot(diff(photocurrent_mono_lockin),'ro-')
%xlim([3200 3700])
%%
monodig=diff(photocurrent_mono_lockin)<0.4;
figure()
plot(monodig,'ro-')
%% find mono on/off points

monotrigglowtreshold=0.4; % look at the derivative of the mono trigger and pick a
value that is below the high points

% get the trigger points
[photocurrent_Monoonpts,photocurrent_Monooffpts]=func_GetMonoTriggerPts(photocurrent_
mono_lockin,monotrigglowtreshold);
```

```
%% get Current vs wavelength

[photocurrent_spectrum] = func_CalcPCspectrum(photocurrent_lock_in_current_flipped,
photocurrent_Monoonpts, photocurrent_Monooffpts);
%%
figure()
hold on
plot(photocurrent_lockin_WavelengthAbs_mono(1:2301),photocurrent_spectrum)
xlabel('Wavelength (nm)'); ylabel('Windaq Signal from Lock-in Amplifier (V)');
title('Photocurrent 1L-MoS2');
hold off

%% Separate PC data into the different potentials

start_potential = 0.55;
end_potential = 0.35;
increment = -0.025;
potentials=[start_potential:increment:end_potential]'; % make a column of potentials

% 0.55 V
pc_start_055 = find(photocurrent_potential(900:571092)>0.54 &
photocurrent_potential(900:571092)<0.56,1)+ 900; % exclude the first 30 seconds of
data before the ivium was turned on
pc_end_055 = find(photocurrent_potential(900:571092)>0.525 &
photocurrent_potential(900:571092)<0.54,1) + 900;
pc_mono_055 = find(photocurrent_Monoonpts>pc_start_055 &
photocurrent_Monoonpts<pc_end_055);
pc_055 = photocurrent_spectrum(pc_mono_055(1):pc_mono_055(size(pc_mono_055)),1);
pc_Wavelengths_055 =
photocurrent_lockin_WavelengthAbs_mono(pc_mono_055(1):pc_mono_055(size(pc_mono_055)))
;

%0.525 V
pc_start_0525 = find(photocurrent_potential(900:571092)>0.515 &
photocurrent_potential(900:571092)<0.535,1)+ 900; % exclude the first 30 seconds of
data before the ivium was turned on
pc_end_0525 = find(photocurrent_potential(900:571092)>0.50 &
photocurrent_potential(900:571092)<0.515,1) + 900;
pc_mono_0525 = find(photocurrent_Monoonpts>pc_start_0525 &
photocurrent_Monoonpts<pc_end_0525);
pc_0525 = photocurrent_spectrum(pc_mono_0525(1):pc_mono_0525(size(pc_mono_0525)),1);
pc_Wavelengths_0525 =
photocurrent_lockin_WavelengthAbs_mono(pc_mono_0525(1):pc_mono_0525(size(pc_mono_0525
)));

%0.50 V
pc_start_050 = find(photocurrent_potential(900:571092)>0.49 &
photocurrent_potential(900:571092)<0.51,1)+ 900; % exclude the first 30 seconds of
data before the ivium was turned on
pc_end_050 = find(photocurrent_potential(900:571092)>0.475 &
photocurrent_potential(900:571092)<0.49,1) + 900;
pc_mono_050 = find(photocurrent_Monoonpts>pc_start_050 &
photocurrent_Monoonpts<pc_end_050);
pc_050 = photocurrent_spectrum(pc_mono_050(1):pc_mono_050(size(pc_mono_050)),1);
```

```
pc_Wavelengths_050 =
photocurrent_lockin_WavelengthAbs_mono(pc_mono_050(1):pc_mono_050(size(pc_mono_050)))
;

%0.475 V
pc_start_0475 = find(photocurrent_potential(900:571092)>0.465 &
photocurrent_potential(900:571092)<0.485,1)+ 900; % exclude the first 30 seconds of
data before the ivium was turned on
pc_end_0475 = find(photocurrent_potential(900:571092)>0.45 &
photocurrent_potential(900:571092)<0.465,1) + 900;
pc_mono_0475 = find(photocurrent_Monoonpts>pc_start_0475 &
photocurrent_Monoonpts<pc_end_0475);
pc_0475 = photocurrent_spectrum(pc_mono_0475(1):pc_mono_0475(size(pc_mono_0475)),1);
pc_Wavelengths_0475 =
photocurrent_lockin_WavelengthAbs_mono(pc_mono_0475(1):pc_mono_0475(size(pc_mono_0475
)));

% 0.45 V
pc_start_045 = find(photocurrent_potential(900:571092)>0.44 &
photocurrent_potential(900:571092)<0.46,1)+ 900; % exclude the first 30 seconds of
data before the ivium was turned on
pc_end_045 = find(photocurrent_potential(900:571092)>0.425 &
photocurrent_potential(900:571092)<0.44,1) + 900;
pc_mono_045 = find(photocurrent_Monoonpts>pc_start_045 &
photocurrent_Monoonpts<pc_end_045);
pc_045 = photocurrent_spectrum(pc_mono_045(1):pc_mono_045(size(pc_mono_045)),1);
pc_Wavelengths_045 =
photocurrent_lockin_WavelengthAbs_mono(pc_mono_045(1):pc_mono_045(size(pc_mono_045)))
;

%0.425 V
pc_start_0425 = find(photocurrent_potential(900:571092)>0.415 &
photocurrent_potential(900:571092)<0.435,1)+ 900; % exclude the first 30 seconds of
data before the ivium was turned on
pc_end_0425 = find(photocurrent_potential(900:571092)>0.40 &
photocurrent_potential(900:571092)<0.415,1) + 900;
pc_mono_0425 = find(photocurrent_Monoonpts>pc_start_0425 &
photocurrent_Monoonpts<pc_end_0425);
pc_0425 = photocurrent_spectrum(pc_mono_0425(1):pc_mono_0425(size(pc_mono_0425)),1);
pc_Wavelengths_0425 =
photocurrent_lockin_WavelengthAbs_mono(pc_mono_0425(1):pc_mono_0425(size(pc_mono_0425
)));

%0.40 V
pc_start_040 = find(photocurrent_potential(900:571092)>0.39 &
photocurrent_potential(900:571092)<0.41,1)+ 900; % exclude the first 30 seconds of
data before the ivium was turned on
pc_end_040 = find(photocurrent_potential(900:571092)>0.375 &
photocurrent_potential(900:571092)<0.39,1) + 900;
pc_mono_040 = find(photocurrent_Monoonpts>pc_start_040 &
photocurrent_Monoonpts<pc_end_040);
pc_040 = photocurrent_spectrum(pc_mono_040(1):pc_mono_040(size(pc_mono_040)),1);
pc_Wavelengths_040 =
photocurrent_lockin_WavelengthAbs_mono(pc_mono_040(1):pc_mono_040(size(pc_mono_040)))
;
```

```
%0.375 V
pc_start_0375 = find(photocurrent_potential(900:571092)>0.365 &
photocurrent_potential(900:571092)<0.385,1)+ 900; % exclude the first 30 seconds of
data before the ivium was turned on
pc_end_0375 = find(photocurrent_potential(900:571092)>0.35 &
photocurrent_potential(900:571092)<0.365,1) + 900;
pc_mono_0375 = find(photocurrent_Monoonpts>pc_start_0375 &
photocurrent_Monoonpts<pc_end_0375);
pc_0375 = photocurrent_spectrum(pc_mono_0375(1):pc_mono_0375(size(pc_mono_0375)),1);
pc_Wavelengths_0375 =
photocurrent_lockin_WavelengthAbs_mono(pc_mono_0375(1):pc_mono_0375(size(pc_mono_0375
)));

% 0.35 V
pc_start_035 = find(photocurrent_potential(900:571092)>0.34 &
photocurrent_potential(900:571092)<0.36,1)+ 900; % exclude the first 30 seconds of
data before the ivium was turned on
pc_end_035 = find(photocurrent_potential(900:571092)>0.325 &
photocurrent_potential(900:571092)<0.34,1) + 900;
pc_mono_035 = find(photocurrent_Monoonpts>pc_start_035 &
photocurrent_Monoonpts<pc_end_035);
pc_035 = photocurrent_spectrum(pc_mono_035(1):pc_mono_035(size(pc_mono_035)),1);
pc_Wavelengths_035 =
photocurrent_lockin_WavelengthAbs_mono(pc_mono_035(1):pc_mono_035(size(pc_mono_035)))
;



%%

figure()
hold on
scatter(pc_Wavelengths_055,pc_055)
scatter(pc_Wavelengths_0525,pc_0525)
scatter(pc_Wavelengths_050,pc_050)
scatter(pc_Wavelengths_0475,pc_0475)
scatter(pc_Wavelengths_045,pc_045)
scatter(pc_Wavelengths_0425,pc_0425)
scatter(pc_Wavelengths_040,pc_040)
scatter(pc_Wavelengths_0375,pc_0375)
scatter(pc_Wavelengths_035,pc_035)

legend('0.55V','0.525V','0.5V','0.475V','0.45V','0.425V','0.4V','0.375V','0.35V')

xlabel('Wavelength (nm)')
ylabel('Photocurrent')
hold off

%% now average each potential

[pc_wl_055,~,idx] = unique(pc_Wavelengths_055); % Unique x's and their locations
(each wavelength)
pc_mean_055 = accumarray(idx,pc_055,[],@mean);
```

```
[pc_wl_0525,~,idx] = unique(pc_Wavelengths_0525); % Unique x's and their locations
(each wavelength)
pc_mean_0525 = accumarray(idx,pc_0525,[],@mean);

[pc_wl_050,~,idx] = unique(pc_Wavelengths_050); % Unique x's and their locations
(each wavelength)
pc_mean_050 = accumarray(idx,pc_050,[],@mean);

[pc_wl_0475,~,idx] = unique(pc_Wavelengths_0475); % Unique x's and their locations
(each wavelength)
pc_mean_0475 = accumarray(idx,pc_0475,[],@mean);

[pc_wl_045,~,idx] = unique(pc_Wavelengths_045); % Unique x's and their locations
(each wavelength)
pc_mean_045 = accumarray(idx,pc_045,[],@mean);

[pc_wl_0425,~,idx] = unique(pc_Wavelengths_0425); % Unique x's and their locations
(each wavelength)
pc_mean_0425 = accumarray(idx,pc_0425,[],@mean);

[pc_wl_040,~,idx] = unique(pc_Wavelengths_040); % Unique x's and their locations
(each wavelength)
pc_mean_040 = accumarray(idx,pc_040,[],@mean);

[pc_wl_0375,~,idx] = unique(pc_Wavelengths_0375); % Unique x's and their locations
(each wavelength)
pc_mean_0375 = accumarray(idx,pc_0375,[],@mean);

[pc_wl_035,~,idx] = unique(pc_Wavelengths_035); % Unique x's and their locations
(each wavelength)
pc_mean_035 = accumarray(idx,pc_035,[],@mean);

%% plot all potentials
map = brewermap(9,'RdYlBu');
f=figure;
ax = gca(f);ax.ColorOrder = map;
hold on;

scatter(pc_wl_055,pc_mean_055, 'filled')
scatter(pc_wl_0525,pc_mean_0525, 'filled')
scatter(pc_wl_050,pc_mean_050, 'filled')
scatter(pc_wl_0475,pc_mean_0475, 'filled')
scatter(pc_wl_045,pc_mean_045, 'filled')
scatter(pc_wl_0425,pc_mean_0425, 'filled')
scatter(pc_wl_040,pc_mean_040, 'filled')
scatter(pc_wl_0375,pc_mean_0375, 'filled')
scatter(pc_wl_035,pc_mean_035, 'filled')

xlabel('Wavelength (nm)'); ylabel('Photocurrent Signal'); title('Photocurrent
Spectra');
legend('0.55V','0.525V','0.50V','0.475V', '0.45V', '0.425V','0.40V','0.375V',
'0.35V')
%% convert mono power daq signal into real current
currvswavelength_mono_corr = photocurrent_spectrum * 0.00001; %1 V = 10 uA
conversion???
```

```
figure()
hold on
plot(photocurrent_lockin_WavelengthAbs_mono(1:350),currvswavelength_mono_corr)
xlabel('Wavelength (nm)'); ylabel('Current (A)'); title('Monocromator Power
Measurement');
hold off
% When the potentiostat outputs 1 V, the current is the full current range (10 uA)


%% convert the photodiode current into power using the power measured at 600 nm

% power at 600 nm was measured to be 45.5 uW
% find the current at 600 nm (this is index # 156)
% use responsivity curve for conversion of current (A) to power (W) at each
% wavelength
PD_responsivity_W = zeros(351,2);
PD_responsivity_W(:,1) = webdigitizerPDresponsivity(:,1);
PD_responsivity_W(:,2) = webdigitizerPDresponsivity(:,2) .^(-1); %convert from A/W to
W/A
%%

%current_600nm = currvswavelength_mono_corr(156);
power_conversion_factor = PD_responsivity_W(:,2); %divide the watts by the current to
get the conversion in (W/A)

powervswavelength_mono_corr = currvswavelength_mono_corr .*
power_conversion_factor(1:350).*17.3657; % 0.575841 is the measured A/W (0.2012967)
over the responsivity curve A/W (0.34957) @ 600 nm

figure()
hold on
plot(photocurrent_lockin_WavelengthAbs_mono(1:350),powervswavelength_mono_corr)
xlabel('Wavelength (nm)'); ylabel('Power (W)'); title('Mono Power Spectrum');

%% Pull out the Watts at each wavelength we measure photocurrent at
 power_mono_corr = zeros(176,1);

for i = 1:175
    X = find(photocurrent_lockin_WavelengthAbs_mono == WavelengthAbs(i)) % find the
index of the wavelength of interest
    power_mono_corr(i) = powervswavelength_mono_corr(X); % use that index to find the
power
end

figure()
hold on
plot(WavelengthAbs, power_mono_corr)
xlabel('Wavelength (nm)'); ylabel('Power (W)')
hold off
%% caculate the power of each wavelength in the variable WavelengthAbs

WavelengthAbs_meters = WavelengthAbs .* (1e-9); % convert nm to m
h = 6.626e-34; % planck's constant in J*s
c = 2.998e8; % speed of light in m/s
```

```
EnergyAbs = (h*c)./(WavelengthAbs_meters);
%% calculate EQE
q = 1.602e-19; %fundametal   Cbuchogmn e o
% EQE = (Current * Energy)/(q * Power)
conversion_factor = EnergyAbs ./ (q .* power_mono_corr);

EQE_040 = photocurrvswavelength_040.* conversion_factor(1:175);
EQE_045 = photocurrvswavelength_0450.* conversion_factor(1:175);
EQE_050 = photocurrvswavelength_050.* conversion_factor(1:175);
EQE_0525 = photocurrvswavelength_0525.* conversion_factor(1:175);
EQE_055 = photocurrvswavelength_055.* conversion_factor;

figure()
hold on
plot(WavelengthAbs(1:175), EQE_040 *100)
plot(WavelengthAbs(1:175), EQE_045*100)
plot(WavelengthAbs(1:175), EQE_050*100)
plot(WavelengthAbs(1:175), EQE_0525*100)
plot(WavelengthAbs, EQE_055*100)
xlabel('Wavelength (nm)'); ylabel('EQE (%)')
legend('0.4V','0.45V','0.5V','0.525V','0.55V')
hold off

%% calculate IQE

% IQE = EQE/(1 - T- R) where T is the fraction of photons transmitted and R
% is the fraction of photons reflected

% convert OD to %T using the equation T = 10^(-OD) % these follow the axis
% of 405 - 755

T_ODmean_040 = 10 .^(-ODmean_040);
T_ODmean_045 = 10 .^(-ODmean_045);
T_ODmean_050 = 10 .^(-ODmean_050);
T_ODmean_0525 = 10 .^(-pc_mean_0525);
T_ODmean_055 = 10 .^(-pc_mean_055);

R = 0.12; % From Li's paper, he states in the SI that 12% of incident photons reflect
from the TMD surface (& 10% reflect from the covership?)
%%
% take the EQE at each wavelength and divide it by 0.88 - T at each
% wavelength (0.88 comes from 1 - R where R is wavelength independent)

% The wavelength axis for EQE is WavelengthAbs and the wavelength axis for
% OD is wavelength_040
EQE_OD_wavelengths_040 = zeros(70,1);
EQE_OD_wavelengths_045 = zeros(70,1);
EQE_OD_wavelengths_050 = zeros(70,1);
EQE_OD_wavelengths_0525 = zeros(70,1);
EQE_OD_wavelengths_055 = zeros(70,1);
%%

for i = 2:71
```

```
    Y = find(WavelengthAbs == wavelength_040(i) | WavelengthAbs ==
wavelength_040(i)+1) % find the index of the wavelength of interest

    EQE_OD_wavelengths_040(i) = EQE_040(Y); % use that index to find the power
    EQE_OD_wavelengths_045(i) = EQE_045(Y); % use that index to find the power
    EQE_OD_wavelengths_050(i) = EQE_050(Y); % use that index to find the power
    EQE_OD_wavelengths_0525(i) = EQE_0525(Y); % use that index to find the power
    EQE_OD_wavelengths_055(i) = EQE_055(Y); % use that index to find the power %
these EQE_OD_wavelengths have matching wavelengths to wavelength_040
end

IQE_040 = EQE_OD_wavelengths_040 ./ (1 - T_ODmean_040);
IQE_045 = EQE_OD_wavelengths_045 ./ (1 - T_ODmean_045);
IQE_050 = EQE_OD_wavelengths_050 ./ (1 - T_ODmean_050);
IQE_0525 = EQE_OD_wavelengths_0525 ./ (1 - T_ODmean_0525);
IQE_055 = EQE_OD_wavelengths_055 ./ (1 - T_ODmean_055);

%%
figure()
hold on
plot(wavelength_040, IQE_040*100)
plot(wavelength_040, IQE_045*100)
plot(wavelength_040, IQE_050*100)
plot(wavelength_040, IQE_0525*100)
plot(wavelength_040, IQE_055*100)
xlabel('Wavelength (nm)'); ylabel('IQE (%)')
legend('0.4V','0.45V','0.5V','0.525V','0.55V')
hold off

%% import the mono power spectrum taken with the photodiode


%[photodiode_time, photodiode_mono, photodiode_lockin] =
func_importWinDAQUVVis('C:\Users\raraa\OneDrive - Colostate\New MoS2 EChem
Data\windaq_monopowerspectrum.txt');
% manually import the file windaq_monopowerspectrum.txt
photodiode_time = windaq_monopowerspectrum(:,1);
photodiode_mono = windaq_monopowerspectrum(:,3);
photodiode_lockin = windaq_monopowerspectrum(:,2);

% make wavelength axis
startpt=755; % start scan point
increment=-1; % scan increment
endpt=405; % end point of scan
photodiode_Wavelengths=[startpt:increment:endpt]'; % make a column of wavelengths

% plot raw daq data
photodiode_lockin_flipped = photodiode_lockin *-1;

figure()
hold on
plot(photodiode_mono,'ro-')
plot(photodiode_lockin_flipped,'bo-')
legend('mono','current');
hold off
```

```
%% find mono on/off points
monotrigglowtreshold=0.4; % look at the derivative of the mono trigger and pick a
value that is below the high points

% get the trigger points
[photodiode_Monoonpts,photodiode_Monooffpts]=func_GetMonoTriggerPts(photodiode_mono,m
onotrigglowtreshold);

% get Current vs wavelength
[photodiode_mono_spectrum] = func_CalcPCspectrum(photodiode_lockin_flipped,
photodiode_Monoonpts, photodiode_Monooffpts);
%
figure()
hold on
plot(photodiode_Wavelengths,photodiode_mono_spectrum)
xlabel('Wavelength (nm)'); ylabel('Lamp Signal from Lock-in Amplifier (V)');
hold off
%% convert the measured windaq signal (V) into photodiode current (A) and then
photodiode current into mono power (W)
%convert windaq signal into current
photodiode_600nm_signal_V = photodiode_mono_spectrum(156); % measured windaq signal
in V at 600 nm
photodiode_600nm_power_W = 45.5e-6; % measured power of the mono light in W at 600 nm
photodiode_600nm_responsivity_AperW = 0.3495; % the responsivity of the photodiode
(A/W) at 600nm
photodiode_600nm_current_A = photodiode_600nm_power_W *
photodiode_600nm_responsivity_AperW;
photodiode_signaltocurrent_conv_factor = photodiode_600nm_current_A /
photodiode_600nm_signal_V; %conversion between windaq signal and photodiode current
(A/V)
% use conversion factor to go from windaq signal to photodiode current
photodiode_mono_spectrum_current = photodiode_mono_spectrum .*
photodiode_signaltocurrent_conv_factor;

figure()
hold on
plot(photodiode_Wavelengths,photodiode_mono_spectrum_current)
xlabel('Wavelength (nm)'); ylabel('Photodiode Current (A)');
hold off
%%
% now use the responsivity curve of the photodiode to go from photodiode
% current to mono power

responsivity_sorted_WperA = webplotdigitizerPDresponsivity_sorted(:,2).^(-1);
%responsivity curve is in A/W but we need to convert using W/A
mono_power_spectrum = photodiode_mono_spectrum_current .* responsivity_sorted_WperA;
figure()
hold on
plot(photodiode_Wavelengths, mono_power_spectrum)
xlabel('Wavelength (nm)'); ylabel('Power (W)'); title('Mono Power Spectrum');

%% Pull out the Watts at each wavelength we measure photocurrent at
 mono_power_spectrum_corr = zeros(71,1);
```

```
for i = 1:71
    X = find(photodiode_Wavelengths == pc_wl_040(i)) % find the index of the
wavelength of interest
   mono_power_spectrum_corr(i) = mono_power_spectrum(X); % use that index to find the
power
end

figure()
hold on
plot(pc_wl_040, mono_power_spectrum_corr)
xlabel('Wavelength (nm)'); ylabel('Power (W)')
hold off
%% caculate the power of each wavelength in the variable 'pc_wl_040'

pc_wl_040_meters = pc_wl_040 .* (1e-9); % convert nm to m
h = 6.626e-34; % planck's constant in J*s
c = 2.998e8; % speed of light in m/s

EnergyAbs = (h*c)./(pc_wl_040_meters);
%% calculate EQE

pc_lockin_data_Amps = cat(2, pc_mean_035.*11.3e-9, pc_mean_0375.*11.3e-9,
pc_mean_040.*11.3e-9, pc_mean_0425_exout.*11.3e-9, pc_mean_045.*11.3e-9,
pc_mean_0475.*11.3e-9,pc_mean_050.*11.3e-9, pc_mean_0525.*11.3e-9,
pc_mean_055.*11.3e-9);
q = 1.602e-19; %fundametal charge
% EQE = (Current * Energy)/(q * Power)
conversion_factor = EnergyAbs ./ (q .* mono_power_spectrum_corr);
pc_lockin_data_EQE = zeros(71,9);

for i = 1:9
    pc_lockin_data_EQE(:,i) = pc_lockin_data_Amps(:,i).* conversion_factor;
end

map = brewermap(9,'RdYlBu');
f=figure;
ax = gca(f);ax.ColorOrder = map;
hold on;
plot(pc_wl_040, pc_lockin_data_EQE(:,1).*100)
plot(pc_wl_040, pc_lockin_data_EQE(:,2).*100)
plot(pc_wl_040, pc_lockin_data_EQE(:,3).*100)
plot(pc_wl_040, pc_lockin_data_EQE(:,4).*100)
plot(pc_wl_040, pc_lockin_data_EQE(:,5).*100)
plot(pc_wl_040, pc_lockin_data_EQE(:,6).*100)
plot(pc_wl_040, pc_lockin_data_EQE(:,7).*100)
plot(pc_wl_040, pc_lockin_data_EQE(:,8).*100)
plot(pc_wl_040, pc_lockin_data_EQE(:,9).*100)
xlabel('Wavelength (nm)'); ylabel('EQE (%)')
legend('0.35V','0.375V','0.4V','0.425V','0.45V','0.475V','0.50V','0.525V','0.55V')
hold off
```

The Matlab code for potential-dependent photocurrent spectra is provided below for reference.

```
% order of code operations: import windaq data, import images, separate
% images by what potential was applied, then sync images to mono wavelength
%
%% import daq

[time,ivium,camera,mono] = func_importWinDAQUVVis('D:\Rachelle\2021-11-18\Potential
Dependent OD\windaq_Ch1mono_Ch2potential_Ch3camera_Potential_dependent_OD_MoS2.txt');

%% make wavelength axis

startpt=755; % start scan point
increment=-5; % scan increment
endpt=405; % end point of scan
Wavelengths=[startpt:increment:endpt]'; % make a column of wavelengths
WavelengthAbs_mono = repmat(Wavelengths,75,1); % repeat the wavelengths
%% plot raw daq data
mono = mono *-1;
ivium = ivium *-1;
figure()
hold on
plot(time,mono,'ro-')
plot(time,camera,'bo-')
plot(time,ivium,'go-')
legend('mono','camera','ivium');
hold off

%% pick threshold values to determine on/off points for the triggers
%close all
figure()

monodiff = diff(mono);
plot(monodiff,'ro-')
%xlim([3200 3700])

%% find camera and mono on/off points

monotrigglowtreshold=1.5; % look at the derivative of the mono trigger and pick a
value that is below the high points
camerahighthresh=126.5; % look at the absolute of the prime trigger and pick a value
that is below the high points
% get the trigger points
[Monoonpts,Monooffpts,Cameraonpts,Cameraoffpts]=func_GetTriggerPts(mono,camera,monotr
igglowtreshold,camerahighthresh);
%delete the first Monooffpnts value and the last Monoonpnts value
%% Draw the region that you want to measure absorbance spectrum
% loads the average img computed from all
image=double(imread('D:\Rachelle\2021-11-18\Potential Dependent OD\avg_image.tif'));
contrast=[961 3684]; % define the image contrast, probably from image j
 warning('off');
%% point and click I and I0 masks, 3x3, USE THIS
boxsize=3;
[Mask_IHJ,Mask_I0HJ]=func_PointClickMasks(image,contrast,boxsize);
```

```
%% change image naming and put all images into one folder
mv='D:\Rachelle\2021-11-18\Potential Dependent OD\Pos0\Pos0'

[ODTrajHJ]=func_GetWholeTrajectory(mv,Mask_IHJ,Mask_I0HJ);

%% get OD vs wavelength

[ODvsWavelengthHJ]=func_CalcAbsSpectrum(ODTrajHJ,Monoonpts,Monooffpts,Cameraonpts,Cam
eraoffpts)
%% average thE different spots

ODvsWavelength_cat = cat(3,ODvsWavelengthHJ{:});
ODvsWavelength_avg = mean(ODvsWavelength_cat,3);
%% plot OD at all potentials

figure()
hold on
% for i = 1:size(ODvsWavelengthHJ,2)
% plot(WavelengthAbs,ODvsWavelengthHJ{i}(:,1))
% hold on
% end
scatter(WavelengthAbs_mono(1:5054),ODvsWavelengthHJ{1}(:,1))
% hold on
% plot(WavelengthAbs,ODvsWavelengthMoS2{5}(:,1),'bo-')
% plot(WavelengthAbs,ODvsWavelengthWSe2{5}(:,1),'ks-')
% legend('HJ','MoS2','WSe2')
xlabel('Wavelength (nm)')
ylabel('Optical Density')
% xlim([420 800])
% ylim([-0.01 .1])

%% Separate OD data intotpen the different otials

start_potential = 0.55;
end_potential = 0.0;
increment = -0.025;
potentials=[start_potential:increment:end_potential]'; % make a column of potentials

% 0.55 V
start_055 = find(ivium(2240:510459)>0.54 & ivium(2240:510459)<0.56,1)+ 2240; %
exclude the first 30 seconds of data before the ivium was turned on
end_055 = find(ivium(2240:510459)>0.525 & ivium(2240:510459)<0.54,1) + 2240;
mono_055 = find(Monoonpts>start_055 & Monoonpts<end_055);
ODvsWavelength_055 = ODvsWavelength_avg(mono_055(1):mono_055(size(mono_055)),1);
Wavelengthmono_055 = WavelengthAbs_mono(mono_055(1):mono_055(size(mono_055)));

%0.525 V
start_0525 = find(ivium(2233:510459)>0.515 & ivium(2233:510459)<0.535,1)+ 2233; %
exclude the first 30 seconds of data before the ivium was turned on
end_0525 = find(ivium(2233:510459)>0.50 & ivium(2233:510459)<0.515,1) + 2233;
mono_0525 = find(Monoonpts>start_0525 & Monoonpts<end_0525);
ODvsWavelength_0525 = ODvsWavelength_avg(mono_0525(1):mono_0525(size(mono_0525)),1);
Wavelengthmono_0525 = WavelengthAbs_mono(mono_0525(1):mono_0525(size(mono_0525)));
```

```
%0.50 V
start_050 = find(ivium(2233:510459)>0.49 & ivium(2233:510459)<0.51,1)+ 2233; %
exclude the first 30 seconds of data before the ivium was turned on
end_050 = find(ivium(2233:510459)>0.475 & ivium(2233:510459)<0.49,1) + 2233;
mono_050 = find(Monoonpts>start_050 & Monoonpts<end_050);
ODvsWavelength_050 = ODvsWavelength_avg(mono_050(1):mono_050(size(mono_050)),1);
Wavelengthmono_050 = WavelengthAbs_mono(mono_050(1):mono_050(size(mono_050)));

%0.475 V
start_0475 = find(ivium(2233:510459)>0.465 & ivium(2233:510459)<0.485,1)+ 2233; %
exclude the first 30 seconds of data before the ivium was turned on
end_0475 = find(ivium(2233:510459)>0.45 & ivium(2233:510459)<0.465,1) + 2233;
mono_0475 = find(Monoonpts>start_0475 & Monoonpts<end_0475);
ODvsWavelength_0475 = ODvsWavelength_avg(mono_0475(1):mono_0475(size(mono_0475)),1);
Wavelengthmono_0475 = WavelengthAbs_mono(mono_0475(1):mono_0475(size(mono_0475)));

% 0.45 V
start_045 = find(ivium(2233:510459)>0.44 & ivium(2233:510459)<0.46,1)+ 2233; %
exclude the first 30 seconds of data before the ivium was turned on
end_045 = find(ivium(2233:510459)>0.425 & ivium(2233:510459)<0.44,1) + 2233;
mono_045 = find(Monoonpts>start_045 & Monoonpts<end_045);
ODvsWavelength_045 = ODvsWavelength_avg(mono_045(1):mono_045(size(mono_045)),1);
Wavelengthmono_045 = WavelengthAbs_mono(mono_045(1):mono_045(size(mono_045)));

%0.425 V
start_0425 = find(ivium(2233:510459)>0.415 & ivium(2233:510459)<0.435,1)+ 2233; %
exclude the first 30 seconds of data before the ivium was turned on
end_0425 = find(ivium(2233:510459)>0.40 & ivium(2233:510459)<0.415,1) + 2233;
mono_0425 = find(Monoonpts>start_0425 & Monoonpts<end_0425);
ODvsWavelength_0425 = ODvsWavelength_avg(mono_0425(1):mono_0425(size(mono_0425)),1);
Wavelengthmono_0425 = WavelengthAbs_mono(mono_0425(1):mono_0425(size(mono_0425)));

%0.40 V
start_040 = find(ivium(2233:510459)>0.39 & ivium(2233:510459)<0.41,1)+ 2233; %
exclude the first 30 seconds of data before the ivium was turned on
end_040 = find(ivium(2233:510459)>0.375 & ivium(2233:510459)<0.39,1) + 2233;
mono_040 = find(Monoonpts>start_040 & Monoonpts<end_040);
ODvsWavelength_040 = ODvsWavelength_avg(mono_040(1):mono_040(size(mono_040)),1);
Wavelengthmono_040 = WavelengthAbs_mono(mono_040(1):mono_040(size(mono_040)));

%0.375 V
start_0375 = find(ivium(2233:510459)>0.365 & ivium(2233:510459)<0.385,1)+ 2233; %
exclude the first 30 seconds of data before the ivium was turned on
end_0375 = find(ivium(2233:510459)>0.35 & ivium(2233:510459)<0.365,1) + 2233;
mono_0375 = find(Monoonpts>start_0375 & Monoonpts<end_0375);
ODvsWavelength_0375 = ODvsWavelength_avg(mono_0375(1):mono_0375(size(mono_0375)),1);
Wavelengthmono_0375 = WavelengthAbs_mono(mono_0375(1):mono_0375(size(mono_0375)));

% 0.35 V
start_035 = find(ivium(2233:510459)>0.34 & ivium(2233:510459)<0.36,1)+ 2233; %
exclude the first 30 seconds of data before the ivium was turned on
end_035 = find(ivium(2233:510459)>0.325 & ivium(2233:510459)<0.34,1) + 2233;
mono_035 = find(Monoonpts>start_035 & Monoonpts<end_035);
ODvsWavelength_035 = ODvsWavelength_avg(mono_035(1):mono_035(size(mono_035)),1);
Wavelengthmono_035 = WavelengthAbs_mono(mono_035(1):mono_035(size(mono_035)));
```

```
%0.325 V
start_0325 = find(ivium(2233:510459)>0.315 & ivium(2233:510459)<0.335,1)+ 2233; %
exclude the first 30 seconds of data before the ivium was turned on
end_0325 = find(ivium(2233:510459)>0.30 & ivium(2233:510459)<0.315,1) + 2233;
mono_0325 = find(Monoonpts>start_0325 & Monoonpts<end_0325);
ODvsWavelength_0325 = ODvsWavelength_avg(mono_0325(1):mono_0325(size(mono_0325)),1);
Wavelengthmono_0325 = WavelengthAbs_mono(mono_0325(1):mono_0325(size(mono_0325)));

%0.30 V
start_030 = find(ivium(2233:510459)>0.29 & ivium(2233:510459)<0.31,1)+ 2233; %
exclude the first 30 seconds of data before the ivium was turned on
end_030 = find(ivium(2233:510459)>0.275 & ivium(2233:510459)<0.29,1) + 2233;
mono_030 = find(Monoonpts>start_030 & Monoonpts<end_030);
ODvsWavelength_030 = ODvsWavelength_avg(mono_030(1):mono_030(size(mono_030)),1);
Wavelengthmono_030 = WavelengthAbs_mono(mono_030(1):mono_030(size(mono_030)));

%0.275 V
start_0275 = find(ivium(2233:510459)>0.265 & ivium(2233:510459)<0.285,1)+ 2233; %
exclude the first 30 seconds of data before the ivium was turned on
end_0275 = find(ivium(2233:510459)>0.25 & ivium(2233:510459)<0.265,1) + 2233;
mono_0275 = find(Monoonpts>start_0275 & Monoonpts<end_0275);
ODvsWavelength_0275 = ODvsWavelength_avg(mono_0275(1):mono_0275(size(mono_0275)),1);
Wavelengthmono_0275 = WavelengthAbs_mono(mono_0275(1):mono_0275(size(mono_0275)));

% 0.25 V
start_025 = find(ivium(2233:510459)>0.24 & ivium(2233:510459)<0.26,1)+ 2233; %
exclude the first 30 seconds of data before the ivium was turned on
end_025 = find(ivium(2233:510459)>0.225 & ivium(2233:510459)<0.24,1) + 2233;
mono_025 = find(Monoonpts>start_025 & Monoonpts<end_025);
ODvsWavelength_025 = ODvsWavelength_avg(mono_025(1):mono_025(size(mono_025)),1);
Wavelengthmono_025 = WavelengthAbs_mono(mono_025(1):mono_025(size(mono_025)));

%0.225 V
% start_0225 = find(ivium(2240:510459)>0.210 & ivium(2240:510459)<0.235,1)+ 2240; %
exclude the first 30 seconds of data before the ivium was turned on
% end_0225 = find(ivium(2240:510459)>0.20 & ivium(2240:510459)<0.218,1) + 2240;
% mono_0225 = find(Monoonpts>start_0225 & Monoonpts<end_0225);
% ODvsWavelength_0225 =
ODvsWavelength_avg(mono_0225(1):mono_0225(size(mono_0225)),1);
% Wavelengthmono_0225 = WavelengthAbs_mono(mono_0225(1):mono_0225(size(mono_0225)));

%0.20 V
start_020 = find(ivium(2233:510459)>0.19 & ivium(2233:510459)<0.21,1)+ 2233; %
exclude the first 30 seconds of data before the ivium was turned on
end_020 = find(ivium(2233:510459)>0.175 & ivium(2233:510459)<0.19,1) + 2233;
mono_020 = find(Monoonpts>start_020 & Monoonpts<end_020);
ODvsWavelength_020 = ODvsWavelength_avg(mono_020(1):mono_020(size(mono_020)),1);
Wavelengthmono_020 = WavelengthAbs_mono(mono_020(1):mono_020(size(mono_020)));

%0.175 V
start_0175 = find(ivium(2233:510459)>0.165 & ivium(2233:510459)<0.185,1)+ 2233; %
exclude the first 30 seconds of data before the ivium was turned on
end_0175 = find(ivium(2233:510459)>0.15 & ivium(2233:510459)<0.165,1) + 2233;
mono_0175 = find(Monoonpts>start_0175 & Monoonpts<end_0175);
```

```
ODvsWavelength_0175 = ODvsWavelength_avg(mono_0175(1):mono_0175(size(mono_0175)),1);
Wavelengthmono_0175 = WavelengthAbs_mono(mono_0175(1):mono_0175(size(mono_0175)));

% 0.15 V
start_015 = find(ivium(2233:510459)>0.14 & ivium(2233:510459)<0.16,1)+ 2233; %
exclude the first 30 seconds of data before the ivium was turned on
end_015 = find(ivium(2233:510459)>0.125 & ivium(2233:510459)<0.14,1) + 2233;
mono_015 = find(Monoonpts>start_015 & Monoonpts<end_015);
ODvsWavelength_015 = ODvsWavelength_avg(mono_015(1):mono_015(size(mono_015)),1);
Wavelengthmono_015 = WavelengthAbs_mono(mono_015(1):mono_015(size(mono_015)));

%0.125 V
start_0125 = find(ivium(2233:510459)>0.115 & ivium(2233:510459)<0.135,1)+ 2233; %
exclude the first 30 seconds of data before the ivium was turned on
end_0125 = find(ivium(2233:510459)>0.10 & ivium(2233:510459)<0.115,1) + 2233;
mono_0125 = find(Monoonpts>start_0125 & Monoonpts<end_0125);
ODvsWavelength_0125 = ODvsWavelength_avg(mono_0125(1):mono_0125(size(mono_0125)),1);
Wavelengthmono_0125 = WavelengthAbs_mono(mono_0125(1):mono_0125(size(mono_0125)));

%0.10 V
start_010 = find(ivium(2233:510459)>0.09 & ivium(2233:510459)<0.11,1)+ 2233; %
exclude the first 30 seconds of data before the ivium was turned on
end_010 = find(ivium(2233:510459)>0.075 & ivium(2233:510459)<0.09,1) + 2233;
mono_010 = find(Monoonpts>start_010);
ODvsWavelength_010 = ODvsWavelength_avg(mono_010(1):mono_010(size(mono_010)),1);
Wavelengthmono_010 = WavelengthAbs_mono(mono_010(1):mono_010(size(mono_010)));

%0.075 V
start_0075 = find(ivium(2233:510459)>0.06 & ivium(2233:510459)<0.08,1)+ 2233; %
exclude the first 30 seconds of data before the ivium was turned on
end_0075 = find(ivium(2233:510459)>0.075 & ivium(2233:510459)<0.09,1) + 2233;
mono_0075 = find(Monoonpts>start_0075);
ODvsWavelength_0075 = ODvsWavelength_avg(mono_0075(1):mono_0075(size(mono_0075)),1);
Wavelengthmono_0075 = WavelengthAbs_mono(mono_0075(1):mono_0075(size(mono_0075)));

%0.05 V
start_005 = find(ivium(2233:510459)>0.04 & ivium(2233:510459)<0.06,1)+ 2233; %
exclude the first 30 seconds of data before the ivium was turned on
end_005 = find(ivium(2233:510459)>0.075 & ivium(2233:510459)<0.09,1) + 2233;
mono_005 = find(Monoonpts>start_005);
ODvsWavelength_005 = ODvsWavelength_avg(mono_005(1):mono_005(size(mono_005)),1);
Wavelengthmono_005 = WavelengthAbs_mono(mono_005(1):mono_005(size(mono_005)));

%0.025 V
start_0025 = find(ivium(2233:510459)>0.015 & ivium(2233:510459)<0.35,1)+ 2233; %
exclude the first 30 seconds of data before the ivium was turned on
end_0025 = find(ivium(2233:510459)>0.075 & ivium(2233:510459)<0.09,1) + 2233;
mono_0025 = find(Monoonpts>start_0025);
ODvsWavelength_0025 = ODvsWavelength_avg(mono_0025(1):mono_0025(size(mono_0025)),1);
Wavelengthmono_0025 = WavelengthAbs_mono(mono_0025(1):mono_0025(size(mono_0025)));

%0.00 V
start_00 = find(ivium(2233:510459)>-0.1 & ivium(2233:510459)<0.015,1)+ 2233; %
exclude the first 30 seconds of data before the ivium was turned on
end_00 = find(ivium(2233:510459)>0.075 & ivium(2233:510459)<0.09,1) + 2233;
```

```
mono_00 = find(Monoonpts>start_00);
ODvsWavelength_00 = ODvsWavelength_avg(mono_00(1):mono_00(size(mono_00)),1);
Wavelengthmono_00 = WavelengthAbs_mono(mono_00(1):mono_00(size(mono_00)));

%%

figure()
hold on
scatter(Wavelengthmono_055,ODvsWavelength_055)
%scatter(Wavelengthmono_0525,ODvsWavelength_0525)
scatter(Wavelengthmono_050,ODvsWavelength_050)
%scatter(Wavelengthmono_0475,ODvsWavelength_0475)
%scatter(Wavelengthmono_045,ODvsWavelength_045)
%scatter(Wavelengthmono_0425,ODvsWavelength_0425)
scatter(Wavelengthmono_040,ODvsWavelength_040)
%scatter(Wavelengthmono_0375,ODvsWavelength_0375)
%scatter(Wavelengthmono_035,ODvsWavelength_035)
%scatter(Wavelengthmono_0325,ODvsWavelength_0325)
scatter(Wavelengthmono_030,ODvsWavelength_030)
%scatter(Wavelengthmono_0275,ODvsWavelength_0275)
%scatter(Wavelengthmono_025,ODvsWavelength_025)
%scatter(Wavelengthmono_0225,ODvsWavelength_0225)
scatter(Wavelengthmono_020,ODvsWavelength_020)
%scatter(Wavelengthmono_0175,ODvsWavelength_0175)
scatter(Wavelengthmono_015,ODvsWavelength_015)
%scatter(Wavelengthmono_0125,ODvsWavelength_0125)
%scatter(Wavelengthmono_010,ODvsWavelength_010)

%legend('0.55V','0.525V','0.5V','0.475V','0.45V','0.425V','0.4V','0.375V','0.35V','0.
325V','0.3V','0.275V','0.25V','0.225V','0.2V','0.175V','0.15V', '0.125V','0.1V')
legend('0.55V','0.5V','0.4V','0.3V','0.2V','0.15V')
xlabel('Wavelength (nm)')
ylabel('Optical Density')
hold off

%% now average each potential and smooth a little

[wavelength_055,~,idx] = unique(Wavelengthmono_055); % Unique x's and their locations
(each wavelength)
ODmean_055 = smoothn(accumarray(idx,ODvsWavelength_055,[],@mean),1);

[wavelength_0525,~,idx] = unique(Wavelengthmono_0525); % Unique x's and their
locations (each wavelength)
ODmean_0525 = smoothn(accumarray(idx,ODvsWavelength_0525,[],@mean),1);

[wavelength_050,~,idx] = unique(Wavelengthmono_050); % Unique x's and their locations
(each wavelength)
ODmean_050 = smoothn(accumarray(idx,ODvsWavelength_050,[],@mean),1);

[wavelength_0475,~,idx] = unique(Wavelengthmono_0475); % Unique x's and their
locations (each wavelength)
ODmean_0475 = smoothn(accumarray(idx,ODvsWavelength_0475,[],@mean),1);

[wavelength_045,~,idx] = unique(Wavelengthmono_045); % Unique x's and their locations
(each wavelength)
```

```
ODmean_045 = smoothn(accumarray(idx,ODvsWavelength_045,[],@mean),1);

[wavelength_0425,~,idx] = unique(Wavelengthmono_0425); % Unique x's and their
locations (each wavelength)
ODmean_0425 = smoothn(accumarray(idx,ODvsWavelength_0425,[],@mean),1);

[wavelength_040,~,idx] = unique(Wavelengthmono_040); % Unique x's and their locations
(each wavelength)
ODmean_040 = smoothn(accumarray(idx,ODvsWavelength_040,[],@mean),1);

[wavelength_0375,~,idx] = unique(Wavelengthmono_0375); % Unique x's and their
locations (each wavelength)
ODmean_0375 = smoothn(accumarray(idx,ODvsWavelength_0375,[],@mean),1);

[wavelength_035,~,idx] = unique(Wavelengthmono_035); % Unique x's and their locations
(each wavelength)
ODmean_035 = smoothn(accumarray(idx,ODvsWavelength_035,[],@mean),1);

[wavelength_0325,~,idx] = unique(Wavelengthmono_0325); % Unique x's and their
locations (each wavelength)
ODmean_0325 = smoothn(accumarray(idx,ODvsWavelength_0325,[],@mean),1);

[wavelength_030,~,idx] = unique(Wavelengthmono_030); % Unique x's and their locations
(each wavelength)
ODmean_030 = smoothn(accumarray(idx,ODvsWavelength_030,[],@mean),1);

[wavelength_0275,~,idx] = unique(Wavelengthmono_0275); % Unique x's and their
locations (each wavelength)
ODmean_0275 = smoothn(accumarray(idx,ODvsWavelength_0275,[],@mean),1);

[wavelength_025,~,idx] = unique(Wavelengthmono_025); % Unique x's and their locations
(each wavelength)
ODmean_025 = smoothn(accumarray(idx,ODvsWavelength_025,[],@mean),1);

% [wavelength_0225,~,idx] = unique(Wavelengthmono_0225); % Unique x's and their
locations (each wavelength)
% ODmean_0225 = smoothn(accumarray(idx,ODvsWavelength_0225,[],@mean),1);

[wavelength_020,~,idx] = unique(Wavelengthmono_020); % Unique x's and their locations
(each wavelength)
ODmean_020 = smoothn(accumarray(idx,ODvsWavelength_020,[],@mean),1);

[wavelength_0175,~,idx] = unique(Wavelengthmono_0175); % Unique x's and their
locations (each wavelength)
ODmean_0175 = smoothn(accumarray(idx,ODvsWavelength_0175,[],@mean),1);

[wavelength_015,~,idx] = unique(Wavelengthmono_015); % Unique x's and their locations
(each wavelength)
ODmean_015 = smoothn(accumarray(idx,ODvsWavelength_015,[],@mean),1);

[wavelength_0125,~,idx] = unique(Wavelengthmono_0125); % Unique x's and their
locations (each wavelength)
ODmean_0125 = smoothn(accumarray(idx,ODvsWavelength_0125,[],@mean),1);
```

```
[wavelength_010,~,idx] = unique(Wavelengthmono_010); % Unique x's and their locations
(each wavelength)
ODmean_010 = smoothn(accumarray(idx,ODvsWavelength_010,[],@mean),1);

[wavelength_0075,~,idx] = unique(Wavelengthmono_0075); % Unique x's and their
locations (each wavelength)
ODmean_0075 = smoothn(accumarray(idx,ODvsWavelength_0075,[],@mean),1);

[wavelength_005,~,idx] = unique(Wavelengthmono_005); % Unique x's and their locations
(each wavelength)
ODmean_005 = smoothn(accumarray(idx,ODvsWavelength_005,[],@mean),1);

[wavelength_0025,~,idx] = unique(Wavelengthmono_0025); % Unique x's and their
locations (each wavelength)
ODmean_0025 = smoothn(accumarray(idx,ODvsWavelength_0025,[],@mean),1);

[wavelength_00,~,idx] = unique(Wavelengthmono_00); % Unique x's and their locations
(each wavelength)
ODmean_00 = smoothn(accumarray(idx,ODvsWavelength_00,[],@mean),1);
%%

ODmean_040_baselined = ODmean_040 - mean(ODmean_040(57:67))+0.001;
ODmean_045_baselined = ODmean_045 - mean(ODmean_045(57:67))+0.001;
ODmean_050_baselined = ODmean_050 - mean(ODmean_050(57:67))+0.001;
ODmean_0525_baselined = ODmean_0525 - mean(ODmean_0525(57:67))+0.001;
ODmean_055_baselined = ODmean_055 - mean(ODmean_055(57:67))+0.001;

map = brewermap(5,'RdYlBu')
f=figure;
ax = gca(f);ax.ColorOrder = map;
hold on;

plot(wavelength_040, ODmean_040_baselined, 'linewidth', 2)
plot(wavelength_040, ODmean_040_baselined, 'linewidth', 2)

legend('0.55V', '0.525V','0.5V','0.45V', '0.4V')
xlabel('Wavelength (nm)')
ylabel('Optical Density')
%%

%eV_axis = 1239.8 ./ wavelength_055;

map = brewermap(18,'RdYlBu');
f=figure;
ax = gca(f);ax.ColorOrder = map;
hold on;

plot(eV_axis, ODmean_055, 'linewidth', 4)
plot(eV_axis, ODmean_0525, 'linewidth', 4)
plot(eV_axis, ODmean_050, 'linewidth', 4)
plot(eV_axis, ODmean_0475, 'linewidth', 4)
plot(eV_axis, ODmean_045, 'linewidth', 4)
plot(eV_axis, ODmean_0425, 'linewidth', 4)
plot(eV_axis, ODmean_040, 'linewidth', 4)
plot(eV_axis, ODmean_0375, 'linewidth', 4)
```

```
plot(eV_axis, ODmean_035, 'linewidth', 4)
plot(eV_axis, ODmean_0325, 'linewidth', 4)
plot(eV_axis, ODmean_030, 'linewidth', 4)
plot(eV_axis, ODmean_0275, 'linewidth', 4)
plot(eV_axis, ODmean_025, 'linewidth', 4)
plot(eV_axis, ODmean_0225, 'linewidth', 4)
plot(eV_axis, ODmean_020, 'linewidth', 4)
plot(eV_axis, ODmean_0175, 'linewidth', 4)
plot(eV_axis, ODmean_015, 'linewidth', 4)
plot(eV_axis, ODmean_0125, 'linewidth', 4)
% plot(eV_axis, ODmean_010, 'linewidth', 4)
% plot(eV_axis, ODmean_0075, 'linewidth', 4)
% plot(eV_axis, ODmean_005, 'linewidth', 4)
% plot(eV_axis, ODmean_0025, 'linewidth', 4)
% plot(eV_axis, ODmean_00, 'linewidth', 4)
%legend('0.55V','0.5V','0.4V','0.3V','0.2V','0.15V')
xlabel('Wavelength (nm)')
ylabel('Optical Density')
hold off
%% plot difference spectra

% use 0.25V as VOC
% calcuate as Av - Avoc

A_voc = ODmean_035;

diff_ODmean_0125 = ODmean_0125 - A_voc;
diff_ODmean_015 = ODmean_015 - A_voc;
diff_ODmean_0175 = ODmean_0175 - A_voc;
diff_ODmean_020 = ODmean_020 - A_voc;
diff_ODmean_0225 = ODmean_0225 - A_voc;
diff_ODmean_025 = ODmean_025 - A_voc;
diff_ODmean_0275 = ODmean_0275 - A_voc;
diff_ODmean_030 = ODmean_030 - A_voc;
diff_ODmean_0325 = ODmean_0325 - A_voc;
diff_ODmean_035 = ODmean_035 - A_voc;
diff_ODmean_0375 = ODmean_0375 - A_voc;
diff_ODmean_040 = ODmean_040 - A_voc;
diff_ODmean_0425 = ODmean_0425 - A_voc;
diff_ODmean_045 = ODmean_045 - A_voc;
diff_ODmean_0475 = ODmean_0475 - A_voc;
diff_ODmean_050 = ODmean_050 - A_voc;
diff_ODmean_0525 = ODmean_0525 - A_voc;
diff_ODmean_055 = ODmean_055 - A_voc;

%% plot diff OD
map = brewermap(17,'RdYlBu')
f=figure;
ax = gca(f);ax.ColorOrder = map;
hold on;

plot(wavelength_055, diff_ODmean_055, 'linewidth', 2)
plot(wavelength_0525, diff_ODmean_0525, 'linewidth', 2)
plot(wavelength_050, diff_ODmean_050, 'linewidth', 2)
plot(wavelength_0475, diff_ODmean_0475, 'linewidth', 2)
```

```
plot(wavelength_045, diff_ODmean_045, 'linewidth', 2)
plot(wavelength_0425, diff_ODmean_0425, 'linewidth', 2)
plot(wavelength_040, diff_ODmean_040, 'linewidth', 2)
plot(wavelength_0375, diff_ODmean_0375, 'linewidth', 2)
plot(wavelength_035, diff_ODmean_035, 'linewidth', 2)
plot(wavelength_0325, diff_ODmean_0325, 'linewidth', 2)
plot(wavelength_030, diff_ODmean_030, 'linewidth', 2)
plot(wavelength_0275, diff_ODmean_0275, 'linewidth', 2)
plot(wavelength_025, diff_ODmean_025, 'linewidth', 2)
plot(wavelength_0225, diff_ODmean_0225, 'linewidth', 2)
plot(wavelength_020, diff_ODmean_020, 'linewidth', 2)
plot(wavelength_0175, diff_ODmean_0175, 'linewidth', 2)
plot(wavelength_015, diff_ODmean_015, 'linewidth', 2)
%legend('0.55V','0.5V','0.4V','0.3V','0.2V','0.15V')
xlabel('Wavelength (nm)')
ylabel('\DeltaA')
xlim([415 695])
hold off

%% fit A exciton with gaussian to find amplitude
%function func_plotgaussAex(data, nm)
%check that fit is good with plotgaussAex then actually fit with fitAex

%func_plotgaussAex(ODmean_0125, wavelength_0125)
func_plotgaussAex(ODmean_015, wavelength_015)
func_plotgaussAex(ODmean_0175, wavelength_0175)
func_plotgaussAex(ODmean_020, wavelength_020)
func_plotgaussAex(ODmean_0225, wavelength_0225)
func_plotgaussAex(ODmean_025, wavelength_025)
func_plotgaussAex(ODmean_0275, wavelength_0275)
func_plotgaussAex(ODmean_030, wavelength_030)
func_plotgaussAex(ODmean_0325, wavelength_0325)
func_plotgaussAex(ODmean_035, wavelength_035)
func_plotgaussAex(ODmean_0375, wavelength_0375)
func_plotgaussAex(ODmean_040, wavelength_040)
func_plotgaussAex(ODmean_0425, wavelength_0425)
func_plotgaussAex(ODmean_045, wavelength_045)
func_plotgaussAex(ODmean_0475, wavelength_0475)
func_plotgaussAex(ODmean_050, wavelength_050)
func_plotgaussAex(ODmean_0525, wavelength_0525)
func_plotgaussAex(ODmean_055, wavelength_055)
%% actually fit and save amplitudes

%[Az_area, Az_gauss_amp, A_center_freq, A_fwhm] = func_fitAex(data, nm)

%[~, A_amp_0125, ~, ~] = func_fitAex(ODmean_0125, wavelength_0125);
[~, A_amp_015, A_centwl_015, ~] = func_fitAex(ODmean_015, wavelength_015);
[~, A_amp_0175, A_centwl_0175, ~] = func_fitAex(ODmean_0175, wavelength_0175);
[~, A_amp_020, A_centwl_020, ~] = func_fitAex(ODmean_020, wavelength_020);
[~, A_amp_0225, A_centwl_0225, ~] = func_fitAex(ODmean_0225, wavelength_0225);
[~, A_amp_025, A_centwl_025, ~] = func_fitAex(ODmean_025, wavelength_025);
[~, A_amp_0275, A_centwl_0275, ~] = func_fitAex(ODmean_0275, wavelength_0275);
[~, A_amp_030, A_centwl_030, ~] = func_fitAex(ODmean_030, wavelength_030);
[~, A_amp_0325, A_centwl_0325, ~] = func_fitAex(ODmean_0325, wavelength_0325);
[~, A_amp_035, A_centwl_035, ~] = func_fitAex(ODmean_035, wavelength_035);
```

```
[~, A_amp_0375, A_centwl_0375, ~] = func_fitAex(ODmean_0375, wavelength_0375);
[~, A_amp_040, A_centwl_040, ~] = func_fitAex(ODmean_040, wavelength_040);
[~, A_amp_0425, A_centwl_0425, ~] = func_fitAex(ODmean_0425, wavelength_0425);
[~, A_amp_045, A_centwl_045, ~] = func_fitAex(ODmean_045, wavelength_045);
[~, A_amp_0475, A_centwl_0475, ~] = func_fitAex(ODmean_0475, wavelength_0475);
[~, A_amp_050, A_centwl_050, ~] = func_fitAex(ODmean_050, wavelength_050);
[~, A_amp_0525, A_centwl_0525, ~] = func_fitAex(ODmean_0525, wavelength_0525);
[~, A_amp_055, A_centwl_055, ~] = func_fitAex(ODmean_055, wavelength_055);

A_amp_OCP = A_amp_025;

%% calculate carrier density at each potential
% equation is (Aocp/Av - 1)Dc = Dn
A_amp_0 = A_amp_0475;
D_c = 7.36e13;

D_n_015 = abs((A_amp_0/A_amp_015)-1)*D_c;
D_n_0175 = abs((A_amp_0/A_amp_0175)-1)*D_c;
D_n_020 = abs((A_amp_0/A_amp_020)-1)*D_c;
D_n_0225 = abs((A_amp_0/A_amp_0225)-1)*D_c;
D_n_025 = abs((A_amp_0/A_amp_025)-1)*D_c;
D_n_0275 = abs((A_amp_0/A_amp_0275)-1)*D_c;
D_n_030 = abs((A_amp_0/A_amp_030)-1)*D_c;
D_n_0325 = abs((A_amp_0/A_amp_0325)-1)*D_c;
D_n_035 = abs((A_amp_0/A_amp_035)-1)*D_c;
D_n_0375 = abs((A_amp_0/A_amp_0375)-1)*D_c;
D_n_040 = abs((A_amp_0/A_amp_040)-1)*D_c;
D_n_0425 = abs((A_amp_0/A_amp_0425)-1)*D_c;
D_n_045 = abs((A_amp_0/A_amp_045)-1)*D_c;
D_n_0475 = abs((A_amp_0/A_amp_0475)-1)*D_c;
D_n_050 = abs((A_amp_0/A_amp_050)-1)*D_c;
D_n_0525 = abs((A_amp_0/A_amp_0525)-1)*D_c;
D_n_055 = abs((A_amp_0/A_amp_055)-1)*D_c;

%% calculate delta E exciton A

% calculated as E0 - EappliedV and E0 is the energy at the maximum
% absorption
% convert table of delta E values to meV
% eV = 1239.8/nm

A_centwl_max = 1239800 / A_centwl_0475;

DEexciton_015 = A_centwl_max - 1239800 / A_centwl_015;
DEexciton_0175 = A_centwl_max - 1239800 / A_centwl_0175;
DEexciton_020 = A_centwl_max - 1239800 / A_centwl_020;
DEexciton_0225 = A_centwl_max - 1239800 / A_centwl_0225;
DEexciton_025 = A_centwl_max - 1239800 / A_centwl_025;
DEexciton_0275 = A_centwl_max - 1239800 / A_centwl_0275;
DEexciton_030 = A_centwl_max - 1239800 / A_centwl_030;
DEexciton_0325 = A_centwl_max - 1239800 / A_centwl_0325;
DEexciton_035 = A_centwl_max - 1239800 / A_centwl_035;
DEexciton_0375 = A_centwl_max - 1239800 / A_centwl_0375;
DEexciton_040 = A_centwl_max - 1239800 / A_centwl_040;
DEexciton_0425 = A_centwl_max - 1239800 / A_centwl_0425;
```

```
DEexciton_045 = A_centwl_max - 1239800 / A_centwl_045;
DEexciton_0475 = A_centwl_max - 1239800 / A_centwl_0475;
DEexciton_050 = A_centwl_max - 1239800 / A_centwl_050;
DEexciton_0525 = A_centwl_max - 1239800 / A_centwl_0525;
DEexciton_055 = A_centwl_max - 1239800 / A_centwl_055;


%% plot Dn vs potential

figure()
hold on
scatter(0.15, D_n_015, 'blue', 'filled');
scatter(0.175, D_n_0175, 'blue', 'filled');
scatter(0.20, D_n_020, 'blue', 'filled');
scatter(0.225, D_n_0225, 'blue', 'filled');
scatter(0.25, D_n_025, 'blue', 'filled');
scatter(0.275, D_n_0275, 'blue', 'filled');
scatter(0.30, D_n_030, 'blue', 'filled');
scatter(0.325, D_n_0325, 'blue', 'filled');
scatter(0.35, D_n_035, 'blue', 'filled');
scatter(0.375, D_n_0375, 'blue', 'filled');
scatter(0.40, D_n_040, 'blue', 'filled');
scatter(0.425, D_n_0425, 'blue', 'filled');
scatter(0.45, D_n_045, 'blue', 'filled');
scatter(0.475, D_n_0475, 'blue', 'filled');
scatter(0.50, D_n_050, 'blue', 'filled');
scatter(0.525, D_n_0525, 'blue', 'filled');
scatter(0.55, D_n_055, 'blue', 'filled');
set(gca,'yscale','log')
hold off

%% plot Dn vs deltaE


figure()
hold on
scatter(DEexciton_015, D_n_015, 'blue', 'filled');
scatter(DEexciton_0175, D_n_0175, 'blue', 'filled');
scatter(DEexciton_020, D_n_020, 'blue', 'filled');
scatter(DEexciton_0225, D_n_0225, 'blue', 'filled');
scatter(DEexciton_025, D_n_025, 'blue', 'filled');
scatter(DEexciton_0275, D_n_0275, 'blue', 'filled');
scatter(DEexciton_030, D_n_030, 'blue', 'filled');
scatter(DEexciton_0325, D_n_0325, 'blue', 'filled');
scatter(DEexciton_035, D_n_035, 'blue', 'filled');
scatter(DEexciton_0375, D_n_0375, 'blue', 'filled');
scatter(DEexciton_040, D_n_040, 'blue', 'filled');
scatter(DEexciton_0425, D_n_0425, 'blue', 'filled');
scatter(DEexciton_045, D_n_045, 'blue', 'filled');
scatter(DEexciton_0475, D_n_0475, 'blue', 'filled');
scatter(DEexciton_050, D_n_050, 'blue', 'filled');
scatter(DEexciton_0525, D_n_0525, 'blue', 'filled');
scatter(DEexciton_055, D_n_055, 'blue', 'filled');
set(gca,'yscale','log')
hold off
```

```
%%
Potential_dependent_table(1,3) = DEexciton_015;
Potential_dependent_table(2,3) = DEexciton_0175;
Potential_dependent_table(3,3) = DEexciton_020;
Potential_dependent_table(4,3) = DEexciton_0225;
Potential_dependent_table(5,3) = DEexciton_025;
Potential_dependent_table(6,3) = DEexciton_0275;
Potential_dependent_table(7,3) = DEexciton_030;
Potential_dependent_table(8,3) = DEexciton_0325;
Potential_dependent_table(9,3) = DEexciton_035;
Potential_dependent_table(10,3) = DEexciton_0375;
Potential_dependent_table(11,3) = DEexciton_040;
Potential_dependent_table(12,3) = DEexciton_0425;
Potential_dependent_table(13,3) = DEexciton_045;
Potential_dependent_table(14,3) = DEexciton_0475;
Potential_dependent_table(15,3) = DEexciton_050;
Potential_dependent_table(16,3) = DEexciton_0525;
Potential_dependent_table(17,3) = DEexciton_055;

Potential_dependent_table(1,2) = D_n_015;
Potential_dependent_table(2,2) = D_n_0175;
Potential_dependent_table(3,2) = D_n_020;
Potential_dependent_table(4,2) = D_n_0225;
Potential_dependent_table(5,2) = D_n_025;
Potential_dependent_table(6,2) = D_n_0275;
Potential_dependent_table(7,2) = D_n_030;
Potential_dependent_table(8,2) = D_n_0325;
Potential_dependent_table(9,2) = D_n_035;
Potential_dependent_table(10,2) = D_n_0375;
Potential_dependent_table(11,2) = D_n_040;
Potential_dependent_table(12,2) = D_n_0425;
Potential_dependent_table(13,2) = D_n_045;
Potential_dependent_table(14,2) = D_n_0475;
Potential_dependent_table(15,2) = D_n_050;
Potential_dependent_table(16,2) = D_n_0525;
Potential_dependent_table(17,2) = D_n_055;
%% plot of wavelength max versus applied potential
figure()
hold on
scatter(0.15, A_centwl_015, 'blue', 'filled');
scatter(0.175, A_centwl_0175, 'blue', 'filled');
scatter(0.20, A_centwl_020, 'blue', 'filled');
scatter(0.225, A_centwl_0225, 'blue', 'filled');
scatter(0.25, A_centwl_025, 'blue', 'filled');
scatter(0.275, A_centwl_0275, 'blue', 'filled');
scatter(0.30, A_centwl_030, 'blue', 'filled');
scatter(0.325, A_centwl_0325, 'blue', 'filled');
scatter(0.35, A_centwl_035, 'blue', 'filled');
scatter(0.375, A_centwl_0375, 'blue', 'filled');
scatter(0.40, A_centwl_040, 'blue', 'filled');
scatter(0.425, A_centwl_0425, 'blue', 'filled');
scatter(0.45, A_centwl_045, 'blue', 'filled');
scatter(0.475, A_centwl_0475, 'blue', 'filled');
scatter(0.50, A_centwl_050, 'blue', 'filled');
```

```
scatter(0.525, A_centwl_0525, 'blue', 'filled');
scatter(0.55, A_centwl_055, 'blue', 'filled');
hold off

%% make variables for fitting

D_n = Potential_dependent_table(:,2);
D_exciton = Potential_dependent_table(:,3);

cftool
%% fitting the XYZ data

XYZ_bandgap = XYZdataset(:,2);
XYZ_carrierden = XYZdataset(:,1);
% generate fitted curve
xfit = 0:0.1:70;
yfit = 2.183*exp(-0.003534.*xfit);
figure()
hold on
scatter(XYZ_carrierden, XYZ_bandgap)
plot(xfit,yfit)

%%
xfit_2 = 0:0.1:70;
yfit_2 = 0.467*exp(-0.04266.*xfit_2)+1.81;
figure()
hold on
scatter(XYZ_carrierden, XYZ_bandgap)
plot(xfit_2,yfit_2)
ylim([1.6 2.6])

%%
D_n_adj = Potential_dependent_table(:,2)/10^12;
yfit_Dn = 0.467*exp(-0.04266.*D_n_adj)+1.81;
xfit_2 = 0:0.1:145;
yfit_2 = 0.467*exp(-0.04266.*xfit_2)+1.81;
figure()
hold on
scatter(D_n_adj, yfit_Dn)
plot(xfit_2,yfit_2)
ylim([1.6 2.6])
%% plot of wavelength max versus applied potential with bandgap energy
figure()
hold on
scatter(0.15, 1239.8/A_centwl_015, 'blue', 'filled');
scatter(0.175, 1239.8/A_centwl_0175, 'blue', 'filled');
scatter(0.20, 1239.8/A_centwl_020, 'blue', 'filled');
scatter(0.225, 1239.8/A_centwl_0225, 'blue', 'filled');
scatter(0.25, 1239.8/A_centwl_025, 'blue', 'filled');
scatter(0.275, 1239.8/A_centwl_0275, 'blue', 'filled');
scatter(0.30, 1239.8/A_centwl_030, 'blue', 'filled');
scatter(0.325, 1239.8/A_centwl_0325, 'blue', 'filled');
scatter(0.35, 1239.8/A_centwl_035, 'blue', 'filled');
scatter(0.375, 1239.8/A_centwl_0375, 'blue', 'filled');
scatter(0.40, 1239.8/A_centwl_040, 'blue', 'filled');
```

```
scatter(0.425, 1239.8/A_centwl_0425, 'blue', 'filled');
scatter(0.45, 1239.8/A_centwl_045, 'blue', 'filled');
scatter(0.475, 1239.8/A_centwl_0475, 'blue', 'filled');
scatter(0.50, 1239.8/A_centwl_050, 'blue', 'filled');
scatter(0.525, 1239.8/A_centwl_0525, 'blue', 'filled');
scatter(0.55, 1239.8/A_centwl_055, 'blue', 'filled');
scatter(Potential_dependent_table(:,1),yfit_Dn, 'black', 'filled');
hold off

%% fit C exciton

[~, C_amp_015, C_centwl_015, ~] = func_fitCex(ODmean_015, wavelength_015);
[~, C_amp_0175, C_centwl_0175, ~] = func_fitCex(ODmean_0175, wavelength_0175);
[~, C_amp_020, C_centwl_020, ~] = func_fitCex(ODmean_020, wavelength_020);
[~, C_amp_0225, C_centwl_0225, ~] = func_fitCex(ODmean_0225, wavelength_0225);
[~, C_amp_025, C_centwl_025, ~] = func_fitCex(ODmean_025, wavelength_025);
[~, C_amp_0275, C_centwl_0275, ~] = func_fitCex(ODmean_0275, wavelength_0275);
[~, C_amp_030, C_centwl_030, ~] = func_fitCex(ODmean_030, wavelength_030);
[~, C_amp_0325, C_centwl_0325, ~] = func_fitCex(ODmean_0325, wavelength_0325);
[~, C_amp_035, C_centwl_035, ~] = func_fitCex(ODmean_035, wavelength_035);
[~, C_amp_0375, C_centwl_0375, ~] = func_fitCex(ODmean_0375, wavelength_0375);
[~, C_amp_040, C_centwl_040, ~] = func_fitCex(ODmean_040, wavelength_040);
[~, C_amp_0425, C_centwl_0425, ~] = func_fitCex(ODmean_0425, wavelength_0425);
[~, C_amp_045, C_centwl_045, ~] = func_fitCex(ODmean_045, wavelength_045);
[~, C_amp_0475, C_centwl_0475, ~] = func_fitCex(ODmean_0475, wavelength_0475);
[~, C_amp_050, C_centwl_050, ~] = func_fitCex(ODmean_050, wavelength_050);
[~, C_amp_0525, C_centwl_0525, ~] = func_fitCex(ODmean_0525, wavelength_0525);
[~, C_amp_055, C_centwl_055, ~] = func_fitCex(ODmean_055, wavelength_055);


%% plot of wavelength max versus applied potential with bandgap energy
figure()
hold on
scatter(0.15, C_amp_015, 'blue', 'filled');
scatter(0.175, C_amp_0175, 'blue', 'filled');
scatter(0.20, C_amp_020, 'blue', 'filled');
scatter(0.225, C_amp_0225, 'blue', 'filled');
scatter(0.25, C_amp_025, 'blue', 'filled');
scatter(0.275, C_amp_0275, 'blue', 'filled');
scatter(0.30, C_amp_030, 'blue', 'filled');
scatter(0.325, C_amp_0325, 'blue', 'filled');
scatter(0.35, C_amp_035, 'blue', 'filled');
scatter(0.375, C_amp_0375, 'blue', 'filled');
scatter(0.40, C_amp_040, 'blue', 'filled');
scatter(0.425, C_amp_0425, 'blue', 'filled');
scatter(0.45, C_amp_045, 'blue', 'filled');
scatter(0.475, C_amp_0475, 'blue', 'filled');
scatter(0.50, C_amp_050, 'blue', 'filled');
scatter(0.525, C_amp_0525, 'blue', 'filled');
scatter(0.55, C_amp_055, 'blue', 'filled');
hold off
```